DEVELOPING GRAPHENE-ORGANIC HYBRID ELECTRODES FOR SILICON BASED SCHOTTKY DEVICES

A Thesis Submitted to
the Graduate School of Engineering and Sciences of
İzmir Institute of Technology
in Partial Fulfillment of the Requirements for the Degree of

DOCTOR OF PHILOSOPHY

in Materials Science and Engineering

by
Hasan AYDIN

July 2018
İZMİR

We approve the thesis of **Hasan AYDIN**

Examining committee members:

Assoc. Prof. Dr. Cem ÇELEBİ
Department of Physics, İzmir Institute of Technology

Prof. Dr. Serdar ÖZÇELİK
Deparment of Photonics, İzmir Institute of Technology

Assoc. Prof. Dr. İlbeyi AVCI
Department of Physics, Ege University

Assoc. Prof. Dr. Hasan ŞAHİN
Department of Photonics, İzmir Institute of Technology

Assist. Prof. Dr. Gökhan UTLU
Department of Physics, Ege University

04 July 2018

Assoc. Prof. Dr. Cem ÇELEBİ
Supervisor, Department of Physics,
İzmir Institute of Technology

Prof. Dr. Canan VARLIKLI
Co-Supervisor, Department of
Photonics,
İzmir Institute of Technology

Prof. Dr. Mustafa Muammer DEMİR
Head of the Department of Materials
Science and Engineering

Prof. Dr. Aysun SOFUOĞLU
Dean of the Graduate School of
Engineering and Sciences

ACKNOWLEDGEMENTS

Firstly, I would like to my deeply thanks to my advisor Assoc. Prof. Dr. Cem Çelebi for his invaluable help, guidance, encouragement and support throughout this thesis.

I thankfully commemorate my former advisor Assoc. Prof. Dr. Yusuf Selamet for his great contributions and unique assistance. Without his support and guidance, I would never have been able to complete this thesis.

I am thankful for my co-advisor Prof. Dr. Canan Varlıklı for her help, guidance, encouragement and detailed reviewing of my thesis.

I also would like to thank my committee members of my thesis Prof. Dr. Serdar Özçelik, Assoc. Prof. Dr. İlbeyi Avcı and Assist. Prof. Dr. Gökhan Utlu for their participations and contributions to this thesis.

In addition, I would like to thank Assoc. Prof. Dr. Mustafa Can for providing SAMs and Dr. Cihan Bacaksız for theoretical calculations. I am also thankful to Assoc. Prof. Dr. Hasan Şahin for his encouragement, motivation and great contributions to this thesis.

I would also like to thank my lab mates Nesli Yağmurcukardeş who stood me almost 10 years, Atike İnce Yardımcı, Alper Yanılmaz, Elif Bilgilisoy Alperen, Begüm Yavaş, Barış Akbalı and all the members of IRMAM for their friendship and support.

I am also grateful to my lab mates Batuhan Kalkan for all brainstorming and help, Dilce Özkendir, Mehmet Fidan and all the members of Quantum Device Lab for their support and friendly work environment. I am also thankful to Dr. Mehmet Yağmurcukardeş for his friendship, plenty of laughter and entertaining moments. Furthermore, I would like to thank Zebih Çetin and Ece Meriç for their friendship. Osman Gümüş and Mustafa Kıran are another people I would like to thanks. They are my best friends that we have shared bitter sweet days together since our childhood, and life is beautiful and more enjoyable with them.

Last but not least, I want to deeply thanks to my family for leading me to this stage, unconditional love and their endless support during all of my life. I can’t think of a life without them.

This research was supported by TUBITAK with 112T946 project number.

ABSTRACT

DEVELOPING GRAPHENE-ORGANIC HYBRID ELECTRODES FOR SILICON BASED SCHOTTKY DEVICES

This thesis focused on developing graphene-organic hybrid electrodes for silicon based Schottky devices. Two different sets of carboxylic acid based SAMs were used to improve the rectification character of the Schottky junction formed at graphene/Si interface. While the first set of SAMs consists of MePIFA and DPIFA, the second set of SAMs contains TPA and CAR. In addition to this, P3HT, which is known to be an electron donor and absorb light in the visible spectrum, was utilized to form P3HT-graphene bilayer electrode. Current-voltage characteristics of bare and SAMs modified devices showed rectification behavior confirming a Schottky junction formation at the graphene/Si interface. The DPIFA SAMs device exhibited better diode performance compare to MePIFA SAMs due to the absence of methyl group which hinders π-π interaction between SAMs molecule and graphene. Furthermore, the CAR-based device indicates better diode characteristic with respect to the TPA-based device due to smaller energy differences between graphene and CAR.

The effect of P3HT-graphene bilayer electrode on the photoresponsivity characteristics of Silicon based Schottky photodetectors have been also investigated. Current-voltage measurements of graphene/Si and P3HT-graphene/Si revealed rectification behavior confirming Schottky junction formation at the graphene/Si interface. Time-resolved photocurrent measurements exhibited excellent durability and fast response speed. Moreover, the maximum photoresponsivity of P3HT-graphene/Si photodetector increased compared to that of bare graphene/Si photodetector. The observed increment in the photoresponsivity of P3HT-graphene/Si devices was attributed to the charge transfer doping from P3HT to graphene within the spectral range between near-ultraviolet and near-infrared. Finally, P3HT-graphene electrode was found to improve the specific detectivity and noise equivalent power of graphene/Si photodetectors.

ÖZET

SİLİKON TABANLI SCHOTTKY AYGITLAR İÇİN GRAFEN-ORGANİK HİBRİT ELEKTROTLAR GELİŞTİRİLMESİ

Bu tez silikon tabanlı Schottky aygıtlar için grafen-organik hibrit elektrotlar geliştirilmesine odaklanmıştır. Grafen/Si arayüzünü geliştirmek için iki farklı set karboksilik asit bazlı kendiliğinden organize tek katman molekülleri kullanılmıştır. İlk kendiliğinden organize tek katman seti MePIFA ve DPIFA'dan oluşurken, ikinci kendiliğinden organize tek katman seti TPA ve CAR içerir. Buna ek olarak, P3HT-grafen iki katmanlı elektrot oluşturmak için bir elektron verici olduğu bilinen ve görünür spektrumda ışığa absorbe eden P3HT kullanılmıştır. Yalın ve kendiliğinden organize tek katman molekülleriyle modifiye edilmiş aygıtların akım-gerilim karakteristikleri grafen/Si arayüzeyinde bir Schottky birleşimi oluşumunu doğrulayan düzeltme davranışını gösterir. DPIFA aygıtı, MePIFA aygıtı ile karşılaştırıldığında kendiliğinden organize tek katman molekülü ve grafen arasında π-π etkileşimini engelleyen metil grubunun olmaması nedeniyle daha iyi diyot performansı sergilemiştir. Ayrıca, CAR tabanlı aygıt, grafen ve CAR arasındaki daha küçük enerji farklılıklarından dolayı TPA tabanlı aygıta göre daha iyi diyot karakteristiğini göstermiştir.

P3HT-grafen iki katmanlı elektrodun Silikon bazlı Schottky fotodetektörlerin fotoduyarlılık karakteristiği üzerine etkisi ayrıca araştırılmıştır. Grafen/Si ve P3HT-grafen/Si akım-gerilim ölçüm sonuçları grafen/Si arayüzünde Schottky bağlantı oluşumunu doğrulayan düzeltme davranışını ortaya çıkarmıştır. Zamana bağlı fotoakım spektroskopisi ölçümleri mükemmel dayanıklılık ve hızlı tepki sergilemiştir. Ayrıca, P3HT-grafen fotodetektörün maksimum spektral fotoduyarlılığı grafen/Si fotodetektöre göre karşılaştırıldığında üç kat daha fazla artmıştır. P3HT-grafen aygıtlarının fotoduyarlılığında gözlenen artış yakın ultraviyole ve yakın kızılötesi arasındaki spektral aralık içinde P3HT den grafene yük transfer katkılanmasından kaynaklanmıştır. Son olarak, P3HT-grafen elektrodu grafen/Si fotodetektörün algılama hassasiyeti ve gürültü eşdeğer gücü geliştirdiği bulunmuştur.

TABLE OF CONTENTS

LIST OF FIGURES

LIST OF TABLES

LIST OF ABBREVIATIONS

SPD	Surface Potential Difference
CVD	Chemical Vapor Deposition
APCVD	Atmospheric Pressure Chemical Vapor Deposition
SAMs	Self-Assembled Monolayers
P3HT	Poly (3-hexylthiophene-2.5-diyl)
MePIFA	5-[(3-methylphenyl) (phenyl) amino] izoftalic acid
DPIFA	5-(diphenyl) amino] izoftalic acid
TPA	4″bis(diphenylamino)-1,1′:3″,-terphenyl-5′carboxylic acids
CAR	4,4-di-9H-carbazol-9-yl-1,1′:3′1′-terphenyl-5′carboxylic acid
Cu	Copper
Ni	Nickel
PR	Photoresist
TE	Thermionic Emission
TFE	Thermionic Field Emission
SiC	Silicon Carbide
SLG	Single Layer Graphene
BLG	Bilayer Graphene
HOPG	Highly-Oriented Pyrolytic Graphite
SEM	Scanning Electron Microscopy
KPFM	Kelvin Probe Force Microscopy
AFM	Atomic Force Microscopy
CV	Cyclic Voltammetry

CHAPTER 1

INTRODUCTION

Graphene, as one atom thick sheet of sp^2 bonded carbon atoms arranged in a honeycomb lattice [1], forms a Schottky junction with rectification character when it is transferred onto most of the conventional semiconducting materials like Si [2], GaN [3], GaAs [4] and SiC [5]. In addition, owing to its high charge carrier mobility [6], superior optical transparency [7] and modulation of Fermi level [8], graphene is considered to be used as transparent conductive electrode alternative to Indium-Thin-Oxide (ITO) in microelectronic and optoelectronic devices operating with low leakage currents. Among these materials, Si is more convenient material as it is the non-toxic, rich in the nature, mostly preferred material in integrated electronics and has large built-in field with graphene (V_{bi} = 0.55 - 0.75 V) [2].

Understanding of metal/semiconductor Schottky junction is essential for the improvement of technological device applications. Contrary to conventional metal/semiconductor Schottky devices, where the Fermi level of the metal remains constant due to a high density of states, even small variations in charge carrier density can significantly change the Fermi level of graphene, resulting in modification of Schottky barrier height and rectification behavior of the junction. Graphene/Si Schottky junction photodetectors have gained an increasing amount of attention over the past few years due to their photodetection capability for a broad wavelength range between 400 and 1100 nm [9-15]. However, the maximum value for the photoresponsivity of these devices is restricted to only about 0.3 mAW^{-1} as a consequence of their substantially low light absorption/gain ratio [9, 16]. For improving device photoresponsivity, the Fermi level of graphene should be lowered to increase both the magnitude of the built-in potential and junction electric field that promote effective charge separation at the depletion region of the semiconducting material underneath [9, 17]. Recently, a hybrid structure that combines graphene-Si quantum dots (Si-QDs) has been reported to enhance the device photoresponsivity [17]. However, the photoresponsivity of this device is still limited to only about 0.5 AW^{-1} and besides it exhibits narrow band optical photodetection greatly hindering the photodetector's wavelength detection capability especially between near-ultraviolet and near-infrared spectral range. Recently, graphene-conductive polymer bilayer structures have attracted a great attention since the conductive polymers provide a broad range of flexibility in the chemical and physical properties [18-20]. Among these conductive polymers, a poly (3-hexylthiophene-2.5-diyl) (P3HT) as an electron donor source is the most widely used material in optoelectronic devices [21-26], owing to its high absorption coefficient and electrical conductivity [27-28]. Additionally, P3HT-graphene bilayer structure shows effective charge transfer at the interface facilitating the movement of photogenerated holes from P3HT to graphene, whereas remaining the photogenerated electrons in P3HT [29]. A recent study has shown that P3HT could be used to modify Si surface as an electron blocking layer in graphene/Si Schottky junction solar cell [30]. The power conversion efficiency of the device reaches to such a value that even exceeds 10 %, suggesting the great potential for large scale photovoltaic application. P3HT-graphene hybrid composite has also been utilized as active channel in photodetectors exhibiting great photocurrent and gain [29, 31].

Structural differences between the graphene and Si lead to the formation of defects at the interface and limit the stability and performance of the Schottky devices. Recent studies have shown that, the graphene-Si Schottky junctions have focused on effect of different annealing temperatures on electronic transport behavior [32-35] and determination of Schottky barrier height, ideality factor and series resistance parameters from current-voltage characteristic [36-38]. However, there is still lack of studies on improving charge transfer between graphene-Si interface. SAMs are a good choice for the modifying Si surface to provide compatible interface between graphene and Si, as well as they enhance charge transfer from Si surface to graphene. Additionally, SAMs are promising materials in organic electronics due to the their flexibility in the chemical structure (choosing convenient donor and acceptor groups) [39] ability in changing the physical properties (such as absorbance spectrum, extinction coefficient and energy levels) [40], easy to synthesized and purified [39-40]. In recent studies, SAMs in graphene field effect transistors have been used as a seed layer in graphene-dielectric interface to improve device performance [41-50]. Common aim of these studies are to passivate dielectric surface with SAMs resulting in reducing charge traps at the graphene-dielectric interface, limiting unintentional doping and increasing field effect mobility.

In this thesis, 5-[(3-methylphenyl) (phenyl) amino] izoftalic acid (MePIFA) and 5-(diphenyl) amino] izoftalic acid (DPIFA) aromatic small molecules with double bound carboxylic acid, 4′′bis(diphenylamino)-1,1′:3′′,-terphenyl-5′carboxylic acid

(TPA) and 4,4-di-9H-carbazol-9-yl-1,1′:3′1′-terphenyl-5′carboxylic acid (CAR) aromatic SAMs with single bound carboxylic acid were used to modify n-Si surface. Electrical characteristics of graphene based Schottky devices were investigated after the modification of n-Si substrates with MePIFA, DPIFA, TPA and CAR SAMs. The results show that SAMs modified graphene/Si devices exhibit better diode performance than bare graphene/Si device in terms of turn-on voltage, barrier height and series resistance. Additionally, we fabricated P3HT-graphene bilayer electrodes for use in Si-based Schottky junction photodetectors operating at a wide spectral wavelength range between 400 and 1100 nm. UV-vis absorbance and Raman spectroscopy measurements were conducted in order to determine the optical characteristics of P3HT coated monolayer graphene. The electronic and optoelectronic characterizations of graphene/Si samples were done before and after coating their graphene electrodes with P3HT molecules. Time-resolved photocurrent spectroscopy measurements showed that P3HT-graphene/Si samples exhibit enhanced photodetector performance compared to uncoated graphene/Si devices in terms of photoswitching characteristics, spectral responsivity, specific detectivity and noise equivalent power. The enhancement in the device performance is attributed to the effective charge transfer doping from P3HT to graphene under light illumination, which increases the magnitude of the built-in potential and widen the depletion region in the Si substrate underneath.

CHAPTER 2

GRAPHENE

2.1. Graphene and its Properties

Graphene is a one atomic thick sheet of sp^2 bonded carbon atoms arranged in a honeycomb crystal lattice that can be thought of as two dimensional material [51]. Linear energy-wave vector relation [52], zero band gap semiconductor and relativistic movement of electron in graphene lead to show superior properties [53]. In addition, graphene has ultra-fast carrier dynamics [53], wavelength independent absorption and tunable optical properties via electrostatic doping [54-55]. All these unique properties of graphene lead to completely new innovate ideas on optoelectronic devices.

2.2. Structure of Graphene

As mentioned previously, graphene is a plane of carbon atoms formed as hexagonal honeycomb lattice due to their sp^2 hybridization. For ground states, each carbon atoms involves six atoms occupying $1s^2$, $2s^2$ and $2p^2$ of atomic orbitals, where two of them fills the inner shell and the others occupy outer shell of $2s$ and $2p$ ($2p_x$, $2p_y$ and $2p_z$). In excited state, available four quantum mechanical states as configurated of $|2s\rangle$, $|2p_x\rangle$, $|2p_y\rangle$ and $|2p_z\rangle$ in orbitals. A superposition of $|2s\rangle$ with $n|2p_j\rangle$ states is named sp^n hybridization. Graphene forms sp^2 hybridization: superposition of $2s$ with two $2p$ orbitals ($2p_x$ and $2p_y$) and they aligned in the xy-plane at angle of 120^o. Therefore, each atom has a strong covalently bonded to the nearest three atoms which is called σ-bond, resulting in forming hexagonal lattice through the xy-plane. The left unhybridized $2p_z$ orbital lies horizontal to the plane (π-electron). Thus, an atom with three neighbors in graphene has three σ-bonds and six π-bonds correspondingly. While σ-bonds are responsible for mechanical strength of the graphene, π-bond provides the electronic properties of graphene at low energy levels. Additionally, the π electrons in graphene are very close to the Fermi surface as compared to σ electrons in graphene. Therefore, the energy dispersion of π electrons is solely regarded for electronic band structure of graphene.

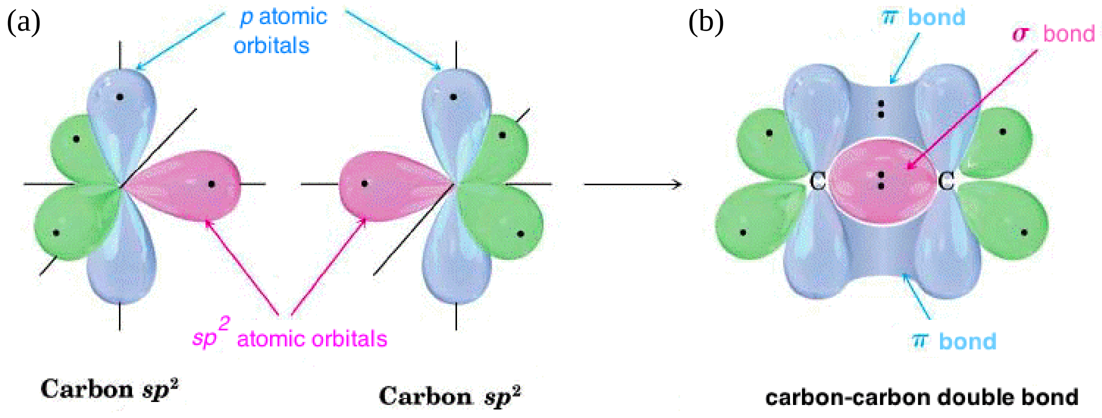

Figure 2.1. (a) Sp^2 configuration of carbon atoms and (b) formation of π and σ bonds in graphene [56].

Figure 2.2 depicts the hexagonal honeycomb lattice of graphene including two atoms (A and B) per unit cell with a lattice constant of a=2.46Å. The length between carbon atoms is about 0.142 nm [57]. The real space lattice vectors a_1 and a_2 can be written as

$$a_1 = a\left(\frac{3}{2}, \frac{\sqrt{3}}{2}\right), \; a_2 = a\left(\frac{1}{2}, -\frac{\sqrt{3}}{2}\right) \tag{2.1}$$

where a is the lattice constant and the reciprocal lattice vectors can be calculated as following,

$$b_1 = \frac{2\pi}{a}\left(\frac{1}{3}, \frac{\sqrt{3}}{3}\right), \; b_2 = \frac{2\pi}{a}\left(\frac{1}{3}, -\frac{\sqrt{3}}{3}\right) \tag{2.2}$$

Figure 2.2 indicates shows first Brillion zone of graphene. *Γ* is the zone center, *M* is the midpoint, *K* and *K*' are two nonequivalent corners of first Brillion zone, respectively. Especially, the corners of Brillion zone (*K* and *K*') are quite important. Since the fascinating physics of graphene arises at these corners which are named Dirac points. At these Dirac points, which have two different sets. Each set is nonequivalent and involved three Dirac points. While one of set labeled as *K*, the other labeled as *K*'. Corresponding positions in momentum space are given by

$$K = \frac{2\pi}{3a}\left(1, \frac{1}{\sqrt{3}}\right),\ K' = \frac{2\pi}{3a}\left(1, -\frac{1}{\sqrt{3}}\right) \tag{2.3}$$

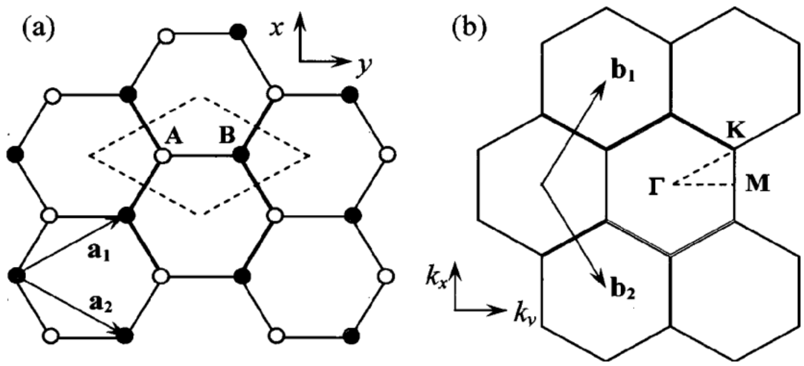

Figure 2.2. (a) Real lattice structure and (b) First Brillion zone of reciprocal lattice of graphene [58].

2.3. Electronic Properties of Graphene

To determine the electronic properties of graphene, π-electrons play a critical role. The honeycomb lattice of graphene are separated by the energy levels of π-bond orbitals into two energy bands including π and π^* bands corresponding to valence and conduction band, respectively. Valence and conduction bands of graphene meets at point at each of *K* and *K*' symmetry points, but do not overlap due to zero number of density of states which are proportional to the absolute value of energy. Because of the fact that each p_z orbital is filled by one electron of spin for each atom in the unit cell, the energy bands of intrinsic graphene are completely half-filled and the intrinsic Fermi-level of graphene is placed at middle of the bands (the Dirac points).

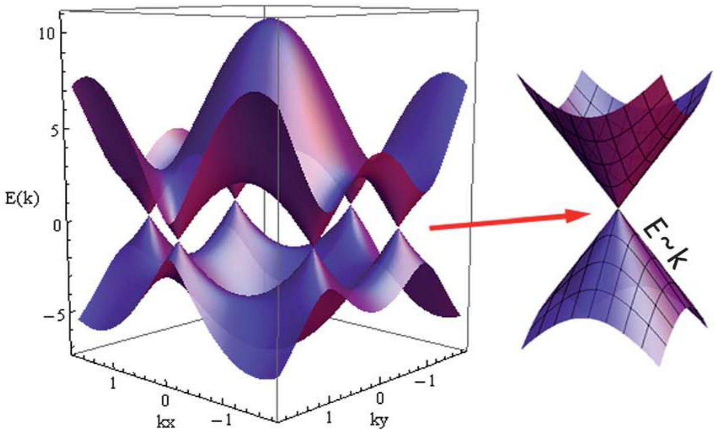

Figure 2.3. Dispersion relation of graphene first Brillion zone [59].

Using tight binding approximation, energy dispersion relation or band structure of graphene can be acquired by taking into account only the interaction of carbon atoms to nearest carbon atoms and given below relation [60]

$$\mathrm{E}(\mathrm{k_x}, \mathrm{k_y}) = \pm \mathrm{t}\sqrt{1 + 4\cos\left(\frac{\sqrt{3}\mathrm{k_x a}}{2}\right)\cos\left(\frac{\mathrm{k_y a}}{2}\right) + 4\cos^2(\frac{\mathrm{k_y a}}{2}}) \tag{2.4}$$

where t is nearest hopping energy nearly equal to 2.7 eV [60-61], k_x and k_y are k momentum components in x and y in-plane directions. The energy bands of intrinsic graphene are completely half-filled and the intrinsic Fermi-level of graphene is placed at middle of the bands (the Dirac points). Energy dispersion around K (or K') points can be expressed as [62]

$$E \approx \hbar \upsilon_{\mathrm{F}} |\mathrm{k}'| \tag{2.5}$$

where k' is the wave vector and υ_F is the Fermi velocity. Energy dispersion relation of graphene displays linear behavior around Dirac points compare to other semiconductor which shows parabolic dispersion characteristics. This linear dispersion gives rise to energy-irrelevance Fermi velocity such as massless Dirac fermions making graphene unparalleled systems with carriers behaving like relativistic particles traveling at the Fermi velocity [63]. This relativistic process has to do with a chiral tunneling in which an incident electron goes into a potential barrier. (when the barrier height is higher than electron's kinetic energy). As compared to the non-relativistic tunneling in which the transmission probability (*P*) has an exponential decay with raising the barrier height, the *P* increases with increasing the barrier height, which is called *Klein tunneling*. For an electron in diffusive conductor, *P* is directly related on the distribution of scatters while Dirac fermions *P* remains constant but depends on the carrier incident angle [64].

2.4. Vibrational Properties of Graphene

Vibration properties of graphene can be understood with help of phonon dispersion relation. The unit cell of graphene consists of 2 carbon atoms A and B, where six phonon dispersions are existed (Figure 2.4 (a)).

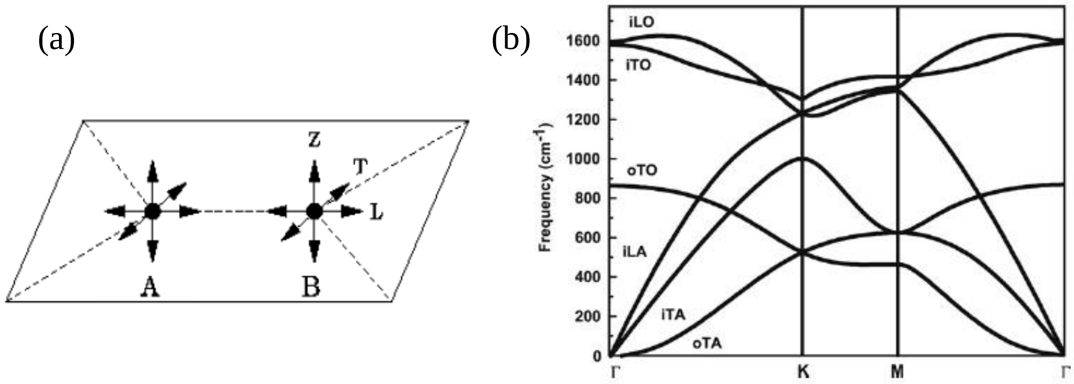

Figure 2.4. (a) Motions of two carbon atoms in graphene through the out-of-plane (Z), in-plane transverse (T), and in-plane longitudinal (L) direction. (b) Phonon dispersion relation of graphene [65].

While three of them are acoustic phonon branches (A), the others are optical (O) phonon branches. For one acoustic branch (A) and one optical (O) phonon branch, directions of atomic vibrations are aligned perpendicularly to the graphene plane specified as out-of plane (o) phonon modes. Direction of vibrations is parallel in the graphene plane (i) for two acoustic and two optic phonon branches. Therefore, the phonon modes are categorized as longitudinal (L) or transverse (T) with respect to the direction of atomic vibrations parallel or perpendicular to the carbon-carbon (A-B) directions. The six phonon dispersions are given as iLO, iTO, oTO, iLA, iTA and oTA, respectively (Figure 2.4 (b)). Figure 2.5 shows first brillion zone and out of plane modes. The gray surface corresponds to optical mode, whereas the pink surface is acoustic mode. The dispersion is quadratic at the Γ point, which is unusual for acoustic modes [66].

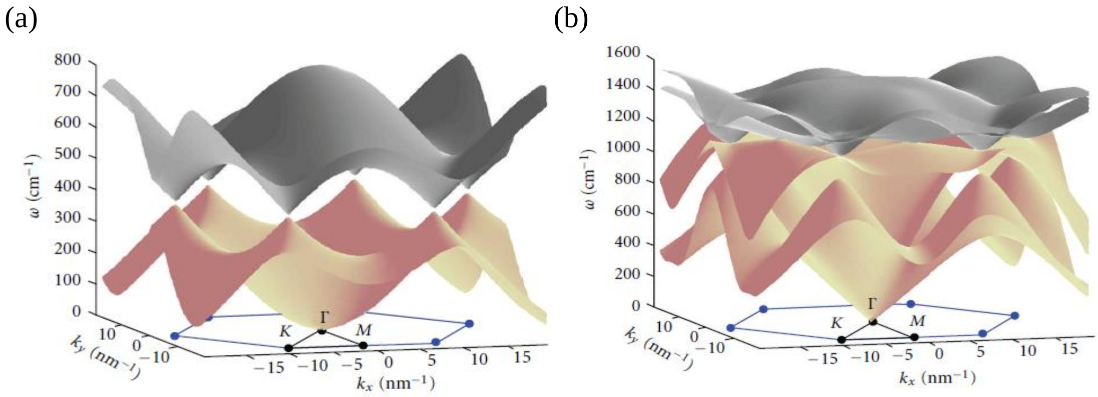

Figure 2.5. The dispersion relation of (a) out-of-plane modes and (b) in-plane modes [66].

The dispersion has conic shape at K and K', which have density of states owing to the existence of in-plane modes. The in-plane has two acoustic modes (TA and LA) and two optical modes (TO and LA), shown in Figure 2.5 (b). Transverse modes exhibit the same trends with longitudinal modes but have lower frequency for both acoustic and optical modes. The dispersion is linear at the Γ point.

2.5. Optical Properties of Graphene

Due to the zero-band gap nature, graphene can be absorbed photons of all frequencies within the spectral range between UV and terahertz. Therefore, the absorption of graphene can be divided into two types of process involving intraband and interband optical transition. Intraband transition occurs at low photon energies (from FIR to terahertz spectra range) whereas interband transition exists at higher photon energies (from MIR to UV range). For intraband transition, optical absorbance is constituted by free-carrier and can be described by Drude model. Frequency dependent sheet conductivity of the Drude model can be written as [62, 67]

$$\sigma(\omega) = \sigma_0/(1 + i\omega\tau) \qquad (2.6)$$

where σ_o is the dc conductivity, τ is the electron scattering time and ω is the angular frequency of the light. Optical conductivity of graphene is related to optical absorbance of graphene in terms of $A(\omega) = (4\pi/c)Re[\sigma(\omega)]$. Interband transition, optical absorbance is occurred between valance and conduction bands. According to the tight banding model, optical conductivity of graphene is directly related to frequency-independent at zero temperature and described by [55]

$$\sigma(\omega) = (\pi e^2)/2h \qquad (2.7)$$

This conductivity of graphene depends on an absorbance of graphene with the relation of $A(\omega) = (4\pi/c)\sigma(\omega) = \pi\alpha = 2.29\ \%$ where α is the fine structure constant. This value is quite high when considering just one atom thick of materials. In addition to this, for a single layer of graphene, it reflects < 0.1 % incident light in the visible region [68] and it has a ~ 97.7 % transparency. However, each additional graphene layer increases absorption ($\pi\alpha$ = 2.29 %) linearly and can be tuned by electronic gating which shifts the Fermi level and causes Pauli blocking of optical transition.

2.6. Graphene as Electrode Material

Since its discovery in 2004, graphene has gained an increasing amount of attention over the past few years due to the owing to its high charge carrier mobility [6], superior optical transparency[7] and modulation of Fermi level[8]. Contrary to conventional transparent conductive electrode, where the Fermi level remains constant, even small variations in charge carrier density can considerably alter the Fermi level of graphene which results in enabling to modify device properties. Accordingly, graphene is considered to be used as transparent conductive electrode alternative to ITO in microelectronic and optoelectronic devices operating with low leakage currents.

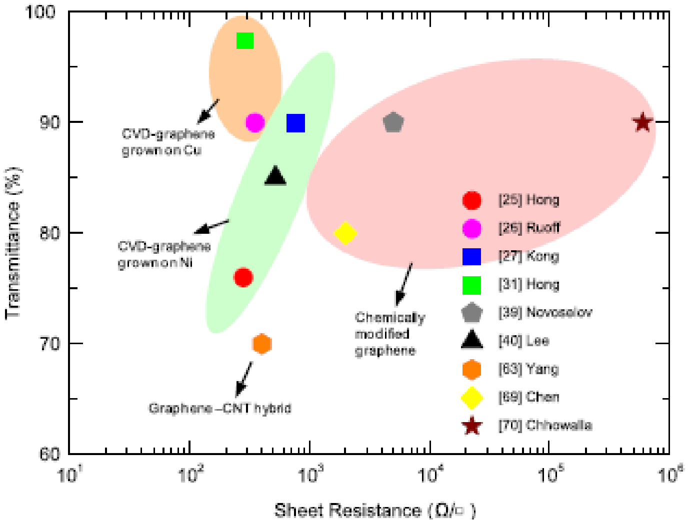

Figure 2.6. Optical transmittance and sheet resistance of graphene films reported by several groups[69].

Figure 2.6 indicates optical transmittance as a function of sheet resistance of graphene films reported by several groups. To use graphene as transparent electrode for a large area, graphene shows relatively low sheet resistance and high transmittance. It is also well known that contrary to reduced graphene oxide which has lower uniformity due to the stacked graphene flake, Chemical Vapor Deposition (CVD) grown graphene on Cu foil exhibits relatively high uniform, high transmittance and low sheet resistance. Therefore, CVD grown graphene can be widely preferred as compared to other growth methods. Although graphene with hybrid or chemically modified has relatively low transmittance or low sheet resistance, they can be vigorously used as transparent electrode depending on a variety of desired device applications.

2.7. Extrinsic Charge Carriers in Graphene

For basal plane of graphene, carbon atoms have a strong covalently bonded to the nearest neighbors which are called σ-bonds. The bonds are chemically inert at ambient. For suspended graphene, small ripples exist which is local flexure regions [70]. These imperfections diminish activation barrier that is considered chemically bonded. Although activity of the in plane carbon atoms in graphene increases in ambient conditions, interactions with surrounding molecules are occurred at edge and defect sites in which fracture aromatic chains are naturally sensitive [71]. In contrast to the bound σ electrons, the charge carriers in graphene are provided by delocalized π -orbitals lies horizontal to the plane. Due to the 2D nature of graphene, surrounding molecules cannot exceed the Debye length which is the measure of how far a charge carrier's net electrostatic effect continues. Therefore, charge carriers adjacent to other charge can be attracted with it. The near the Dirac point, self-screening is weak due to the low density of states and meaning that the adjacent charge of even a single molecule can be sensed by variations in the average energy of electrons on the Fermi surface [72]. Therefore, a charge transfer between graphene and surrounding molecules give rise to shift the Fermi level of graphene, and thus altering the charge carrier density in the graphene. Accordingly, the charge carrier density in graphene can be manipulated in a various ways: atomic or molecular charge transfer doping [73-75], substitutional doping [76-78], contact to metals [79-80], substrate interactions [81-82], or application of a gate field [83].

2.8. Production of Graphene

Synthesis method is great importance to produce high quality graphene. Three growth methods have been utilized so far, the first one is mechanical exfoliation in which graphite is used as source material to separate multiple layers, the second one is the sublimation of Silicon Carbide (SiC) in Ultra High Vacuum (UHV) condition and the last one is about formation of graphene on a metal substrate by CVD using carbon precursor as source materials. Each technique has its own advantages and drawbacks in terms of the cost, production and material characteristics.

2.8.1. Mechanical Exfoliation of Graphene

A. Geim and K. Novoselov received the 2010 Nobel Prize for the discovery of graphene, which was obtained by the mechanical exfoliation method [84]. In this method, scotch tape is used to press down on a photolithographically patterned Highly Ordered Pyrolytic Graphite (HOPG). After repeated peeling, monolayer graphene can be easily removed from the HOPG due to weak van der Waals attraction between HOPG layers. At the end, the carbon sheet can be single or multilayer graphene with high quality. In order to identify number of layers, graphene from the adhesive tape can be transferred to SiO_2/Si substrate by gentle pressing and then observing color difference under optical microscopy.

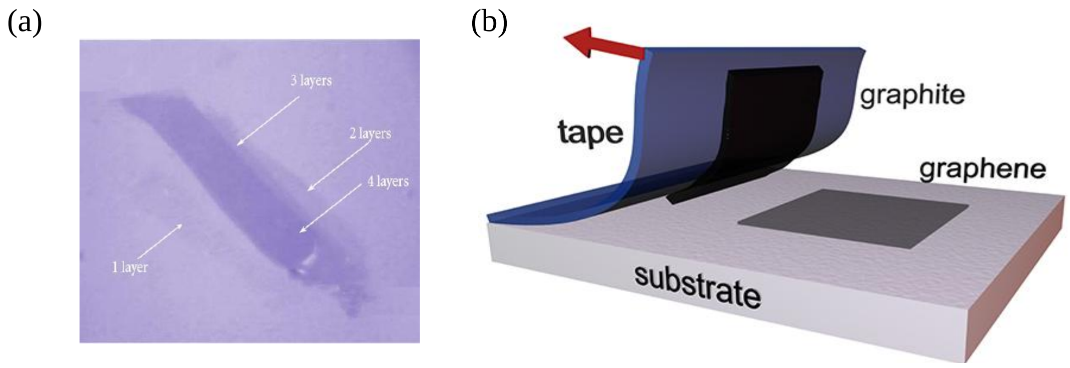

Figure 2.7. (a) Optical image of multilayer graphene. Image size 120 x 110 μm^2 [85]. (b) The mechanical exfoliation of graphene from graphite using Scotch tape [86].

Figure 2.7 (a) shows optical image of graphene transferred by mechanical exfoliation on to SiO_2/Si substrate. Lightest purple flake indicates single layer graphene while the other flakes represent 2, 3 and 4 layered graphene with increasing darker region, respectively. Although this method is very reliable and easy technique and graphene flakes can be distinguished under an optical microscope in visible range, exfoliated graphene has lots of defects and limited in small sizes. Another drawback of this method is that graphene flake control is also hard and graphene has irregular shape. For the use of graphene in commercial applications, large-area and defect-free graphene are needed.

2.8.2. Thermal Decomposition of SiC

The second method used to obtain high quality graphene is the thermal decomposition of SiC, which involves high temperature (> 1000 ^{o}C) and UHV conditions. Annealing of SiC at high temperatures leads to sublimation of Si result that graphitization of remaining carbon is obtained [87] and graphene grows on both silicon rich face (0001) and carbon rich face (4H-SiC or 6H-SiC).

High temperature vacuum annealing of SiC gives rise to highly wrinkled surface covered by graphene domains with different thicknesses. The solution for this problem was achieved by graphitization under non reactive Ar gas ambient which decreases sublimation rate of Si atoms due to higher temperature. As a result of this, smoother surface covered by graphene domains are synthesized. Also, by controlling annealing time, temperature and argon pressure, single or few layers graphene can be formed on an insulating substrate which is compatible for wafer-based applications. However, this method has its own drawbacks; for example, Unlike CVD method which will be addressed in section 2.7.3, transfer process to other substrates is not an easy task due to difficulties of removal of SiC, In addition this, thickness control of layers, reproducibility of large area graphene and low graphene quality need to be addressed before adopting at semiconducting industry.

2.8.3. Chemical Vapor Deposition

The most widely used graphene synthesis method is CVD, which involves chemical reaction of a vapor near or at heated surface. In the CVD method, gas, liquid or solid precursor, mainly hydrocarbons and polymers are used as carbon source reacting with metal catalysts at high temperatures (800 - 1000 ^{o}C) [88]. Figure 2.8 depicts the schematic diagram of a thermal CVD grown graphene using CH_4/H_2 gas mixture. The detailed explanation is listed as follows; (1) Reactants are transported by forced convection. (2) Thermal activation. (3) Reactants are moved by diffusion of gas from main gas to the substrate surface. (4) Reactants are adsorbed on the substrate surface. (5) Depending on the solubility of carbon and physical properties of the substrate, bulk diffusion takes place in the substrate. (6) Thermal activation and surface processes occurs containing catalytic decomposition and reaction, resulting in graphene growth. (7) By-products are desorbed from the surface. (8) Convection of by-product by diffusion along the surface and return to the main gas flows. (9) Carrying of by-products far away from the deposition zone via forced convection.

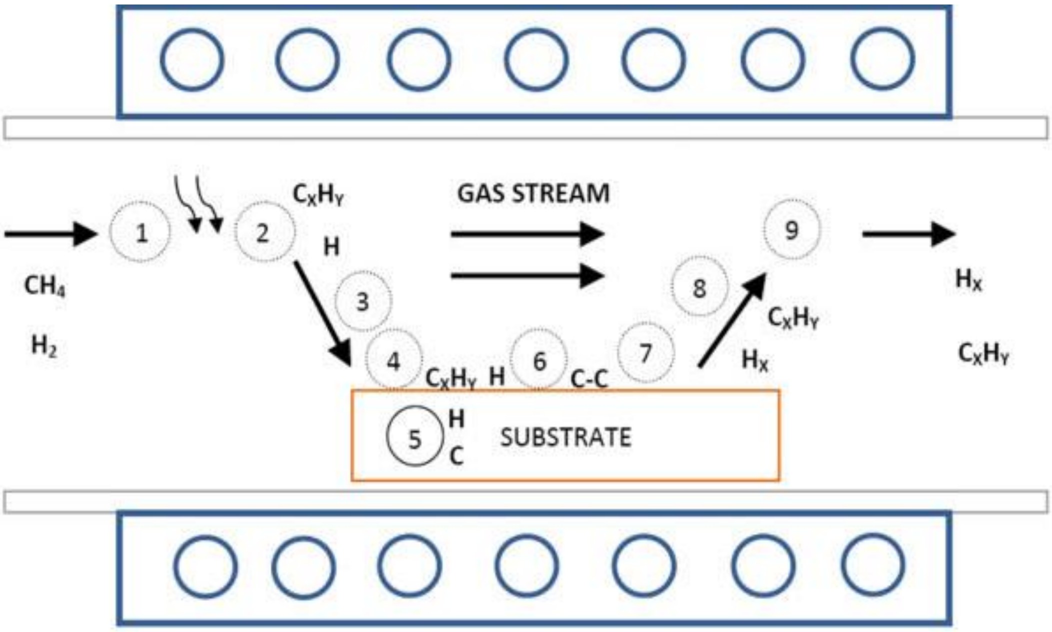

Figure 2. 8. Schematic diagram of a thermal CVD grown graphene [89].

The growth of graphene with CVD consists of many steps including heating, annealing, growing and cooling, respectively. The detailed process is explained as step-by-step. Heating; heating catalyst-substrate up to pre process temperature. Annealing; catalyst-substrate is annealed to remove oxide from the surface and change surface morphology including grain size, crystal orientation and roughness of a catalyst substrate. Growing; carbon precursor is introduced CVD chamber leading to nucleation of graphene by thermal cracking of C atoms on substrates. Cooling, reactor is cooled in a proper temperature to avoid oxidation of surface and graphene functionalizations involving oxygen groups. Additionally, working high carbon solubility catalyst-substrate such as Ni, cooling process plays important role in growing graphene and controlling thickness of graphene.

Gas, liquid and solid precursor of hydrocarbons has been used as graphene growth. Commonly, methane (CH_4), ethylene (CH_2) and acetylene (C_2H_2) hydrocarbons gases would be preferable and C-H (3.72 eV for CH_4) bond energy is the key parameter to growth graphene [90-91]. Among these hydrocarbons, CH_4 is most preferred material due to its good thermal stability to avoid pyrolysis at high temperatures [92]. Other hydrocarbons have a very high pyrolysis rate at high temperature which gives rise to large amount of carbon deposition on a catalyst-substrate that cannot be compatible with sub-nanometer graphene.

Hydrogen (H_2) plays important role in growing graphene and widely utilized to clean and crystallize the catalyst-substrate. The advantage of using H_2 is that H_2 penetrates into the catalyst-substrate with CH_4 to form the initial physical adsorption and deactivate defects and grain boundaries. Also, H_2 gives rise to dehydrogenation of CHx deposition or C-etching; and it leads to sp^3 to sp^2 transition [89].

Transition metals such as Copper (Cu) [93], Nickel (Ni) [94], Palladium (Pd) [95] and Ruthenium (Ru) [96] foils or films have been utilized as catalysts-substrate in graphene growth. Among those, the most commonly used transition metals are Cu and Ni. Compare to Ni, Cu has very low solubility of carbon, which is the key parameter to the control number of graphene layers. As a result of low solubility, Cu and carbon generate weak bond by means of charge transfer between the π electrons in the sp^2–hybridized carbon and empty 4s states of Cu [89]. This consolidation of low affinity between the carbon and cupper gives rise to graphitic carbon formation easily. The CVD method has many controllable parameters that result in synthesis of large size graphene up to 30 inches [97]. In addition, the CVD method can be used for the substitutional doping process by sending heteroatoms such as nitrogen and boron, which will support the functionalizations. Furthermore, CVD grown graphene could be patterned by microfabrication techniques which give rise to the production of miniaturized devices and high density electric circuits.

CHAPTER 3

PHYSICS OF SCHOTTKY JUNCTION

The junction between a metal and a semiconductor plays a crucial role in the realm of semiconductor device technology. The charge carrier transport such junction is directly related to work function of metal and Fermi level of semiconductor, respectively. The difference between energy levels designate charge carriers across the junction will be ohmic (resistive) or Schottky (rectifying) characteristic. Ohmic junction is occurred with heavily doped semiconductors and the current shows a linear dependence with applied voltage. For Schottky junction, rectifying behavior is formed between metal and light doped semiconductor and the current exhibits an exponentially dependence with applied voltage. Additionally, the rectifying characteristic was first observed by Braun in 1874 [98] and then proposed a model of barrier formation by Schottky and Mott in 1930's [99]. Today Schottky junction is widely used in many applications including barristors, solar cells, photodetectors and sensors.

3.1. Formation of Schottky Barrier

3.1.1. Schottky-Mott Model

As mentioned previously, when a metal and semconductor are brought into contact, two different junction, which is called ohmic and Schottky, occurs depending on the work function of metal and Fermi level of semiconductor. For n-type semiconductor, if the work function of metal is high compared to the work function of semiconductor ($\varphi_M > \varphi_S$), electrons in semiconductor tend to flow into metal until the alignment of work function of metal and the Fermi level of semiconductor after the contact. The difference between metal and semiconductor materials gives rise to energy barrier which is called Schottky barrier (Figure 3.1 (a)). By using Schottky-Mott model for n-type semiconductor, the Schottky barrier height (SBH) can be written as [100]

$$\varphi_B = \varphi_M - \chi \tag{3.1}$$

where φ_B is the Schottky barrier height, φ_M is the work function of material and χ is the electron affinity of the semiconductor, respectively. For n-type semiconductor, while charges jump across the junction at the equilibrium, a space charge layer, which is called depletion region, is formed in semiconductor which creates built in potential (V_{bi}). Such a potential leads to collect carriers near the interface and the Femi level lines up bending energy bands from n type semiconductor to metal. Under forward bias condition, meaning that negative voltage is applied as compared to metal. Barrier decreases an amount of $q(V_{bi} - V)$ where V is the applied voltage. Hence, electrons from metal into semiconductor are facilitated due to reduction of barriers (Figure 3.1 (b)). Contrary to forward bias, semiconductor to metal barrier enhances by $q(V_{bi} + V)$ for applied reverse bias. This increasing in the barrier prevents electrons from semiconductor to metal (Figure 3.1(b)). For p-type semiconductor, if the work function of metal is lower than the work function of semiconductor ($\varphi_M < \varphi_S$), Schottky junction is formed at the interface and SBH can be expressed as [100]

$$\varphi_B = E_g - (\varphi_M - \chi) \tag{3.2}$$

where E_g is the band gap of semiconductor, Both ohmic and Schottky junctions configuration are summarized in Table 3.1 for n-type and p-type semiconductors.

Table 3. 1. Combination of metal-semiconductor junctions.

Work function relation	**n-type semiconductor**	**p-type semiconductor**
$\varphi_M > \varphi_S$	Schottky	Ohmic
$\varphi_M < \varphi_S$	Ohmic	Schottky

However, the Schottky-Mott model has its own drawbacks. Since model provides information about the SBH for an ideal condition. Actually, some other effects should

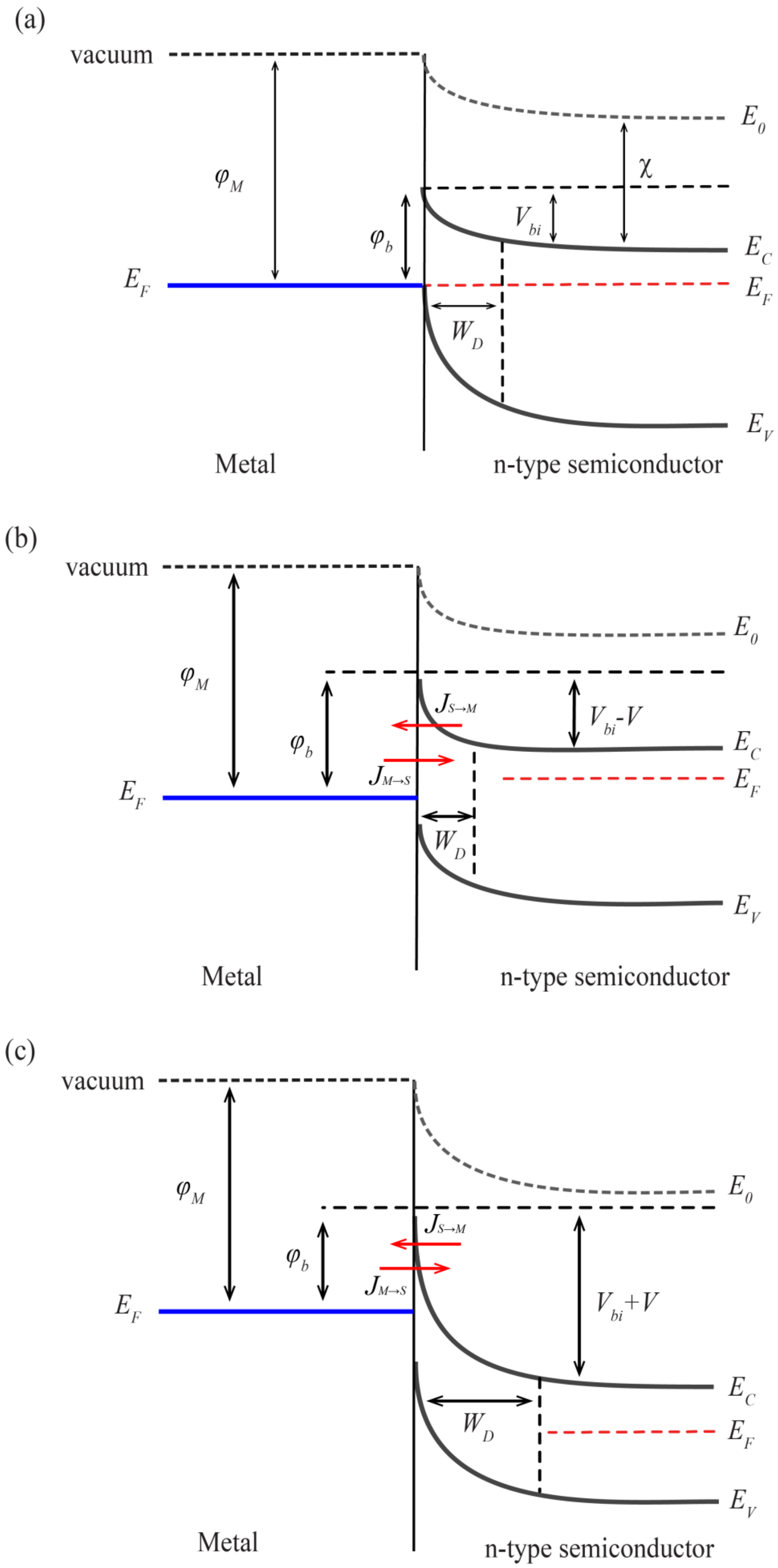

Figure 3.1. Energy band diagram of metal-semiconductor junction (a) thermal equilibrium, (b) forward bias and (c) reverse bias condition.

be taken into account such as interfacial layer from Si with native oxide, surface states, defects, image force lowering and Fermi-level pinning to define expected values of SBH. All those effects are given with detailed following subsections. For clarity, the next following discussions will be focused on n-type semiconductor.

3.1.2. Image Force Lowering

An electron at a distance x far away from metal will induce a polarization positive charge inside the metal at the opposite distance. This positive charge is specified as the image charge and the attractive Coulomb force *F(x)* between electron and its image is called an image force (Figure 3.2).

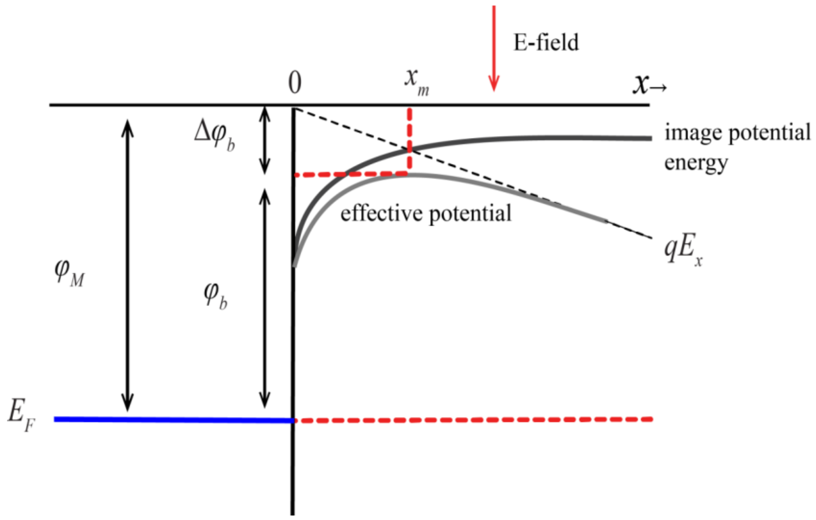

Figure 3.2. Image force lowering under electric field.

Such force can be expressed as

$$F(x) = \frac{e^2}{4\pi\epsilon_0\epsilon_S(2x)^2} = -qE \tag{3.3}$$

where ϵ_s = 8.85 $x\ 10^{-12}$ F/m is the vacuum permittivity, ϵ_s is the relative permittivity of the semiconductor. Therefore, potential energy is given by

$$U_{im} = \int_{\infty}^{x} F(x')dx' = -\frac{e^2}{16\pi\epsilon_0\epsilon_S x} \tag{3.4}$$

Considering electrical potential across depletion region, *V(x)* is the total electrical potential energy is written as

$$U(x) = U_{im} - eV(x) = -\frac{e^2}{16\pi\epsilon_0\epsilon_S x} - \frac{e^2 N_D}{\epsilon_0\epsilon_S}\left(W_D x - \frac{1}{2}x^2\right) \tag{3.5}$$

If the image charge is close to metal-semiconductor interface ($x<< W_D$), then x_m is calculated as

$$x_m = \sqrt{\frac{1}{16\pi N_D W_D}} \tag{3.6}$$

where N_D is the density of shallow donor ions and W_D is the depletion region . The change in the barrier height ($\Delta\varphi$) is determined as

$$\Delta\varphi = \frac{e}{\epsilon_0\epsilon_S}\sqrt{\frac{N_D W_D}{4\pi}} \tag{3.7}$$

effective SBH (φ_{Bn}) can be written as

$$\varphi_{Bn} = \varphi_{Bn}^0 - \Delta\varphi \tag{3.8}$$

where φ_{Bn}^{0} is the SBH at zero bias. It should be noted that while $\Delta\varphi$ reduces under forward bias because of the fact that the W_D is lightly decreased, $\Delta\varphi$ increases in reverse bias with increasing the W_D. Additionally, the values of $\Delta\varphi$ is about tens of meV for Si. Therefore, image force lowering does not strongly contribute to total SBH. Especially, Si-based Schottky junction including high work function metal ($W > 4.8\ eV$) like heavily hole doped graphene [100].

3.1.3. Bardeen Model

As mentioned previously, the Schottky-Mott model has its own drawbacks and disregards the existence of surface states. Therefore, the model does not work truly most of the metal-semiconductor contact [101]. Bardeen was developed a model which derivates from the Schottky-Mott model by emphasizing inadequacy of the model [102]. The model purposes additional presence of surface states at metal-semiconductor interface which the corresponding Fermi level is pinned. This is also known as Bardeen limit. Figure 3.3 shows energy band diagram of metal- n-type semiconductor containing interfacial layer and surface states. When the Fermi level E_F is aligned with φ_0 that is the charge neutrality level at the surface of semiconductor, energy level below E_F is occupied by surface states which is called acceptor type and above E_F is unfilled which is donor type. As a result, the interface-trap charge is zero. On the other hand, when the E_F can be above (below) φ_0, the interface-trap charge density on the semiconductor (Q_{ss}) is negative (positive) and can be expressed as [100]

$$Q_{ss} = -qD_s\left(E_g - q\varphi_0 - q\varphi_{Bn} - q\Delta\varphi\right) \tag{3.9}$$

where D_s is the density of surface states per unit area per energy and $\Delta\varphi$ is Schottky barrier lowering. It should be noted that when D_s is too broad, Q_{ss} indicates a quite alteration even if the little shifting between the Fermi level and neutrality level. Additionally, in the case of E_F is below the φ_0, this excess Q_{ss} counterbalance the charge transferred from metal and remains fixed fermi level to the charge neutrality level which is called the Fermi-level pinning. Using Bardeen model, the SBH can be expressed as

$$q\varphi_{Bn} = E_g - q\varphi_0 \tag{3.10}$$

where $\varphi_0 = E_F - E_V$. It should be pointed out that SBH is the independent of metal's work function and is designated surface properties of semiconductor.

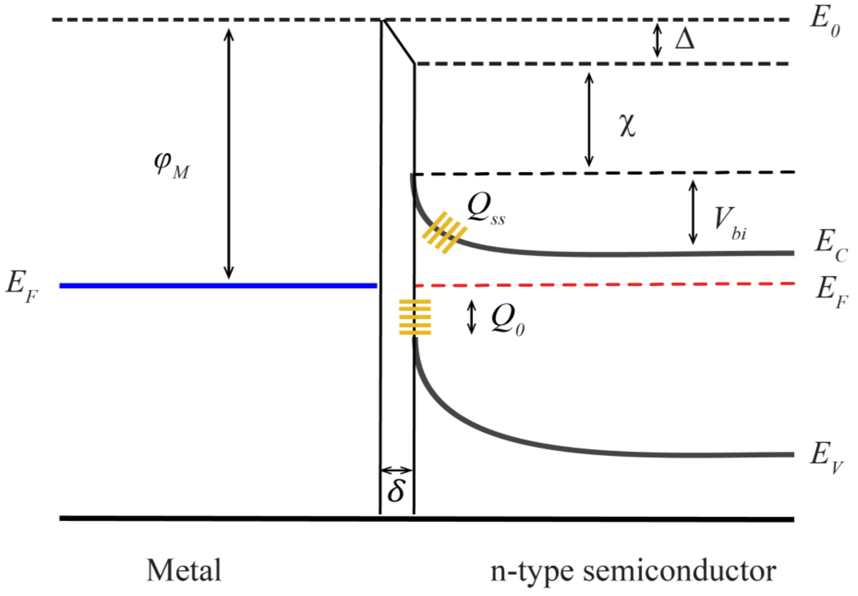

Figure 3.3. Energy band diagram of metal-semiconductor junction involving interfacial layer and surface states.

3.2. Charge Depletion Region

When metal and semiconductor are come into contact with each other, electrons in semiconductor are tended flow into metal until the Fermi levels are aligned across the junction. Owing to the low charge carrier density on semiconductor side, electrons are removed both surface and certain depth in the semiconductor. This gives rise to establish depletion region in the semiconductor underneath resulting in a built-in potential at the region. Additionally, during the alignment between their corresponding the Fermi levels. Band bending in the energy levels occurs on the semiconductor side. In order to identify Schottky junction formation, Poisson equation can be used and also provided important information including electric potential, electric field, depletion region width and interface capacitance, respectively.

3.2.1. Abrupt Junction Approximation

Abrupt Junction Approximation (AJA) is first developed for p-n junctions which the charge distribution at the interface was assumed to have a box profile. When the resemblances between p-n junction and Schottky junction are considered, AJA can be applied to Schottky junction on the semiconductor side. The Poisson equation can be given with below relation [100]

$$\frac{d^2V(x)}{dx^2} = -\frac{\rho}{\epsilon_s} \tag{3.11}$$

where ϵ_s is relative permittivity of the semiconductor. Consider that shallow bands are ionized, therefore $n \approx N_D$ where N_D is the density of shallow donors. Thus, the charge density is written as

$$\rho(x) = \begin{cases} eN_D, \ 0 \leq x \leq W_D \\ 0, \ x > W_D \end{cases} \tag{3.12}$$

where W_D is the width of depletion region. In addition to this, electric field can be acquired by solving the Poisson equation at the boundary condition of $E = 0$, $x = W_{D,}$

$$E(x) = \begin{cases} \frac{eN_D}{\epsilon_0\epsilon_s}(x - W_D), \ 0 \leq x \leq W_D \\ 0, \ x > W_D \end{cases} \tag{3.13}$$

Applying boundary condition for the potential of V (x = 0) = V_{bi} and V ($x = W_D$) = 0

$$V(x) = \begin{cases} \frac{eN_D}{\epsilon_0\epsilon_s}\left(W_Dx - \frac{1}{2}x^2\right), \ 0 \leq x \leq W_D \\ V_{bi}, \ x > W_D \end{cases} \tag{3.14}$$

where V_{bi} is the built-in potential. Then the depletion region can be obtained as

$$W_D = \sqrt{\frac{2\epsilon_0\epsilon_s(V_{bi}-V)}{eN_D}} \tag{3.15}$$

where V is the applied bias voltage. It should be noted that the depletion region shows direct proportional to square root of built-in potential and inverse proportion to density of shallow donors. Additionally, when a bias is applied between metal and semiconductor, forward bias ($V > 0$) gives rise to decrement in W_D whereas reverse bias ($V < 0$) increases W_D. Furthermore, W_D and built-in potential play important role of Schottky photodetector. Meaning that larger built-in potential leads to wider depletion region providing efficient dissociations of photogenerated carries, resulting in high responsivity in the photodetector

3.3. Charge Transport Process

Contrary to p-n junction, where current transport is governed by minority carriers including both electrons and holes, in a Schottky junction, majority carriers provide the current transport across the junction with fast response. This enables advantages in the realm of low charge storage, low junction capacitance and fast recovery time as compared to conventional p-n junction. Charge transport mechanism divides into forward and reverse regime, respectively. For forward regime, charge transport is governed by thermionic emission (TE) over the barrier (dominant process for Schottky diode), diffusion of carriers across depletion region and quantum mechanical tunneling through barrier (heavily doped semiconductor) (Figure 3.4). In reverse regime, charge transport is dominated by thermionic field emission (TFE) and Poole-Frenkel emission. Furthermore, for high mobility semiconductors such as Si and GaAs, charge transport mechanism can be usually described by thermionic emission theory. However, when the low mobility semiconductors are considered, the diffusion model is feasible. All mechanisms are given with detailed discussions in the following subsections.

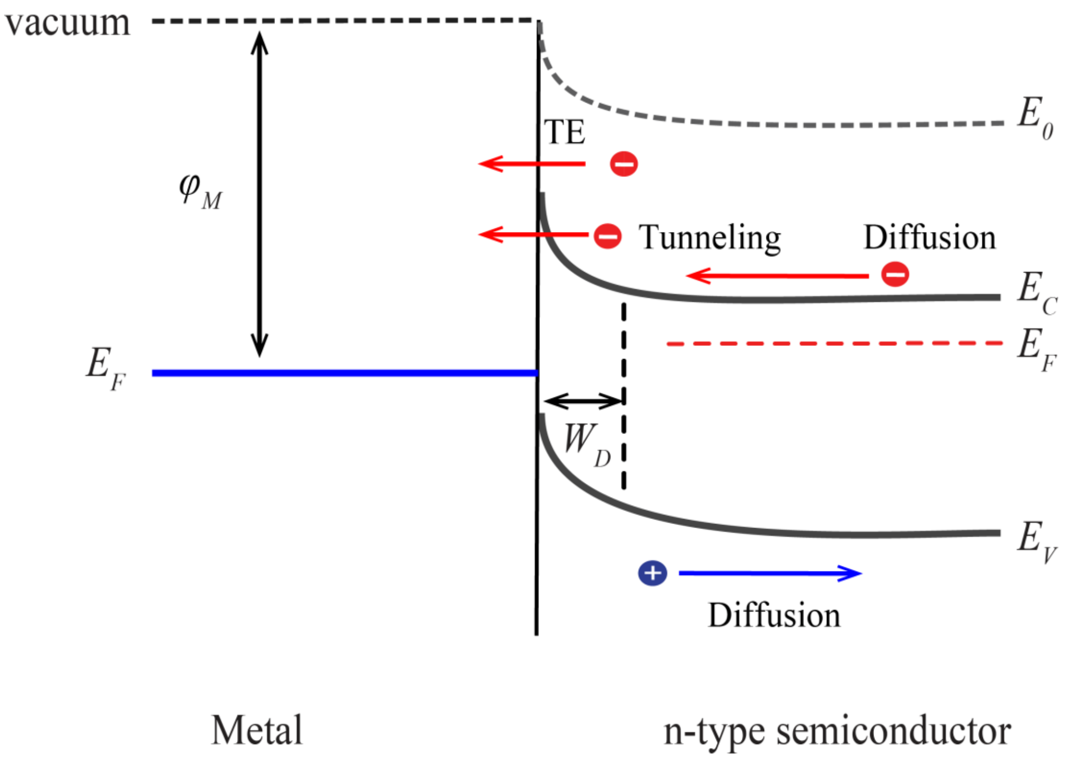

Figure 3.4. Charge transport mechanisms under forward bias condition.

3.3.1. Forward Bias Transport Mechanism

3.3.1.1. Thermionic Emission Model

TE is related to thermally activated emission over the barrier. It means that energy of charge carriers is larger than both k_BT at room temperature (25 meV) and barrier height. However, when the barrier height is relatively small (~ 1 eV), leakage current increases due to the thermionic emission at room temperature. Additionally, TE occurs in the case of energy of charge carriers have enough energy to overcome the conduction band energy at metal-semiconductor interface. Therefore, there are two density of current involving $J_{M \to S}$ and $J_{S \to M}$, respectively. The current density from semiconductor to metal can be expressed as in the following [100]

$$J_{S\to M} = T^2 \exp\left(-\frac{q\varphi_{Bo}}{kT}\right) \exp\left(\frac{qV}{nkT}\right) \tag{3.16}$$

where $A^* = (4\pi q m^* k^2)/h^3$ is the Richardson constant, *n* is the ideality factor, h is the Planck constant and m^* is the effective mass and directly related to direction of carrier transport in semiconductor. It should be pointed out that the Richardson constant is material-dependent constant depending effective mass of carriers at conduction band edge is isotropic or an isotropic. Thus, it has different values between semiconducting materials.

The current density from metal to semiconductor does not alter with applied voltage. Since barrier height is independent of the bias voltage and corresponding current density can be given by

$$J_{M\to S} = -A^*T^2 \exp\left(-\frac{q\varphi_{Bo}}{kT}\right) \tag{3.17}$$

Then total current density can be written as

$$J = J_{S\to M} - J_{M\to S} \tag{3.18}$$

$$J = A^*T^2 \exp\left(-\frac{q\varphi_{Bo}}{kT}\right)\left[exp\left(\frac{qV}{kT}\right) - 1\right] \tag{3.19}$$

$$= J_s\left[exp\left(\frac{qV}{kT}\right) - 1\right] \tag{3.20}$$

where J_s is the saturation current density. It is clear that while the current density *J* exhibits directly exponential dependent on applied voltage and inversely proportional to temperature, In addition to this, the statured current density J_s indicates exponentially dependent on Schottky barrier height. Furthermore, Major Schottky diode parameters such as Schottky barrier height, ideality factor and series resistance (R_s) can be derived from the slope (or intercept) of linear region of current density relation.

3.3.1.2. Diffusion Model

Diffusion model a well described for light doped semiconductor (low mobility or disorder semiconductors) that have the carrier diffusion length is smaller than depletion region width [103]. The current density in the depletion region is related to participate both local electric field (drift) and carrier concentration gradient (diffusion) which can be expressed as [100]

$$J = q\left[n\mu_n\varepsilon + D_n\frac{dn}{dx}\right] \tag{3.21}$$

where D_n is the electron diffusion coefficient and μ_n is the electron mobility, and shape of the depletion region designates local electric field $\varepsilon \sim dE_c(x)/dx$. Integrating current density over the entire depletion region,

$$J = qD_n n(x)\exp\left[\left(\frac{E_C(x)}{k_BT}\right)\right]_{x=0}^{W_D} \tag{3.22}$$

and assuming that the carrier concentration at boundaries stay at equilibrium, current density for diffusion theory can be obtained as

$$J = J_D\left[\exp\left(\frac{qV}{k_BT}\right) - 1\right] \approx q\mu_n N_C\varepsilon_{max}\exp\left(-\frac{q\varphi_b}{k_BT}\right)\left[\exp\left(\frac{qV}{k_BT}\right) - 1\right] \tag{3.23}$$

where J_D is the saturation current density acquired from diffusion model. The electric field exceeds a maximum value at metal-semiconductor interface and depends on the magnitude of the applied bias. Consequently, the current density for diffusion theory resembles to TE except for exponential dependence of saturated current density J_D which is strongly affected by applied bias and barely dependent temperature [100].

3.3.1.3. Tunneling Phenomena

When a heavily doped semiconductor is considered, the charge transport is dominated by the quantum-mechanical tunneling current due to the narrow depletion width underneath semiconductor. The tunneling current from semiconductor to metal is a function tunneling probability and summation of both occupied and unoccupied probability for semiconductor and metal, respectively [100]. Therefore, the tunneling current can be written as,

$$J_{S \to M} = \frac{A^* T^2}{kT} \int_{E_{Fm}}^{q\varphi_b} F_S \, T(E)(1 - F_m) dE \tag{3.24}$$

where F_S and F_m is the Fermi-Dirac distribution functions for the semiconductor and metal. *T(E)* is the tunneling probability depending on the width of barrier. Additionally, similar relation can be written for the current density $J_{M \to S}$ from the metal to semiconductor. Therefore, net current density is the summation of the both two components.

$$T(E) \sim \exp\left(-(q\varphi_{eff})/E_{00}\right) \tag{3.25}$$

$$E_{00} = \frac{qh}{2\pi} \sqrt{\left(\frac{N_D}{\varepsilon_S m^*}\right)} \tag{3.26}$$

then tunneling current density

$$J \sim \exp\left(-(q\varphi_{eff})/E_{00}\right) \tag{3.27}$$

It is clear that tunneling current density increases with increasing donor concentration.

3.3.2. Reverse Bias Transport Mechanism

3.3.2.1. Thermionic Field Emission Model

Thermionic field emission takes place under reverse bias which is strongly influenced and consists of tunneling of charge carrier at the Fermi level and thermally excited carriers for which tunneling barrier is narrow. Under reverse bias, electrons are removed metal surface which generates positive image charge in metal. Thus, an attractive coulomb force is produced by the positive image charge due to the removed electrons come back into metal which leads to decrease the effective barrier height. This reduced barrier height can be expressed as

$$\Delta\varphi = \sqrt{\frac{q\varepsilon_{max}}{4\pi\epsilon_0\epsilon_s}} \tag{3.28}$$

it should be noted that reduced barrier height is proportional to applied voltage that gives rise to field relevance for the reverse bias current. The electric field on the reverse bias current can be calculated by using φ_{b0} - $\Delta\varphi$ instead of φ_{b0} in thermionic emission relation

$$J = AA^{*}T^{2}exp\left[-\frac{q(\varphi_{b0}-\sqrt{q\varepsilon_{max}/4\pi\epsilon_0\epsilon_s})}{kT}\right] \tag{3.29}$$

3.3.2.2. Poole-Frenkel Emission Model

Poole-Frenkel (P-F) emission takes place under strong electric field that reduces energy barrier. This reduction of barrier is related to interactions between image force and the applied electric field for Schottky effect. However, for P-F charge transport, interaction has to do with both ionized trap and applied electric field. Figure 3.5 illustrates P-F conduction mechanism involving potential well owing to the trap states.

Under applied electric field, potential well is bended to reach equilibrium that decreases barrier to facilitate removed carriers from one trap states to lower one. The potential energy of trapped electron can be given as

$$\varphi(x) = -q^2/(4\pi\epsilon_0\ \epsilon_s\ x) \tag{3.30}$$

where x is distance away from the trap center. Finally, P-F emission can be written as[104]

$$J = \sigma_0 \varepsilon exp\left[\frac{-q(\varphi_T - \sqrt{q\varepsilon/\pi\epsilon_0\epsilon_S)}}{kT}\right] \tag{3.31}$$

where $\sigma_0 = N_C q\mu$ is the low field electric conductivity, N_C is the density of states of conduction band and $q\varphi_T$ is the trap energy level. If the plot of ln(J/E) as a function of $E^{1/2}$ is linear behavior, the trap barrier height are determined from intercept at E = 0.

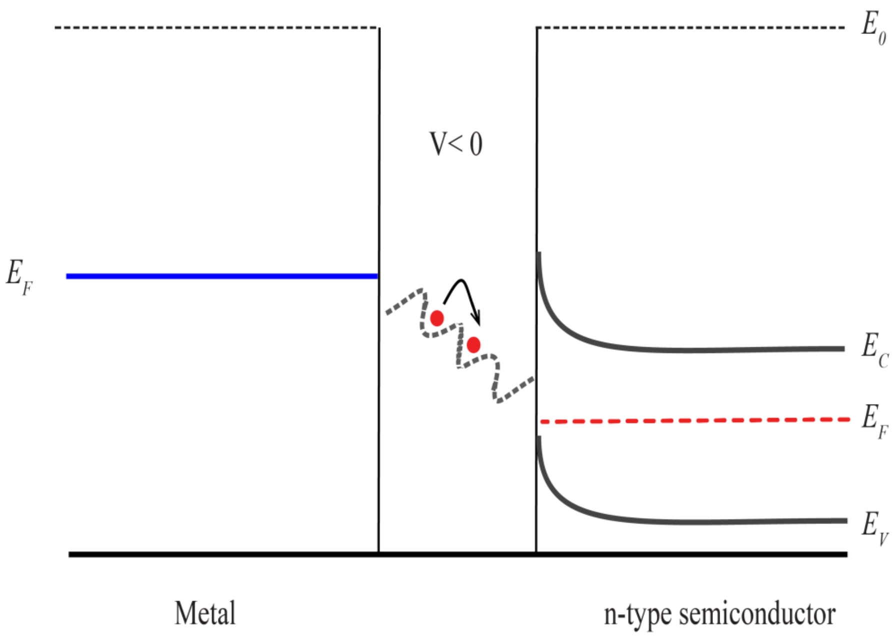

Figure 3.5. P-F transport mechanism under electric field.

3.4. Measurement of Schottky Barrier Height

Current-voltage *(I-V)* measurement plays important role in determining major Schottky parameters such as n, SBH and R_s respectively. Net current at the metal-semiconductor interface can be given as [100]

$$I = AA^{*}T^{2} \exp\left(-\frac{q\phi_B}{kT}\right)\left[exp\left(\frac{qV}{nkT}\right) - 1\right] \tag{3.32}$$

where A is the effective contact area, A^{*} is the Richardson constant (*~112 A cm^{-2} K^{-2} for n-Si*), T is the absolute temperature, ϕ_B is the barrier height, k is the Boltzmann constant, q is the elementary charge and n is the ideality factor. Due to the value ideality factor is obtained as higher than unity, the effect of R_s should be included and relation can be rewritten as

$$I = \ AA^{*}T^{2} \exp\left(-\frac{q\phi_B}{kT}\right) \exp\left(\frac{q(V-IR_S)}{nkT}\right) \text{ for } q(V - IR_s) > \ kT \tag{3.33}$$

if the equation 3.33 is rearranged,

$$V = n\frac{kT}{q}\ln\left(\frac{I_0}{AA^{*}T^{2}}\right) + IR_s + n\phi_B \tag{3.34}$$

when the equation 3.34 is differentiated with respect to I,

$$\frac{dV}{dln(I)} = n\frac{kT}{q} + IR_s \tag{3.35}$$

then n can be expressed as an inversely slope of *ln (I)* vs *V*,

$$n = \frac{q}{kT}\frac{dV}{dln(I)} \qquad (3.36)$$

It should be pointed out that *n* is a measure of a ideal Schottky diode with solely thermionic emission process and the value of *n* equals to 1. However, the value of *n* can be larger than 1. The variation of *n* is also associated with additional interface states between metal-semiconductor, different device fabrication and data derivation in the fitting procedure. The R_s can be defined as the combination of contact resistance between metal and semiconductor, resistivity of metal and semiconductor and resistance of connecting wires [33]. Additionally, The R_s gives important information about interface properties between metal and semiconductor. Values of R_s are determined from the slope of the *dV/dln(I)* vs *I* plot (Figure 3.6). Furthermore, in order to determine SBH, function *H(I)* can be defined as

$$H(I) = V - n\frac{kT}{q}ln\left(\frac{I}{AA^{*}T^{2}}\right) = IR_S + n\phi_B \qquad (3.37)$$

the SBH can be obtained from the intercept of the linear region of *H(I)* vs *I* plot (Figure 3.6). Moreover, SBH plays a crucial role in terms of semiconductor device technology. For instance, when the barrier height is relatively small, leakage current or dark current of device increases due to thermionic emission room temperature. However, if the barrier height is high, device display low leakage at higher temperature and high forward drop.

Another way to calculate the value of SBH is the Arrhenius plot which can be written as

$$\ln\left(\frac{I_S}{T^2}\right) = \ln(A^{*}A) - \frac{q\phi_B}{kT} \qquad (3.38)$$

where I_s is the saturation current. By plotting $\ln(I_S/T^2)$ vs the function of a temperature (*1/T*), the SBH is determined from the slope of a linear region (Figure 3.7).

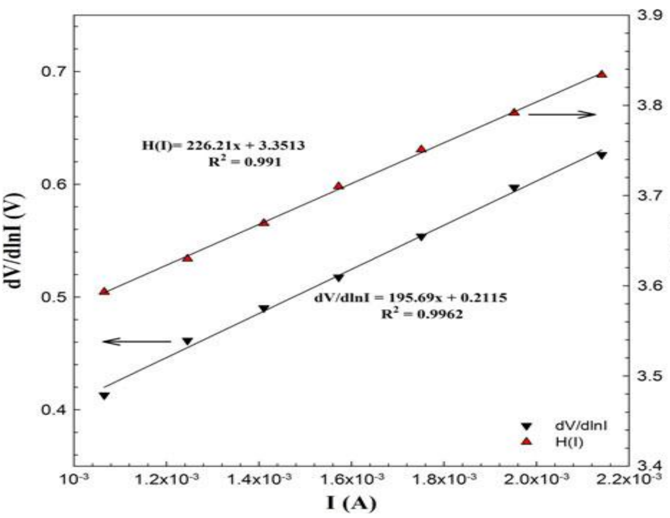

Figure 3.6. *dV/dln(I)* vs *I* and *H(I)* vs I plots of structure GaxIn1-xP/GaAs at room temperature[105].

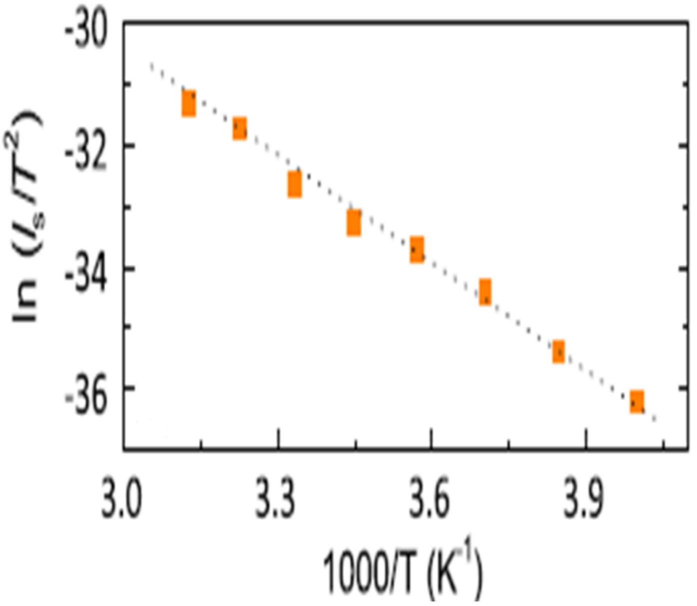

Figure 3.7. A typical Arrhenius plot for the graphene/GaAs diode [32].

3.5. Schottky Contact between Graphene and Semiconductor Interface

Contrary to metal-semiconductor interface, where the Fermi level of metal remains constant due to the high density of states, even small variation in charge carrier density can significantly manipulate the Fermi level of graphene. Accordingly, thermionic emission model was modified by S. Tongay in order to consider the alteration of the Fermi level due to the applied bias voltage [37].

Figure 3.9 indicates energy band diagram of graphene under thermal equilibrium, forward and reverse bias condition, respectively. Under forward bias, the Fermi level of graphene E_F is decreased. However, for reverse bias E_F of graphene is increased due to amounts of induced electrons in graphene. When bias dependence embedded in to diode equation, total barrier height can be given as

$$e\varphi_b = e\varphi_b^0 + e\Delta\varphi_b(V) = e\varphi_b^0 - \Delta E_F(V) \tag{3.39}$$

where φ_b^0 is the Schottky barrier height at zero bias and $\Delta\varphi_b(V)$ is the barrier height at constant voltage V. Then, graphene's the Fermi energy can be written as [60]

$$\Delta E_F = \pm \frac{h}{2\pi} v_F \sqrt{|n_{induced}(V)|} \tag{3.40}$$

where $n_{induced}$ is the charge induced by the application of a bias V. Then total charge density can be obtained to multiply by n_0 and $n_{induced}$. Therefore, the bias dependent of SBH can be obtained as

$$\varphi_b(V) = \varphi_b^0 - \frac{\Delta E_F(V)}{e} = \varphi_b^0 - a\left(\sqrt{V_{bi} - V - \frac{k_B T}{e}} - \sqrt{V_{bi} - \frac{k_B T}{e}}\right) \tag{3.41}$$

where $a = h/4\sqrt{\pi} v_F \sqrt{\epsilon_s N_D / 2en_0}$. It should be noted that when applied voltage is equals to zero, barrier height becomes $\varphi_b = \varphi_b^0$. Therefore, φ_b^0 can be calculated by forward bias current at zero bias. Tongay *et al*[37] showed that graphene forms the Schottky junction with rectification behavior when it is transferred onto most of the conventional semiconducting materials Si, GaAs, SiC and GaN (Figure 3.8). They also found that the Fermi level of graphene is variable during the charge transfer at the graphene/semiconductor interface. These variations took place under reverse bias voltages when the amounts of electrons induced in the graphene which leads to increase the Fermi level of graphene and leakage current. Additionally, the extracted SBH values on various graphene/semiconductor junctions are determined both current density – voltage (Arrhenius plot).

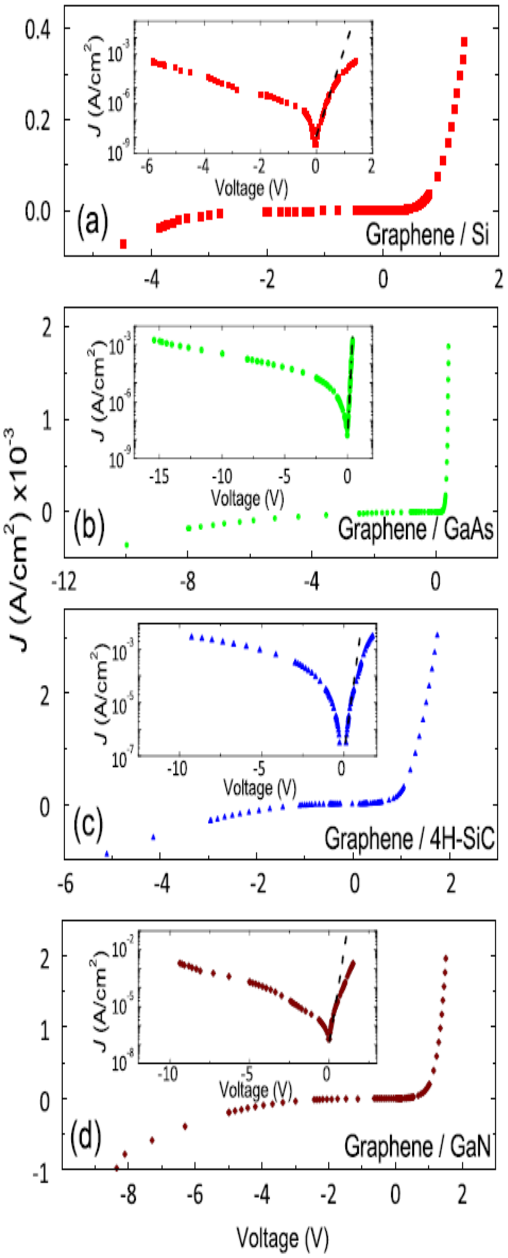

Figure 3.8. Current density - voltage characteristic of (a) graphene/GaAs, (b) graphene/4H-SiC, (c) graphene/Si and (d) graphene/GaN. Insets: log$J$ – V as a function of voltage [37].

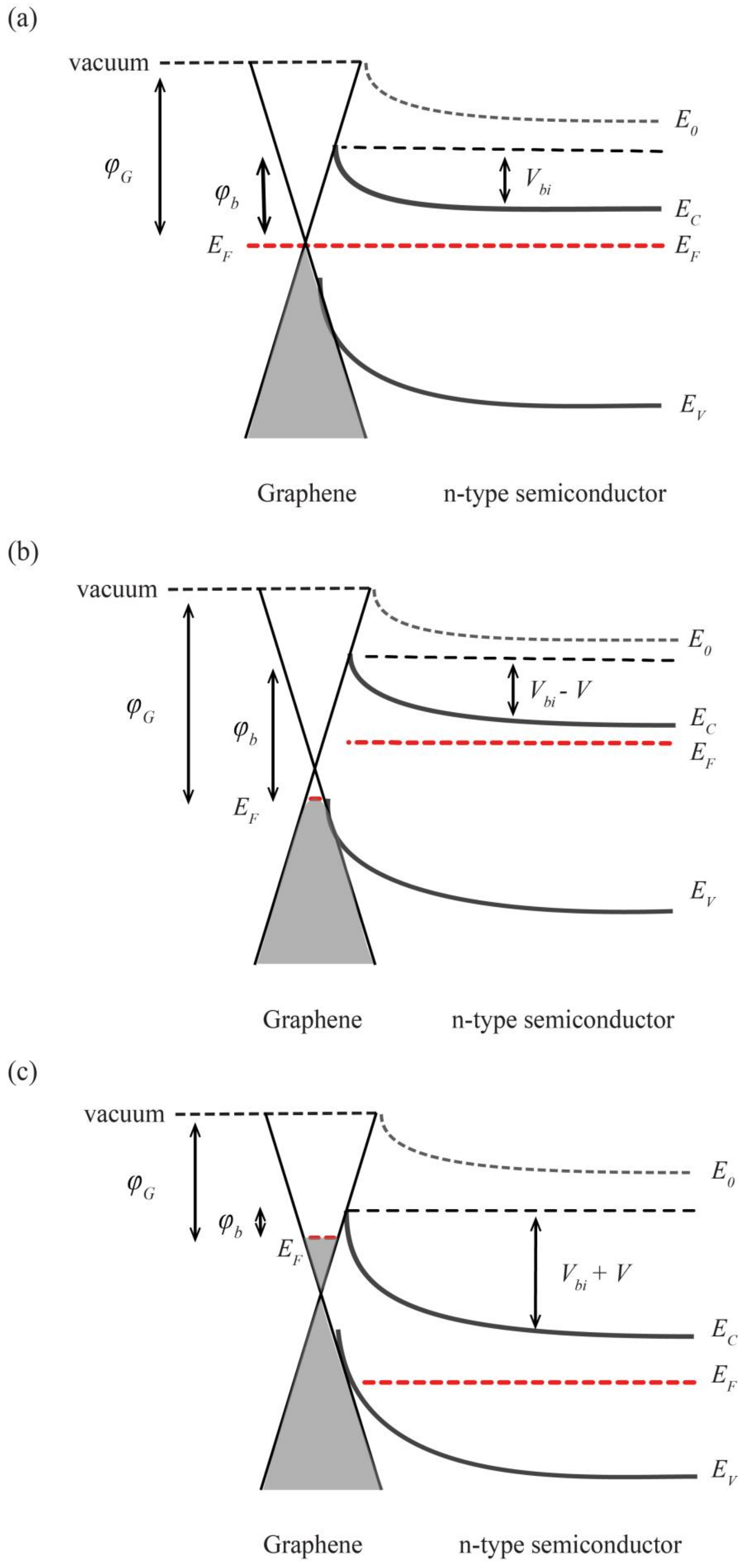

Figure 3.9. Energy band diagram of graphene (a) thermal equilibrium (b) forward bias and (c) reverse bias condition.

CHAPTER 4

EXPERIMENTAL TECHNIQUES

4.1. Preparation of SAMs Molecules and P3HT Polymer

In this work, two different sets of SAMs molecules were prepared to investigate their effect on graphene/Si Schottky devices (Figure 4.1 and Figure 4.2).

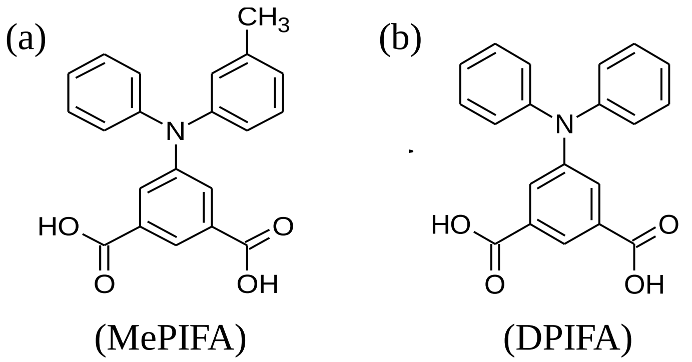

Figure 4.1. Chemical structures of 1st set of SAMs molecules, (a) MePIFA and (b) DPIFA.

SiO_2(300 nm)/n-Si substrates were first cleaned in an ultrasonic bath for 10 min. in deionized water, acetone, ethanol and 2-proponal, respectively. For MePIFA and DPIFA, SAMs with 1 mM concentration were prepared at room temperature in methanol while TPA and CAR SAMs with 1 mM concentration were evaluated at room temperature in dimethyl sulfoxide (DMSO). SiO_2(300 nm)/n-Si substrates were separately kept in methanol-SAMs and DMSO-SAMs solutions for 24 hours to be covered with SAMs. The substrates were then rinsed with methanol and DMSO separately to remove SAMs residues and dried in a stream of N_2 gas.

In order to fabricate P3HT-graphene/Si samples, a set of regioregular poly P3HT (Sigma Aldrich) solutions with 2.5, 5 and 10 mg/ml concentrations were prepared at room temperature in toluene (Figure 4.3). Then, the coating of graphene with P3HT molecules was done by dip-coating technique with an extraction speed of 5 mm/s.

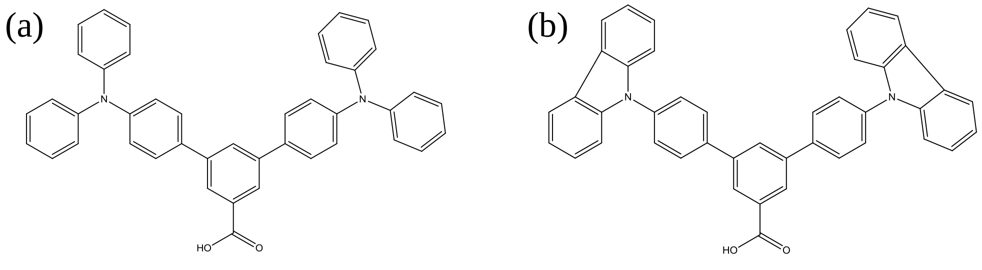

(TPA) (CAR)

Figure 4.2. Chemical structures of 2nd set of SAMs molecules, (a) TPA and (b) CAR.

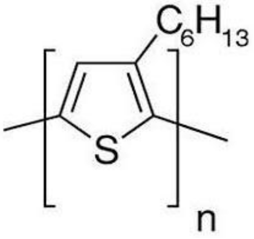

Figure 4.3. Chemical structure of P3HT.

4.2. Growth of Graphene by CVD Method

Cu foil (*25 µm thick, 99.8 % purity, Alfa Aesar*) as catalyst-substrate material was placed on a quartz plate and inserted to a tube furnace (Lindberg/Blue TF55035C Split Mini Tube) of atmospheric pressure CVD system (Figure 4.4). As for the first step, the Cu foil was heated up to 1073 ^{o}C under as H_2 (20 sccm) + Ar (1000 sccm) gas mixture with a temperature ramp rate of 30 ^{o}C min^{-1}. Then the foil was annealed under the same temperature and flows rates for 1h. After the annealing process, CH_4 (10 sccm) was introduced into the tube furnace for 1 min. in order to facilitate the graphene growth. Finally, the sample was left for rapid cooling from growth temperature to room temperature under gas flows of H_2 (20 sccm) and Ar (1000 sccm). Graphene growth chart including heating, annealing, growing and cooling process is given in Figure 4.5.

Additionally, optimized graphene growth parameters are summarized in Table 4.1

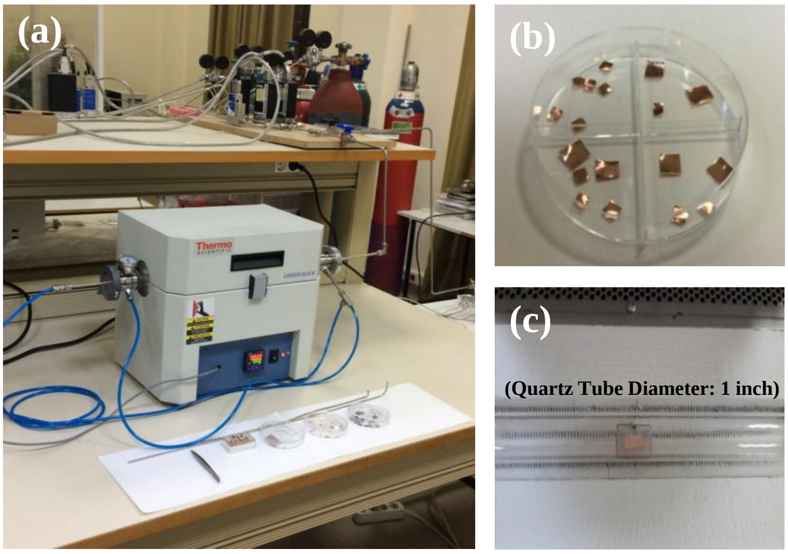

Figure 4.4. (a) The CVD graphene growth set-up including tube furnace, quartz tube and mass flow meters. (b) Deiced Cu foil with a size of 3 mm x 5 mm. (c) Inserted Cu foil on quartz plate to the quartz tube with a diameter of 1 inch.

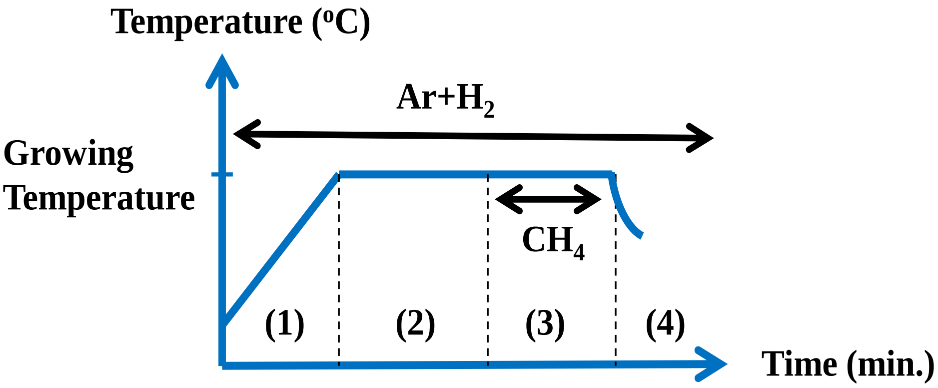

Figure 4.5. (1) Heating, (2) annealing, (3) growth and (4) cooling stages of graphene growth process on Cu foil with schematic representations by APCVD.

Table 4.1. Optimized graphene growth parameters on Cu foil by APCVD.

Sample	**Temperature (°C)**	**Ar (sccm)**	**H_2 (sccm)**	**CH_4 (sccm)**	**Ramp Time (min.)**	**Annealing Time (min.)**	**Growth Time (min.)**
Graphene	1073	1000	20	10	33	59	3

4.3. Transfer of Graphene on to SiO_2/n-Si Substrate

Figure 4.6 demonstrates the steps of the graphene transfer methods. Microposit S1318 Photoresist (PR) was utilized as supporting layer during the graphene transfer process. The PR on the graphene–Cu template was drop casted and annealed at 70 °C overnight. Iron chloride ($FeCl_3$) solution was used to etch the Cu foil and to suspend the graphene-PR. After the Cu foil was fully etched away, graphene-PR was rinsed with deionized water in order to remove any $FeCl_3$ residue. After the N_2 drying process, graphene-PR was transferred onto the surface of the clean SiO_2/n–Si substrate. The substrate was baked at a temperature of 110 °C in order to provide better adhesion of the graphene layer to the surface of the substrate. As for the last step, the PR was removed by hot acetone to leave the graphene layer on its own on the SiO_2/n–Si substrate.

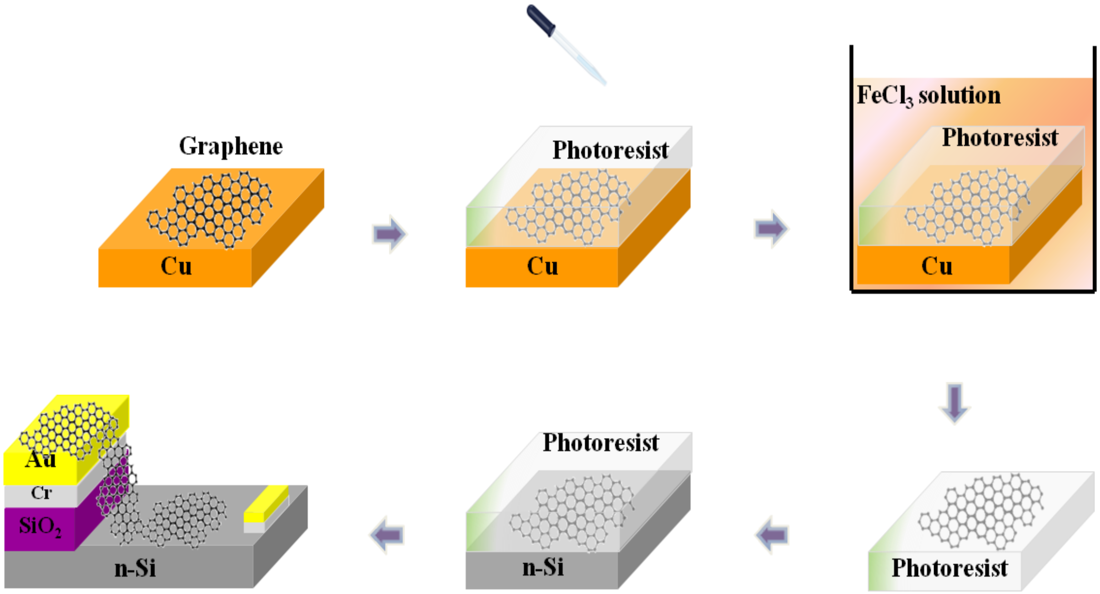

Figure 4.6. Schematic illustration of the graphene transfer process. (a) CVD grown graphene on Cu. (b) Photoresist was drop casted onto graphene/Cu substrate. (c) Then, photoresist/graphene substrate was immersed in $FeCl_3$ solution. (d) After Cu was completely etched, photoresist/graphene was transferred onto fabricated device structure (e-f).

4.4. Fabrication of Graphene/Silicon Schottky Devices

We used commercial SiO_2 (300 nm)/n-Si wafers with a resistivity of ρ = 1-10 Ω.cm. The wafer was diced into 10 mm x 10 mm substrates and was ultrasonically cleaned for 10 min. in deionized water, acetone, ethanol and 2-proponal, respectively. Thereafter, a part of SiO_2 was etched using a mixture of H_2O:HNO_3:HF (60:1:1.5) in order to prevent electrical shortening along the graphene layer. Then, graphene was transferred on to the surface of partially etched SiO_2/n-Si substrate.

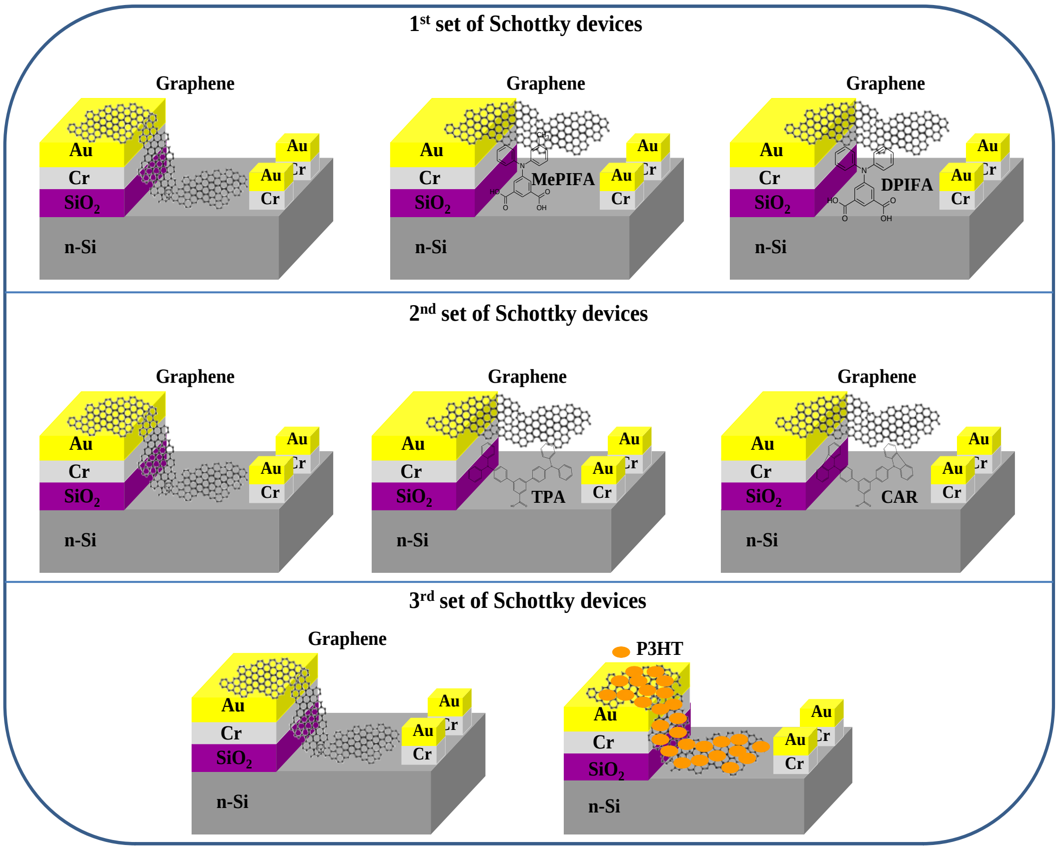

Figure 4.7. The schematic of device structures of graphene/Si Schottky diodes.

The interconnect electrodes comprising 5 nm Cr and 85 nm Au layers were deposited on SiO_2 and n-Si to get ohmic contact using thermal evaporation technique. The fabricated devices were separately kept in methanol-SAMs and DMSO-SAMs solutions for 24 hours to be covered with the corresponding molecules. The devices were then rinsed with methanol and DMSO separately to remove the SAMs residues and dried in a stream of N_2 gas. Additionally, a set of regioregular P3HT solutions with 2.5, 5 and 10 mg/ml concentrations were prepared at room temperature in toluene. Then, the coating of graphene with P3HT molecules was done by dip-coating technique with an extraction speed of 5 mm/s. Finally, P3HT-graphene/Si samples were dried at 110 ^{o}C for 10 min. in air. The schematic of all the fabricated Schottky devices are shown in Figure 4.7.

4.5. Characterization Techniques

4.5.1. Scanning Electron Microscopy

Scanning electron microscopy (SEM) was invented by Max Knoll in 1935 as a surface characterization technique. The working principle of SEM is based on focused electron beam-matter interaction. When the electron hits the sample surface, the interaction between electron and sample leads to various signals being emitted such as cathodoluminescence, auger electrons, characteristic x-ray, secondary electrons and back-scattered electrons.

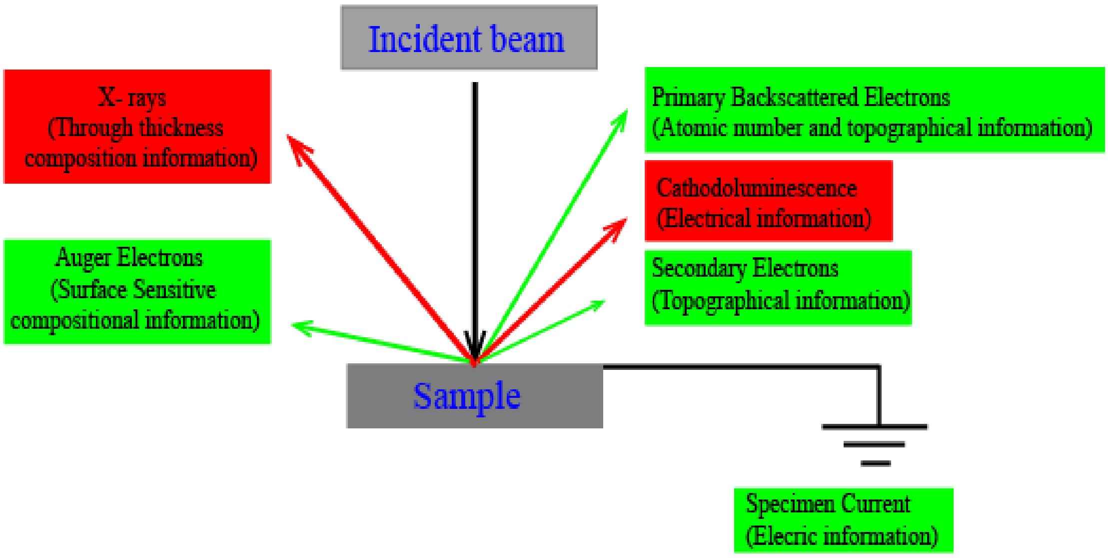

Figure 4. 8. Electron-sample interactions.

Electron-sample interaction can provide information on composition, surface sensitive compositional, atomic number, topographical and electrical, respectively. SEM involves an electron gun producing electron beam. The electron beam goes through a vertical way from electron gun to the sample surface in a vacuum. The vertical direction contains the deflection coils and lenses focusing the beam onto the sample. Electrons and x-rays are produced from the sample when the electron beam strikes the sample. Backscattered and secondary electron detectors collect these ejected electrons and x-rays and convert them into a signal. As a result, the final image is obtained.

In our study, secondary electron detector was used to investigate the surface morphology of graphene and fabricated graphene/Si Schottky devices (Figure 4.9).

Figure 4.9. SEM set up in Materials Research Center at IZTECH.

4.5.2. AFM and KPFM Measurements Technique

Atomic Force Microscope (AFM) was invented by Binnig, Quate, and Gerber in 1985 as a tool for characterizing surface [106]. AFM is based on the analysis of long range Van der Waals forces and repulsive forces. The AFM operates by permitting extremely sharp tip, which is integrated into end of the cantilevers, moving above the surface under the interactive atomic forces. Thus, the information about the sample surface is obtained with a spatial resolution of a few nanometers by measuring deflection and torsion of the cantilever.

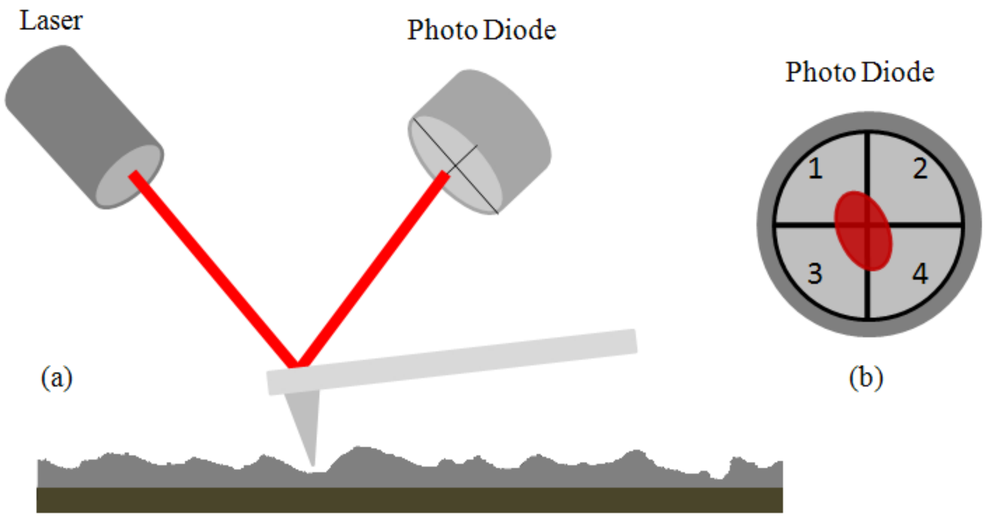

Figure 4.10. (a) Schematic description of optical detection system, (b) photodiode sections.

The fundamental idea of the AFM working principle is measurements of interactive force between tip and sample surface. The interactive forces can be explained by considering the van der Walls forces [107]. Van der Walls force is occurred by dipole or induce-dipole interactions at the atomic and molecular level. The van der Walls energy of two atoms, located at a distance r from each other, is approximated by the exponential function-Lennard potential (Figure 4.11):

$$U(r) = U_0 \left\{ -2\left(\frac{r_0}{r}\right)^6 + \left(\frac{r_0}{r}\right)^{12} \right\} \tag{4.1}$$

The first term in the sum describing the attraction of long distances caused by a dipole-dipole interaction and second term considers short range repulsion owing to the Pauli Exclusion Principle. The parameter r_o is the equilibrium distances between atoms, the energy value in the minimum.

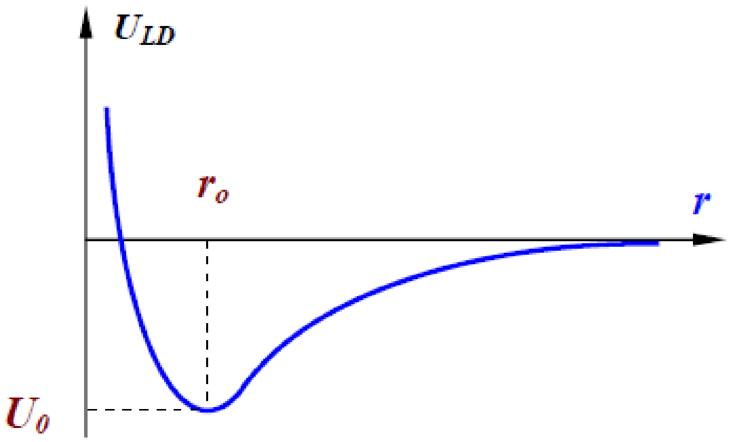

Figure 4.11. Lennard-Jones potential [108].

AFM surface characterization was performed in semi-contact (tapping) mode operation using commercial Scanning Probe Microscopy instrument (Solver Pro 7 from MNT-MDT, Russia). Our experimental setup is shown in Figure 4.12. The AFM system was placed on a vibration isolation table to prevent the mechanical vibrations from the environmental noise. Optical camera integrated into the system sends the image to the computer screen and helps to define the tip position on the sample. Also, the laser source and photodiode are the optical detection system in the AFM can be seen in Figure 4.12. During all the scans, a golden silicon tip with a curvature of 10 nm was used. Surface topography measurements were performed on graphene on SiO_2/Si.

Kelvin Probe Force Microscopy (KPFM) are frequently used to measure surface potential difference (SPD) between conductive tip and the sample surface, thus giving information on the work function of conductive thin films [109]. The SPD (V_{SPD}) between tip and sample is defined as following [110],

$$V_{SPD} = \frac{\varphi_{sample} - \varphi_{tip}}{e} \tag{4.2}$$

where e is the electric charge, φ_{sample} and φ_{tip} are the work functions of the sample, and AFM conductive tip respectively. For KPFM measurements, during the operation, a constant voltage U_0 and a variable voltage $U_{\sim}=U_1 sin(\omega t)$ are applied to the substrate as given in Figure 4.12. When $\varphi(x, y)$ is the potential distribution on the sample, the voltage between the AFM tip and surface will be

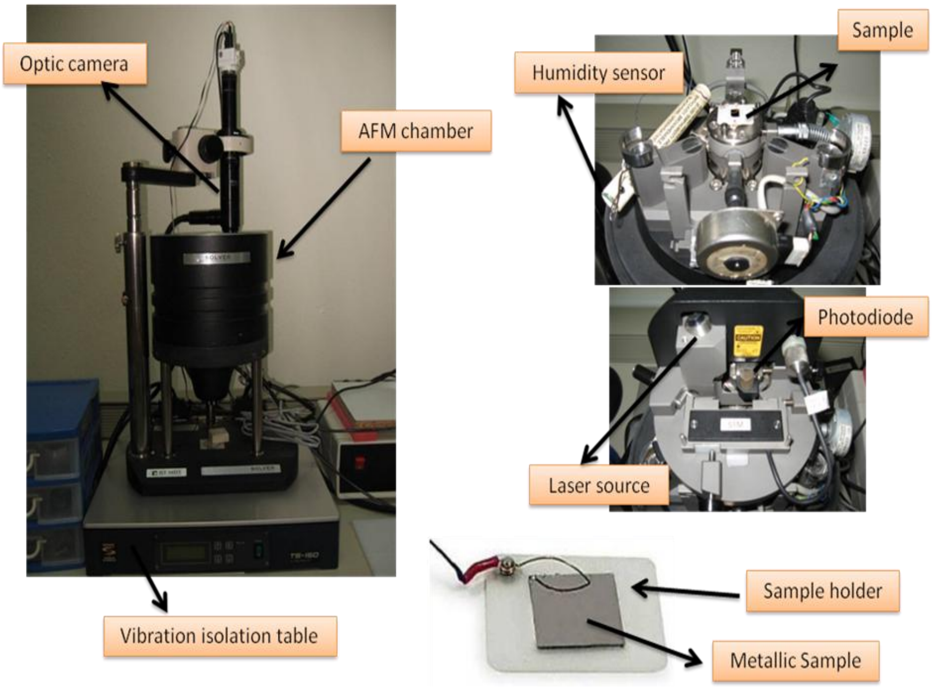

Figure 4.12. AFM set up in Quanum Device Laboratory at IZTECH.

$$U = U_0 + U_1 \sin(\omega t) - \varphi(x, y) \tag{4.3}$$

and stored energy in this system will be

$$E = \frac{CU^2}{2} \tag{4.4}$$

then electric force tip-sample interactions is

$$\vec{F} = -grad(E) \tag{4.5}$$

Z-component of the electric force between tip and surface is written as

$$F_Z = -\frac{\partial E}{\partial z} = -\frac{1}{2}U^2\frac{\partial C}{\partial z} = -\frac{1}{2}\left[U_0 - \quad (x,y) + U_1\sin(\omega t)\right]^2\frac{\partial C}{\partial z} \tag{4.6}$$

by using identity of $\sin^2(\omega t) = [1-\cos(2\omega t)]/2$, electric force between tip and sample becomes,

$$F_Z = -\frac{1}{2}\left\{[U_0 - \varphi(x,y)]^2 + 2[U_0 - \quad (x,y)]U_1\sin(\omega t) + \frac{1}{2}{U_1}^2\left[1-\cos(2\omega t)\right]\right\}\frac{\partial C}{\partial z} \tag{4.7}$$

this equation can be divided into three parts and detection of cantilever oscillation amplitude at a *ω* frequency allows to obtaining surface potential properties of sample as the following,

$$F_{z(\omega)} = -\left\{[U - \varphi(x,y)]\,U_1\sin(\omega t)\right\}\frac{\partial C}{\partial z} \quad \text{component at frequency } \omega; \tag{4.8}$$

The work function of the samples can be calculated using following equation[17]

$$\varphi_{sample} = 4.6\ eV + SPD_{sample} - SPD_{HOPG} \tag{4.9}$$

where φ_{sample} is the work fuction of the sample, SPD_{sample} is the surface potential difference between sample and tip and SPD_{HOPG} is the surface potential difference between HOPG and tip, respectively. For KPFM measurements, conductive AFM tip should be used to generate electrical force between tip and sample. In this work, TiN coated conducting AFM tip with a curvature of 35nm was used and calibrated with HOPG (φ_{HOPG} = 4.6 eV) as reference [111]. To apply voltage between AFM tip and sample surface, a special sample holder with contact electrode was used as shown in Figure 4.12. Detection of cantilever oscillation amplitude (Mag) at *ω* frequency goes to zero with the feedback loop by changing the applied dc (U_0) voltage. At this zero interaction-amplitude, applied dc voltage to the tip equals to the measured SP of the samples. As a result, contact potential differences between AFM tip and each of the samples were found from the Mag at ω frequency versus applied bias voltage as shown in Figure 4.14.

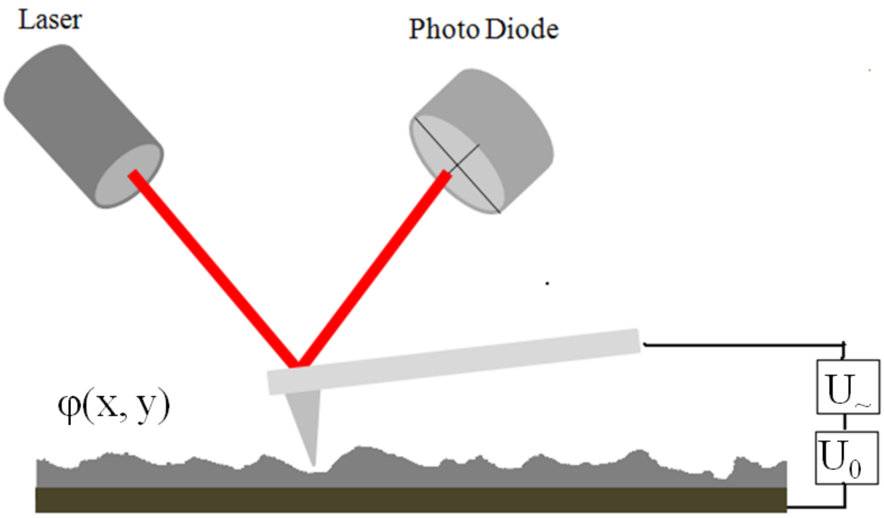

Figure 4.13. Measurement circuit of the electric tip-sample interactions.

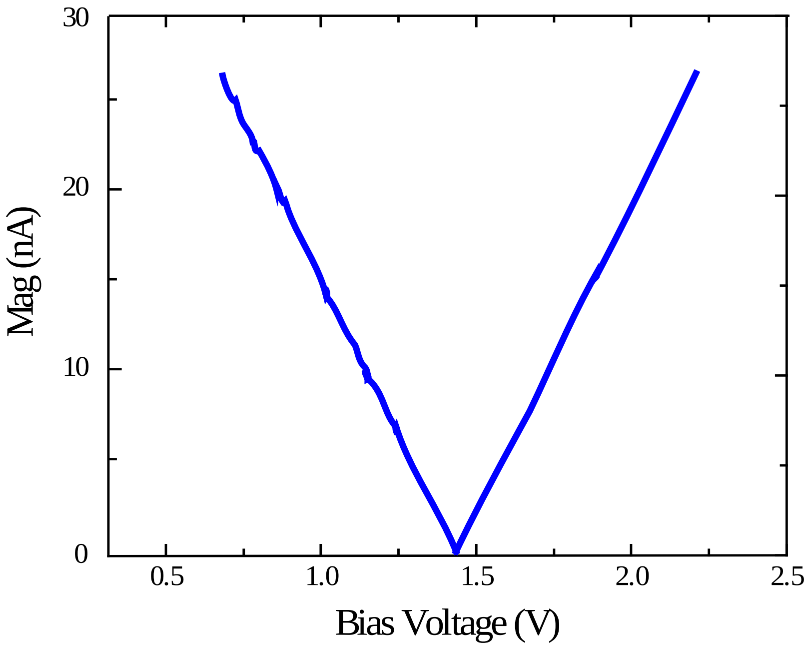

Figure 4.14. Typical cantilever oscillation amplitude as a function of bias voltage.

4.5.3. Raman Spectroscopy Measurement Technique

Raman Spectroscopy has been widely used to identify the number of graphene layers, continuity and quality of graphene. The working principle of Raman Spectroscopy is based on light-matter interactions. Photon of laser is absorbed by the sample and the scattered. The frequency of scattered photon is shifted up or down with respect to the incident photon frequency in the vibrational state. When the scattered photon has less or higher energy than the incident photon, this is called Stokes or Anti-stokes scattering. When the scattered photon has the same frequency with the incident photon, this is called Rayleigh scattering. Main scattering mechanism is Rayleigh. However, this does not provide any information. These scattering process are given in Figure 4.15.

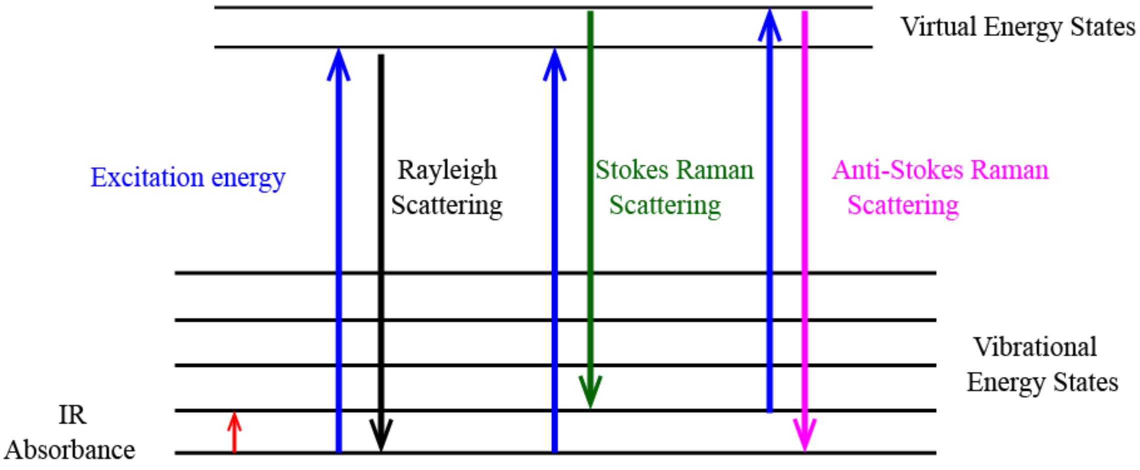

Figure 4.15. Raman scattering process.

Typically, Raman spectrum of graphene consists of three main peaks including, D, G and G' or 2D peaks (Figure 4.16). The D peak is observed at about 1350 cm^{-1} [112] and provide information about disorder (defect) content of graphene. The G is the main peak of graphene and related in plane C-C bond stretching of sp^2 carbon which is associated with phonons at Γ-point in the center first Brillion zone. It appears around 1585 cm^{-1} [112]. The 2D band is the strongest second-order graphene peak [113] (2700 cm^{-1}) and belongs to in plane mode of carbon rings.

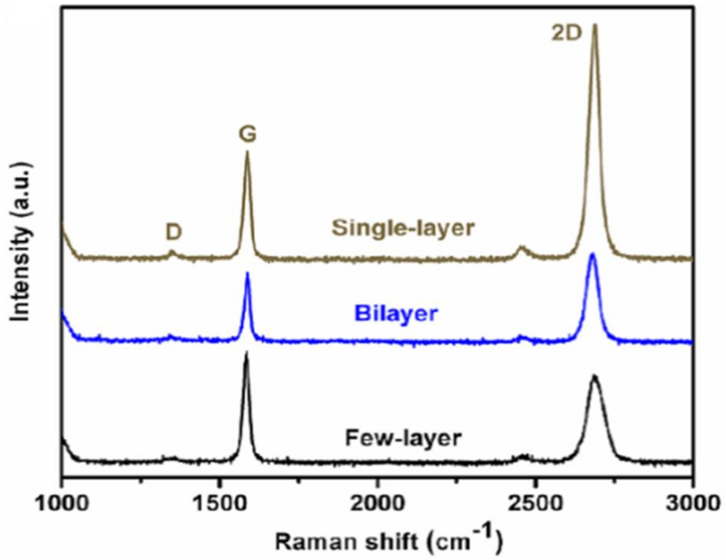

Figure 4.16. Raman spectra of single layer, bilayer and few layer graphene [114].

As addressed in section 2.4, iLO and iTO, which have dispersive energies at *Γ* and *K*-points, contribute to monitor main Raman bands in graphene. For G band in graphene, two vibration modes are observed in iLO and iTO at *Γ* and *K*-points (Figure 4.17 (a)). This process occurs, when the incident photon creates electron-hole pair which is scattered either iLO or iTO phonons in the vibration states. This process results in a radiative recombination and photon emission [115]. D and 2D band in graphene is stretched for iTO and *K* (or *K′*) points in the first Brillion zone (Figure 4.17 (b)). This process can be double or triple resonance in the electronic levels. While incident photon creates electron-hole pair that shows inelastic scattering by iTO at *K′*-points for double resonance. Both carriers are scattered by iTO from *K* to *K′*-points resulting in recombination and photon emission in triple resonance.

Furthermore, normalized intensity ratio (I_D/I_G) of graphene is used to measure the amount of defect. Therefore, higher (I_D/I_G) ratio gives idea about how defective graphene layer. For single layer graphene, the peak intensity ratio (I_D/I_G) ranges between 0.05 and 0.3 [116]. Intensity ratio I_G/I_{2D} gives the number of layers. While I_G/I_{2D} is less than 0.5 for single layer, this ratio equals to or higher 1 for bilayer and few layers graphene.

In this study, the Raman spectrum of our samples were acquired with Horiba (XploRA) Raman system using 532 nm laser excitation with 600 groove/mm grating under 100X microscope objective (Figure 4.18).

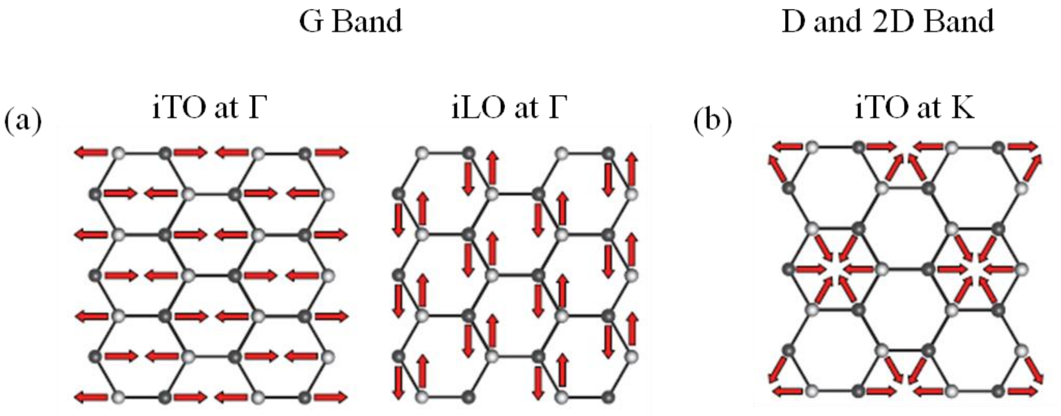

Figure 4.17. (a) G band streching modes for the iTO and iLO phonons at *Γ*-point. (b) D band streching mode for iTO phonons at *K*-point [115].

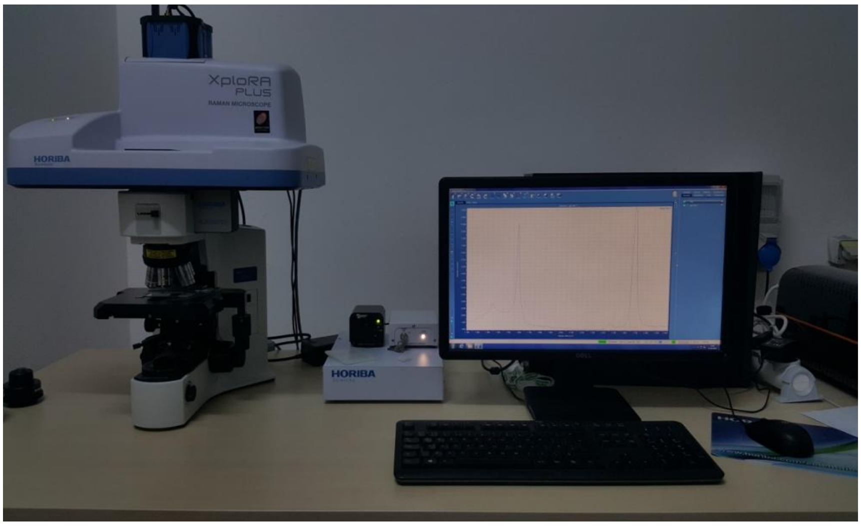

Figure 4.18. Raman spectroscopy measurement set up at IZTECH.

4.5.4. Electronic and Optoelectronic Measurements Set-up

In order to perform optoelectronic characterizations of graphene/n-Si photodiode, tungsten halogen lamp (Osram, 275 W) was used to generate light and specific wavelengths were separated with helping of monochromator (Newport, Oriel Cornerstone) including internal shutter. Before the measurement, flame spectrometer (Oceans Optics) was used to calibrate full width half maximum (FWHM) of light by changing spectrometer slit and power output of Si Photodiode FDS10X10 (Thorlabs) was obtained to define power of light on device area. Then time-resolved dark current and photocurrent measurement, and responsivity vs wavelength (resolution ~ 15 nm) were employed using Keithley 2400 source-meter as the voltage source and Keithley 6485 electrometer to detect dark current and photocurrent.

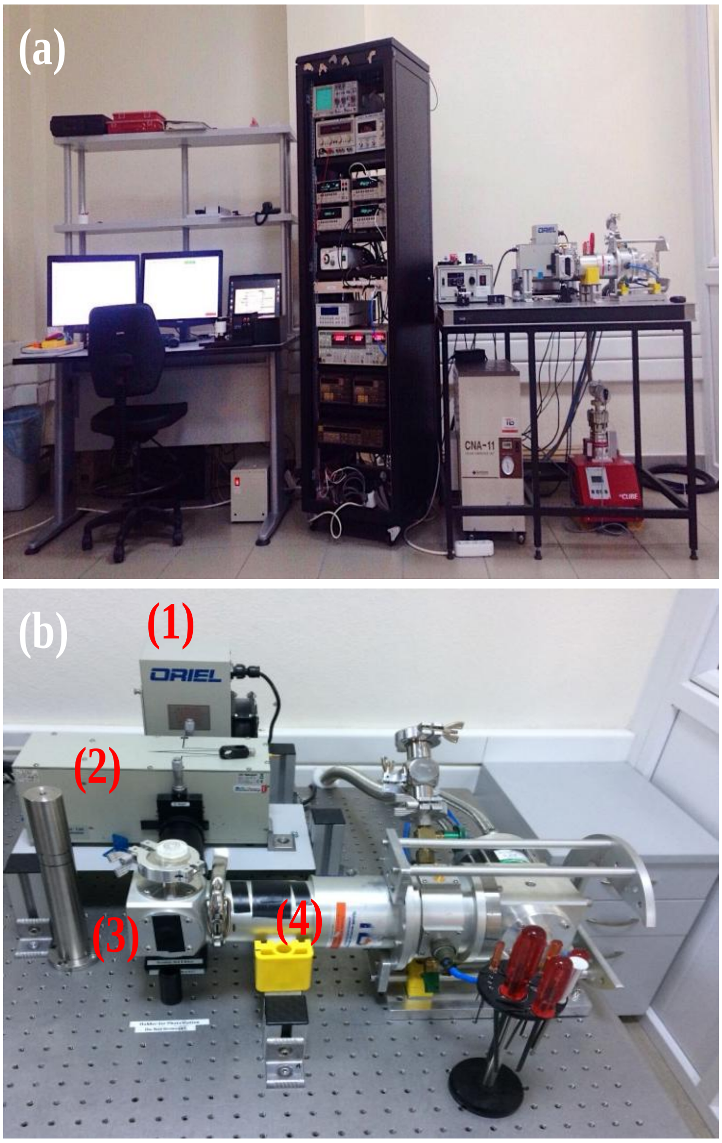

Figure 4.19. (a) Electronic and optoelectronic characterization units in Quantum Device Laboratory at IZTECH. (b) The photocurrent spectroscopy setup; (1) tungsten hologen lamp, (2) monochromator, (3) sample holder, (4) Cryostat system.

CHAPTER 5

RESULTS AND DISCUSSION

5.1. The Effect of Carboxylic Acid with Double Bond Aromatic SAM Molecules on the Device Characteristic of Graphene/Si Schottky Diodes

5.1.1. The Characterizations of Graphene Electrode

Figure 5.1 (a) shows the SEM image of graphene transferred on SiO_2/Si substrate. Some wrinkle was observed owing to the difference thermal expansion coefficient between Cu surface and graphene film during the cooling process. Raman spectrum indicates typical appearance of transferred graphene on SiO_2/Si including D band (1369 cm^{-1}), G (1587 cm^{-1}) and 2D band (2726 cm^{-1}), respectively (Figure 5.1 (a). The G band is the first Raman peak related to C-C stretching of sp^2 carbon. The 2D band is the second order graphene peak and the D provides information about the sp^3 bonds revealing "amount of disorder" in graphene. In addition to this, the intensity ratios of 2D/G and D/G have been utilized to identify number of graphene layers and defect content of graphene. $I_{2D/G}$ and $I_{D/G}$ were about 0.97 and 0.08 verifying presence of high quality bilayer graphene [117-119].

In order to understand modification of n-Si surface with DPIFA and MePIFA SAMs molecules, KPFM measurements were obtained using conductive AFM tip. The SPD between tip and sample can be defined in equation 4.1[120]. Figure 5.2 indicates Mag as a function of bias voltage. Bare n-Si, MePIFA/n-Si and DPIFA/n-Si were measured as 0.14, 0.19 and 0.38 V respectively. The differences of surface potential revealed the modification of n-Si surface with MePIFA and DPIFA SAMs molecular films. Increasing surface potential was related to enhanced charge density on the n-Si surface. In presence of the SAM molecules, potential distributions were enhanced compare to bare n-Si surface. As a result, surface potentials of SAM modified n-Si surfaces were increased with respect to bare n-Si surface.

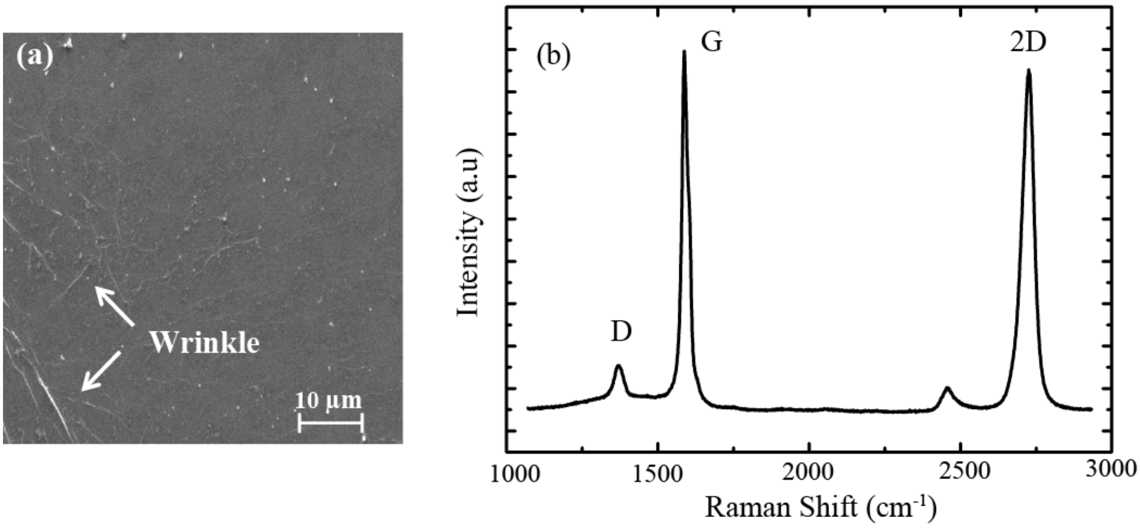

Figure 5.1. (a) SEM image of graphene on SiO_2/Si. (b) Raman spectrum of bilayer graphene transferred onto SiO_2/Si.

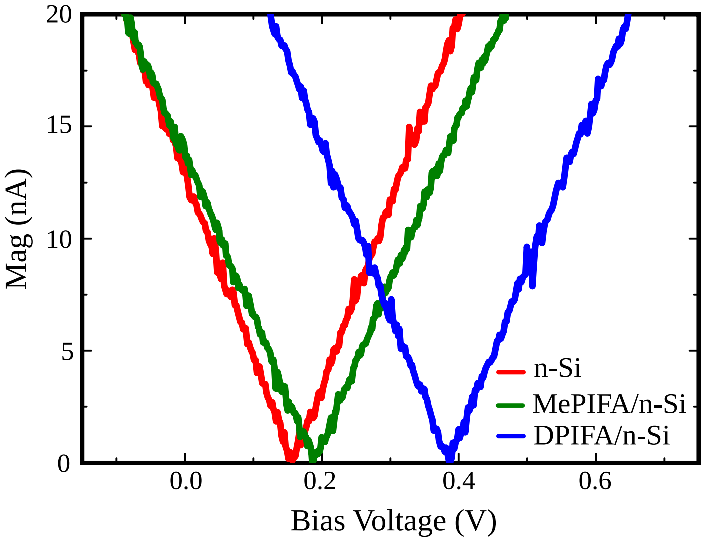

Figure 5.2. Contact potential differences of bare n-Si and modified n-Si with MePIFA and DPIFA SAMs.

Device structures of bare and modified graphene/n-Si and bonding mechanism between double bond carboxylic acid based SAMs and n-Si with native oxide are illustrated in Figure 5.3 (a-c). Due to formation of ester bond on the surface, charge injection and transport occurred through molecules and were enhanced owing to inelastic tunneling mechanism over its π-conjugated structure. Figure 5.3 (d-e) indicates energy band diagram of bare and SAMs based graphene/n-Si Schottky devices.

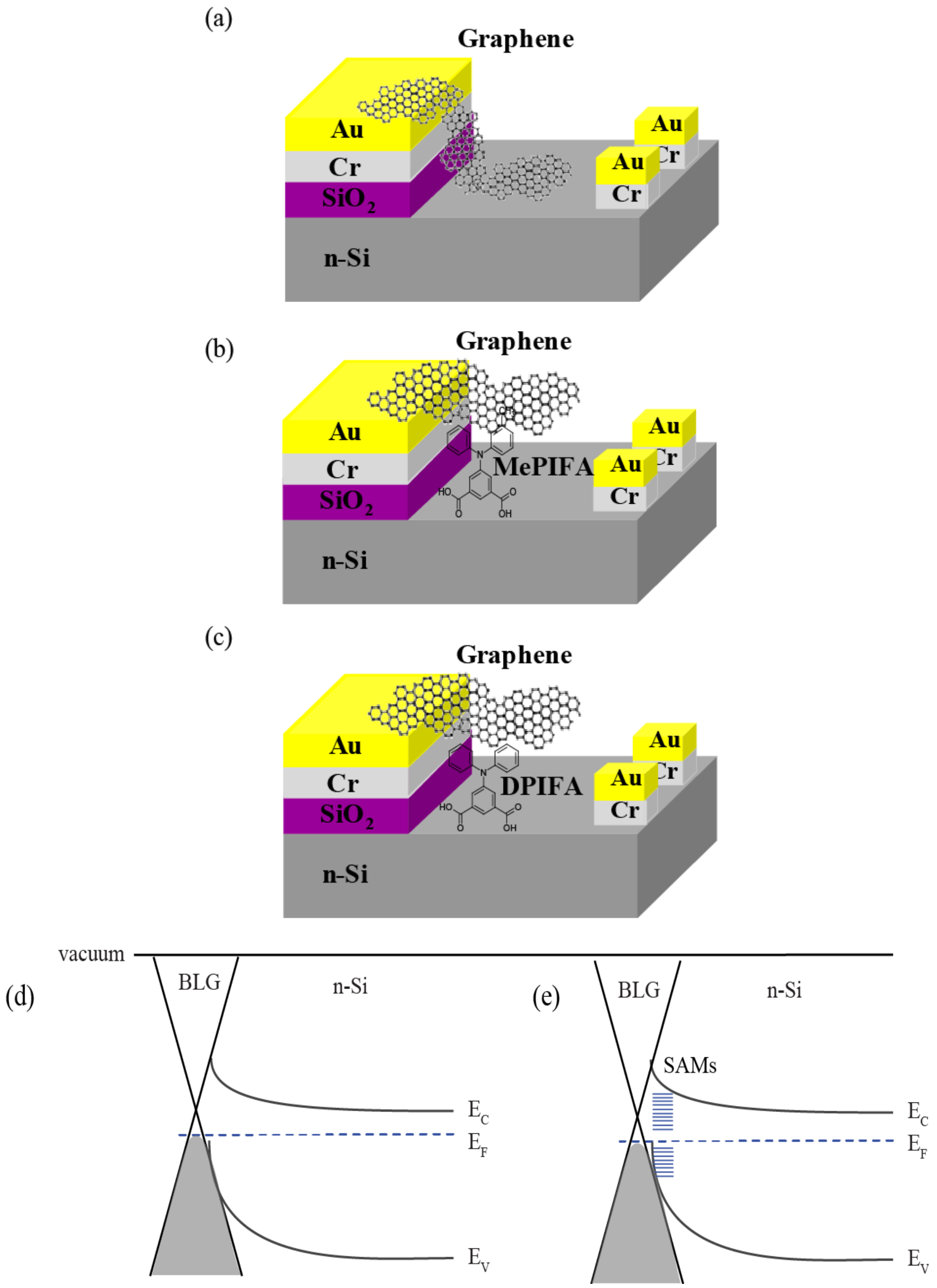

Figure 5.3. Device structures of (a) graphene/n-Si, (b) graphene/MePIFA/n-Si and(c) graphene/DPIFA/n-Si. Energy band diagram of (d) bare and (e) SAMs based graphene/n-Si Schottky diodes.

The work function differences between n-Si and graphene led to charge transfer from n-Si to graphene until alignment of Fermi level across the junction and as a result, bending of energy levels near junction took place (Figure 5.3 (d)). In the presence of

SAMs molecules, the molecular dipole layer created between n-Si and graphene and charge transfer were facilitated due to the reduction of energy barriers and π-bonding between aromatic SAMs molecules and graphene (Figure 5.3 (e)).

5.1.2. Electronic characterization of Graphene/Si Schottky Diodes

The electronic parameters of constructed three devices were showed rectifying behavior like metal/semiconductor Schottky contact. The current-voltage characteristics of graphene/n-Si, graphene/MePIFA/n-Si and graphene/DPIFA/n-Si diodes were shown in Figure 5.4. The diodes that modified by MePIFA and DPIFA SAM molecules were showed better rectifying behavior when compared to bare graphene based diode.

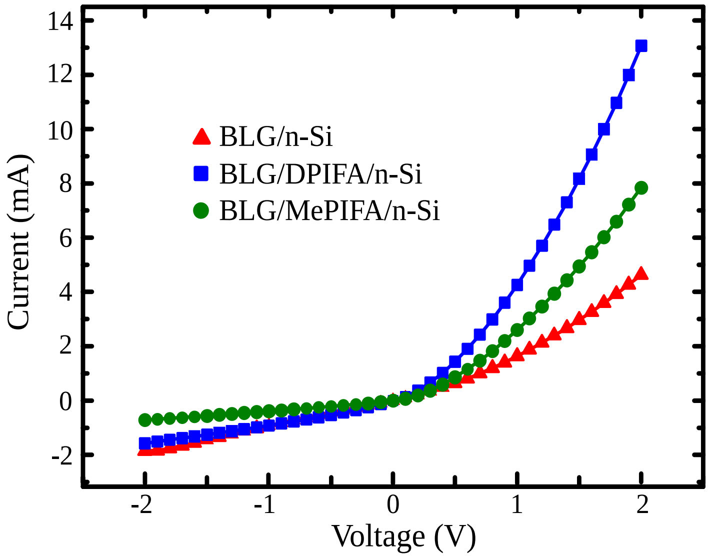

Figure 5.4. Current-voltage characteristics of the graphene/Si, graphene/MePIFA/n-Si and graphene/DPIFA/n-Si Schottky devices.

Current-voltage behavior can be analyzed by thermionic emission (equation 3.33) [100]. If the equation 3.33 is rearranged and differentiated with respect to I, n can be calculated using the equation 3.36. Additionally, function $H(I)$ is defined as the equation 3.37 and used to determine SBH of the devices. $dV/dln(I)$ vs. I and $H(I)$ vs.I plots for the diodes were shown in Figure 5.5 and the electrical parameters that were calculated from these plots are presented in (Table 5.1)

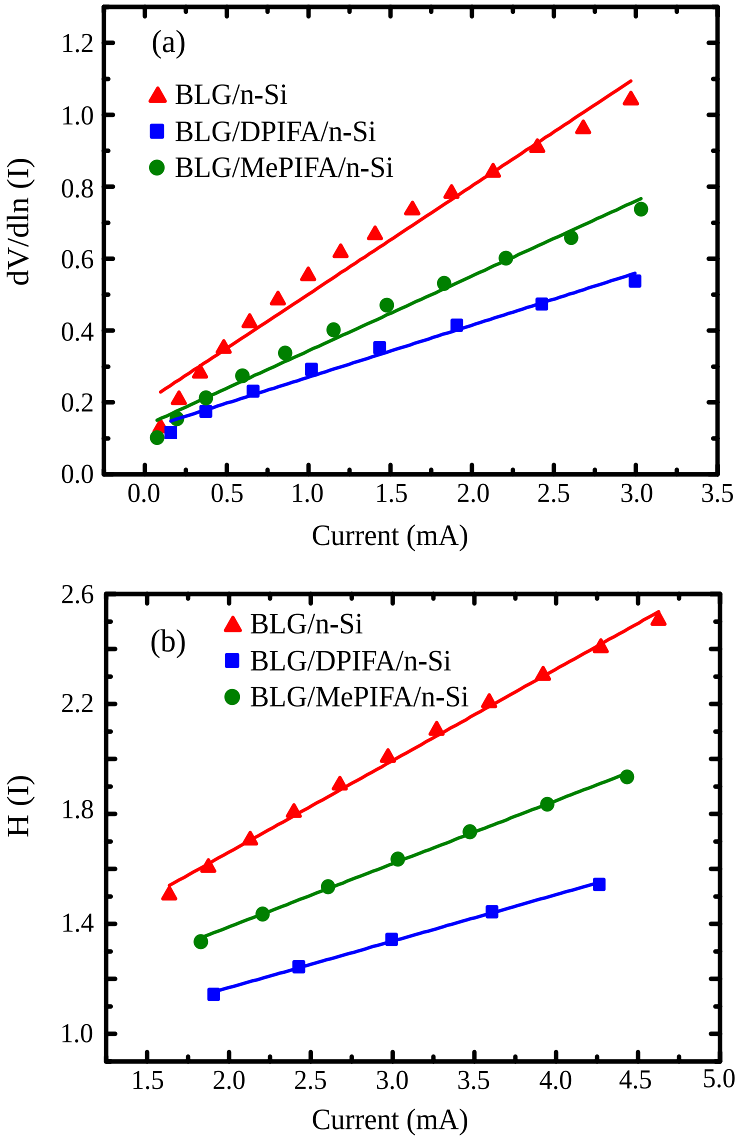

Figure 5.5. (a) *dV/dln (I)* vs *I* and (b) *H(I)* vs plots of bare and SAMs modified Schottky devices.

R_s provides information about the interface properties between graphene and n-Si. Values of the series resistance were calculated from both of the slope of the *dV/dln (I)* vs. *I* and *H(I)* vs *I* plots and it is decreased with the SAMs surface improvement In the presence of SAM molecule, incompatible surface between graphene and n-Si is decreased. Therefore, charge transfer was improved owing to due to π-π interaction, leading to lower resistance at the interface. In addition, while the *n* that was calculated from the intercept of the *dV/dln (I)* vs. *I* plot of the SAM included devices were higher than that of bare graphene diodes, barrier height decreased from 0.931 eV to 0.720 eV with DPIFA and MePIFA surface modification of silicon surface due to compatible interface between graphene and n-Si. Diode with DPIFA SAMs showed better characteristic than that of diode modified by MEPIFA SAMs. Since, MEPIFA SAMs molecule includes longer chain lengths and methyl groups restricting π-π interaction between SAMs and graphene. These limitations of π-π interaction and extra chain length obstruct charge transfer when compared to DPIFA molecules and thus, diode with DPIFA molecule has lower SBH and R_s values (Table 5.1).

Table 5.1. Major Schottky diodes parameters; the ideality factor, n; the series resistance, R_s; the SBH, φ_b; and surface potential.

	n	**φ_b (eV)**	**Surface Potential (V)**	**$^{dV/dlnI}R_s$ (Ω)**	**$^{H(I)}R_s$ (Ω)**
graphene/n-Si	1.06	0.93	0.14	301	333
graphene/MePIFA/n-Si	1.13	0.82	0.19	208	229
graphene/DPIFA/n-Si	1.15	0.72	0.38	144	169

5.2. The Impact of Single Carboxylic Acid SAMs on Graphene/Si Schottky Diodes

5.2.1. Structural Characterization Results

For structural and electronic properties of diode systems consisting of TPA and CAR molecules, graphene and SiO_2, we performed Density Functional Theory (DFT) calculations. At first the single TPA and CAR molecules were investigated. Both molecules are structurally similar in which the head group of both molecules is carboxylic acid and the head group and the spacers are linked by the triphenyl. However, the TPA and CAR have diphenylamino and carbazole as a spacer, respectively. Although the molecules have similar structures, the electronic properties are different. As shown in Figure 5.6, the calculated energy difference between the HOMO and LUMO states for the TPA and CAR molecules were 2.17 and 2.33 eV within GGA, respectively. The level of HOMO and LUMO states are also shown in Figure 5.6. For both molecules the HOMO state charge densities are localized on the spacer part, on the other hand, the LUMO state charge densities are appeared on head-group. In addition, the work functions were calculated to be 4.58 and 4.98 eV for the TPA and CAR molecules, respectively. Such a large difference between similar molecules can be correlated with the deeper Fermi level of CAR molecule because of having strong C-C bonds instead of C-H bonds at carbazole part. In addition, considering the experimental synthesis procedure one may expect formation of defective and misoriented domains of TPA and CAR SAMs and therefore the slight differences between the experiment and DFT results in the work function are acceptable.

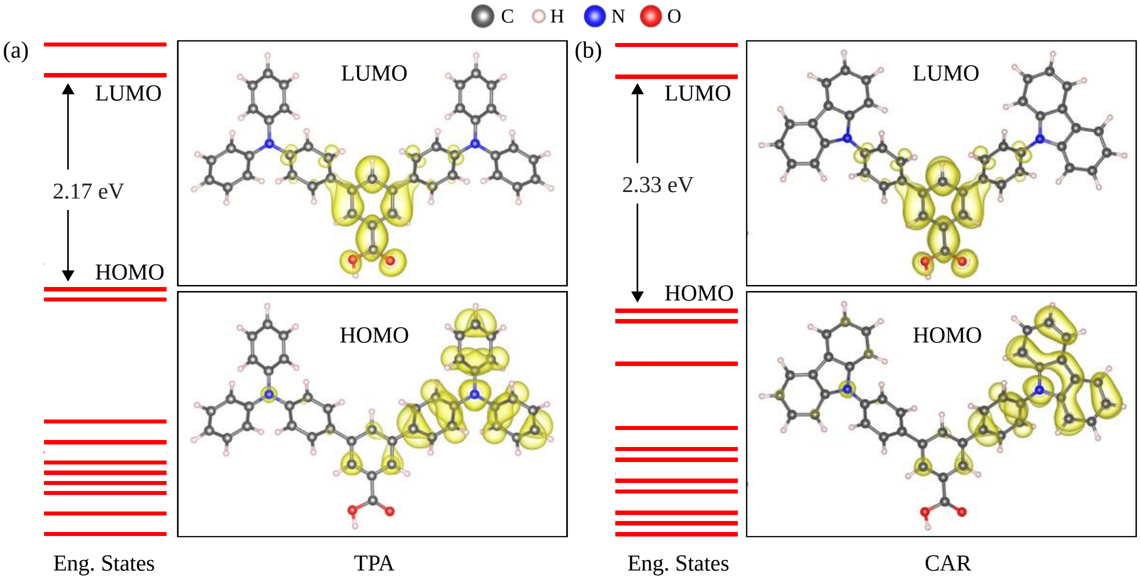

Figure 5.6. Chemical structures of TPA and CAR SAMs. (a) and (b) represent the states (left) and HOMO/LUMO charge densities (right upper/lower) for TPA and CAR molecules, respectively.

5.2.2. Raman Spectroscopy Analysis

Raman spectra indicates typical appearance of graphene transferred onto SiO_2/Si including D band (1367 cm^{-1}), G (1589 cm^{-1}) and 2D band (2711 cm^{-1}), respectively (Figure 5.7). The G band is the first Raman peak related to C-C stretching of sp^2 carbon.

The 2D band is the second order graphene peak and the D provides information about *sp*^{3} bond revealing amount of disorder in graphene. In addition to this, intensity ratios of G/2D and D/G have been utilized to identify the number of graphene layers and defect content of graphene (Table 5.2). $I_{2D/G}$ and $I_{D/G}$ were about 1.11 and 0.11 confirming the presence of high quality BLG. In addition, FWHM of 2D peak was found as 49 cm^{-1} affirming BLG grown on SiO_2/Si [85, 121].

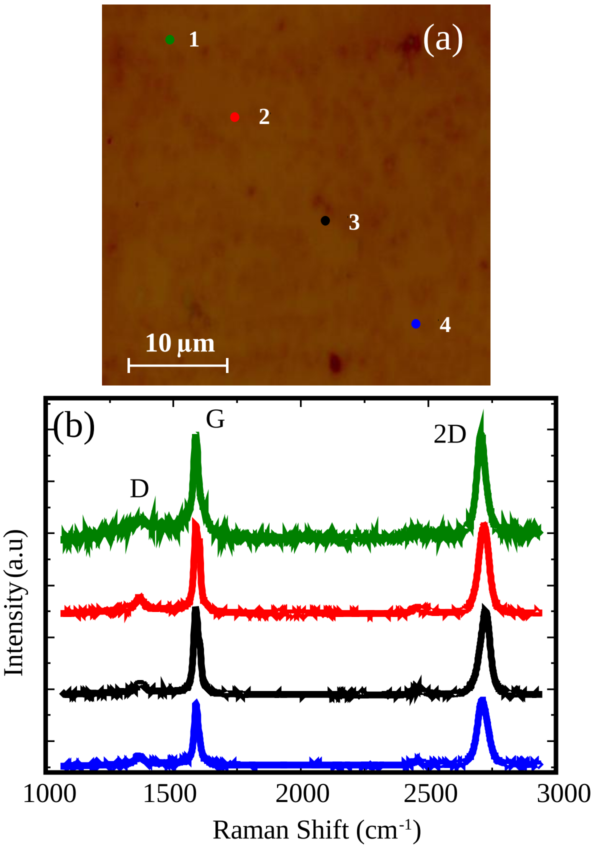

Figure 5.7. (a) Optical microscope image and (b) Multi points Raman spectra of bilayer graphene transferred on SiO_2/Si.

Table 5.2. $I_{D/G}$, $I_{2D/G}$ and FWHM of bilayer graphene on selected points.

Point	**$I_{D/G}$**	**$I_{2D/G}$**	**FWHM (cm^{-1})**
1	0.07	0.99	40
2	0.11	1.11	45
3	0.13	1.02	45
4	0.08	1.01	41

5.2.3. KPFM and CV Analysis

KPFM measurements were performed on bare n-Si and SAMs modified n-Si to prove modification of TPA and CAR SAMs. Figure 5.8 shows Mag versus bias voltage. When Mag signal is close to zero due to feedback in the SPM system, interaction force between tip and samples becomes zero. At this zero interaction-amplitude, applied dc voltage to the tip equals to the measured SP of the samples. The SP of bare n-Si, modified n-Si with TPA and CAR SAMs were found as 1.16, 1.43 and 1.51 V, respectively. The variation in SP values indicates surface modification of n-Si surface with TPA and CAR SAMs. In addition, the difference of SP values between TPA and CAR SAMs arises from the excess carbazole groups in CAR molecular structure lead to enhance electron density of n-Si surface with respect to the TPA SAMs.

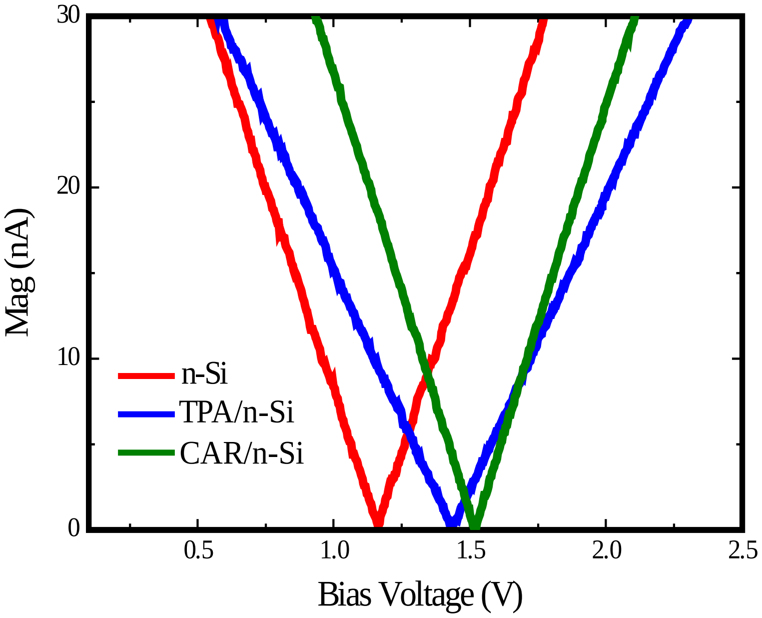

Figure 5.8. Surface potential differences of bare n-Si and modified n-Si with TPA and CAR SAMs.

Electrochemical property of bare TPA and CAR molecules on n-Si surface was investigated by cylic voltammetry (CV) measurement in anodic region (Figure 5.9). Reversible oxidation peaks were obtained from CV voltammogram as 0.31 and 0.40 V for TPA and CAR SAMs. The variation in potential compare to bare n-Si reveals the carboxylic acid group anchored to n-Si surface. Additionally, HOMO levels of TPA and

CAR molecules were determined from the onset of oxidation potential from the CV data using the following relation,

$$E_{HOMO} = -e(E_{ox} + 4.4)V \tag{5.1}$$

where E_{ox} is the oxidation peak and 4.4 is the ferrocene value. The HOMO level values of TPA and CAR molecules were obtained to be 4.71 and 4.8 eV, respectively. The trend in the HOMO levels of TPA and CAR molecules are consistent with the DFT calculations.

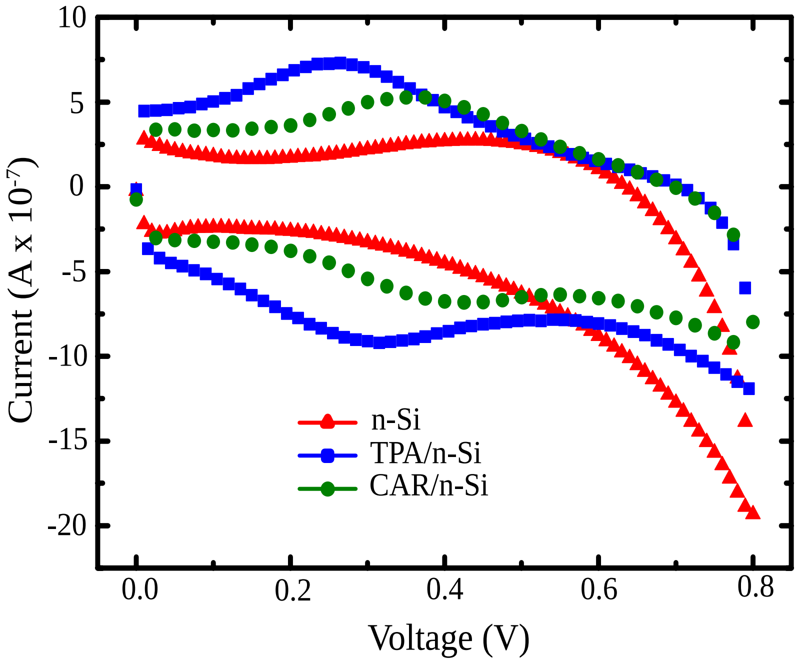

Figure 5.9. Cyclic voltammetry of bare n-Si and SAMs modified n-Si with TPA and CAR molecules.

The picture of graphene/SAMs/Si device bonded on the chip carrier, device structures of bare and SAMs modified diodes and bonding mechanism between carboxylic acid based SAMs and n-Si with native oxide are schematically illustrated in Figure 5.10. The carboxylic acid group anchored to n-Si surface due to the ester bond on the surface, resulting in facilitating charge injection over the π-conjugated structure.

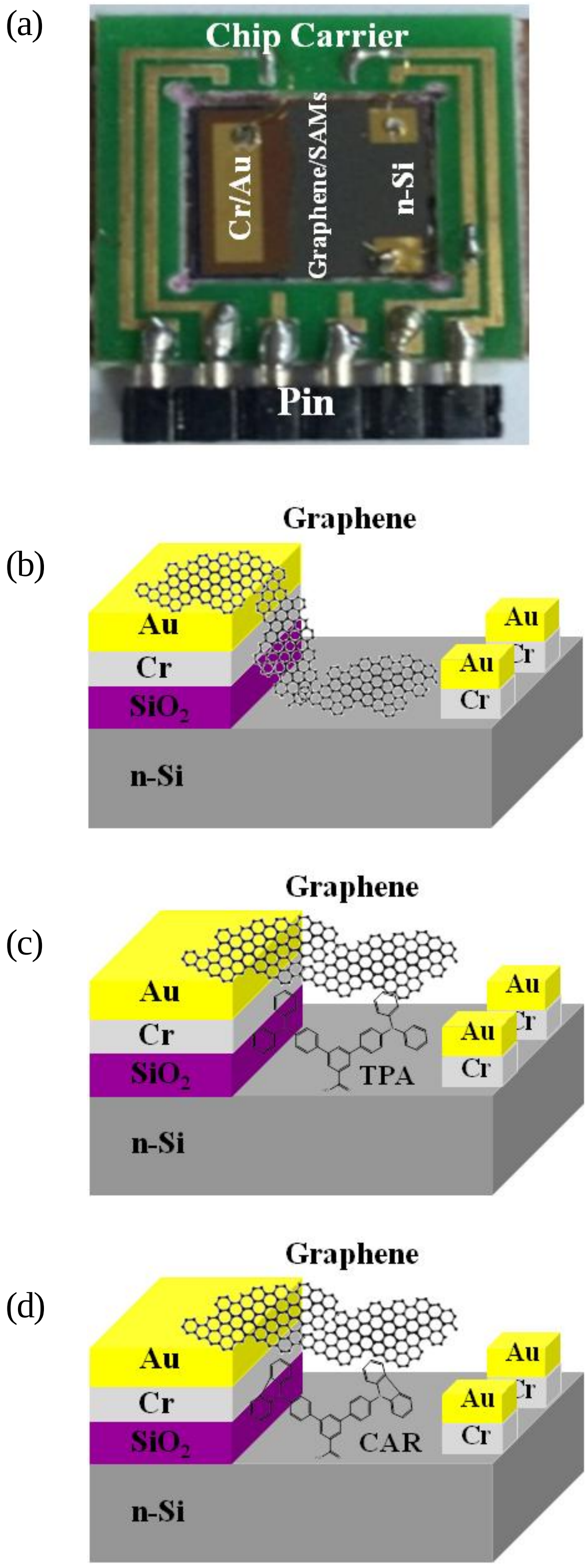

Figure 5.10. (a) Picture of graphene/SAMs/Si device bonded on chip carrier. Device structures of (b) graphene/n-Si, (c) graphene/TPA/n-Si and (d) graphene/CAR/n-Si.

5.2.4. Electronic Characterization of Graphene/Si Schottky Diodes

Driving current capability of Schottky diodes is superior to typical p-n junctions. Therefore, high current, low voltage and rectifying behavior are desired device properties for the Schottky diode applications. The *I-V* characteristics of BLG/n-Si and BLG/SAMs (TPA and CAR)/n-Si diodes were shown in Figure 5.11 (a). Three devices exhibited rectification characteristic verifying Schottky junction formation at the BLG/n-Si interface.

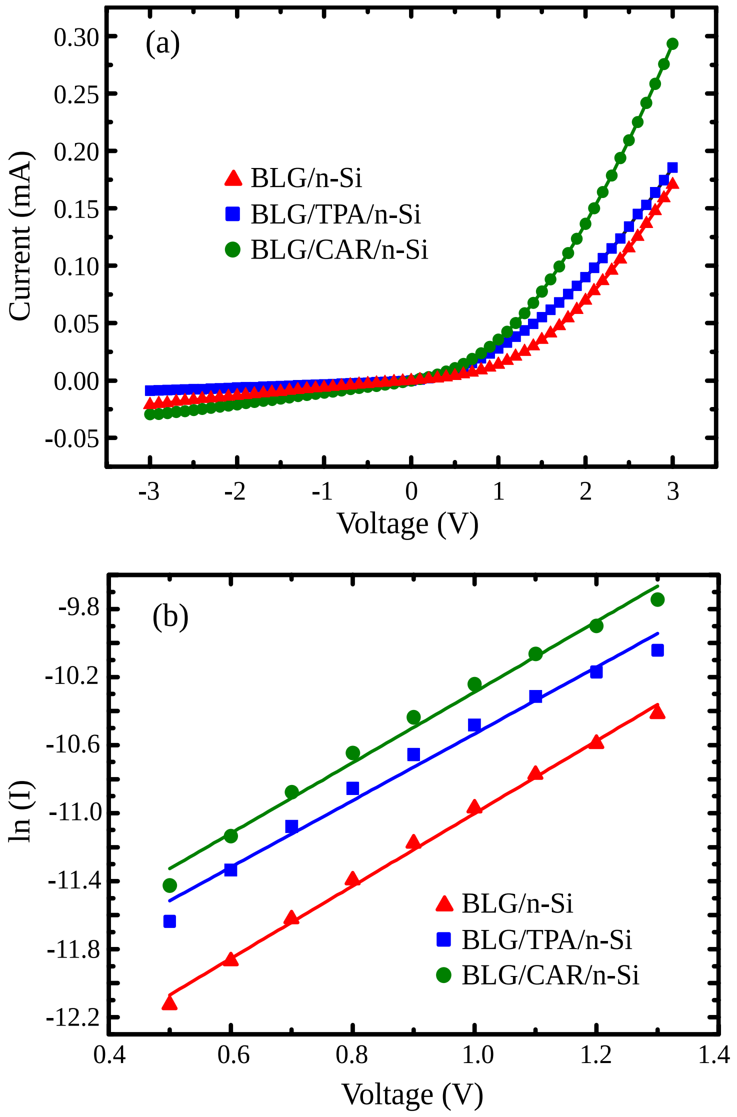

Figure 5.11. (a) *I-V* characteristic and (b) *ln(I)-V* plot of bare and SAMs modified Schottky devices.

Additionally, reducing impurities and improving junction between BLG and n-Si interface due to the presence of SAMs, result with the lower turn-on voltage (V_T) with respect to the bare device (Table 5.3). This implies that SAMs based diodes provide relatively less power wasted in comparison to the bare diode.

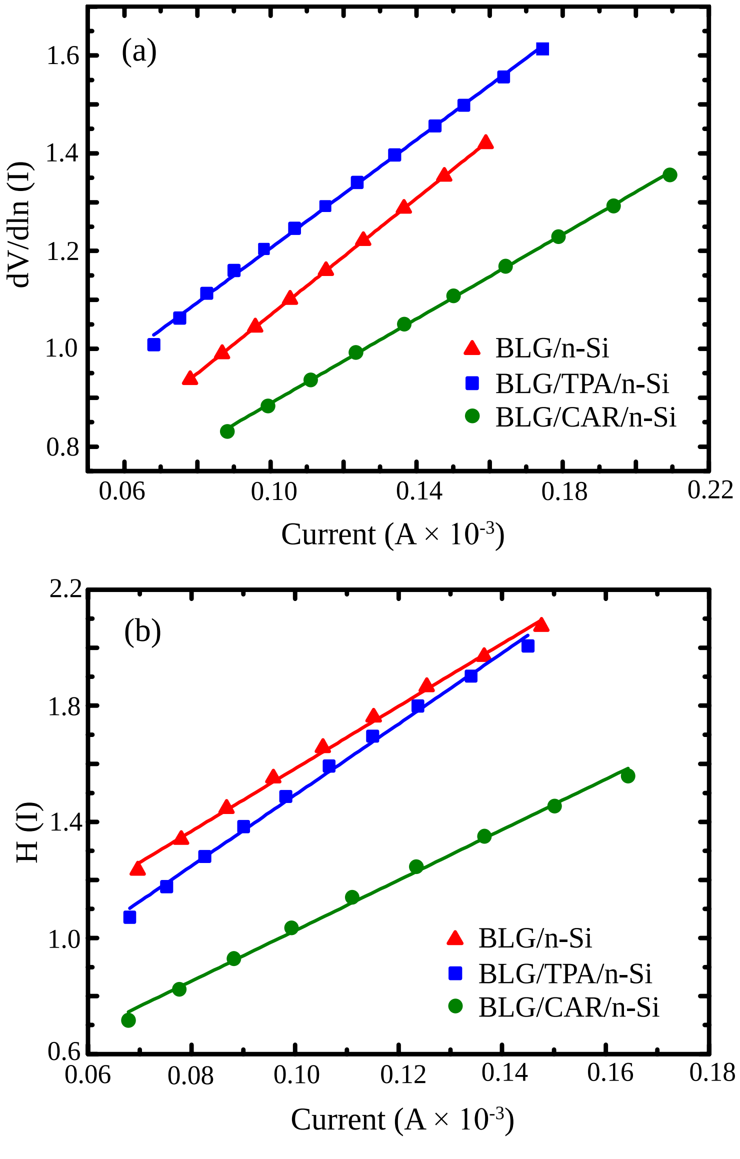

Figure 5.12. (a) *dV/dln (I)* vs *I* and (b) *H(I)* vs *I* plots of bare and SAMs modified Schottky diodes.

The *I-V* characteristic of Schottky diode can be described by thermionic emission model. If the equation 3.34 is rearranged and differentiated with respect to *I*, *n* is determined from the slope of the linear region of *ln(I)-V* curve as indicated in Figure

5.11 (b). The ideality factors of bare Schottky diode and SAMs modified Schottky diodes with TPA and CAR were calculated to be 2.13, 1.96 and 2.07, respectively. The variation of ideality factors in such devices is attributed to presence of SAMs between graphene and n-Si leading to additional interface states at the graphene-Si junction. Further, depending on difference in device fabrication, quality of graphene-Si heterojunction and data derivation in the fitting procedure, the ideality factor can be varied.

The R_s can be defined as the combination of contact resistance between graphene and Si, resistivity of graphene and Si and resistance of connecting wires [33]. Values of R_s of bare and SAMs modified devices were determined from the slope of the $dV/dln(I)$ vs I plot as shown in Figure 5.12 (a). The calculated R_s values, listed in Table 5.3, were about 5.96, 5.54 and 4.32 kΩ for BLG/n-Si, BLG/TPA/n-Si and BLG/CAR/n-Si diodes, respectively. R_s value of graphene/n-Si diode is comparable as reported for similar work [122]. Additionally, it is clear that Rs of SAMs modified diodes with TPA and CAR were decreased as compare to bare device owing to improving BLG/n-Si interface. Furthermore, R_s difference between TPA and CAR could be explained by the barrier height difference of BLG/TPA and BLG/CAR. The barrier height difference of BLG/CAR is lower than that of BLG/TPA, resulting in facilitating charge injection and lowering R_s.

In order to determine SBH, function $H(I)$ can be used. SBH can be obtained from the intercept of the linear region of $H(I)$ vs I plot as shown in Figure 5.12 (b). The estimated SBH of BLG/n-Si diode was about 0.54 eV which is comparable value for CVD grown graphene as reported in the literature [35]. The SBH of SAMs modified devices with TPA and CAR were calculated as 0.46 and 0.32 eV, respectively. The variation in SBH values can be explained by the different energy level of TPA and CAR SAMs. The energy barrier difference between CAR and BLG is less than the between TPA and BLG.

Figure 5.13 shows values of Schottky barrier height, series resistance and ideality factor as a function of air-exposure times up to 7 days. For all devices, although the values of Schottky barrier heights and ideality factors are quite stable and they are not altered significantly. Series resistances increase gradually with increasing air exposure times due to adsorbed molecules (H_2O and O_2) on the graphene which give rise to degradation on devices performance, resulting in high R_s at the graphene-Si interface.

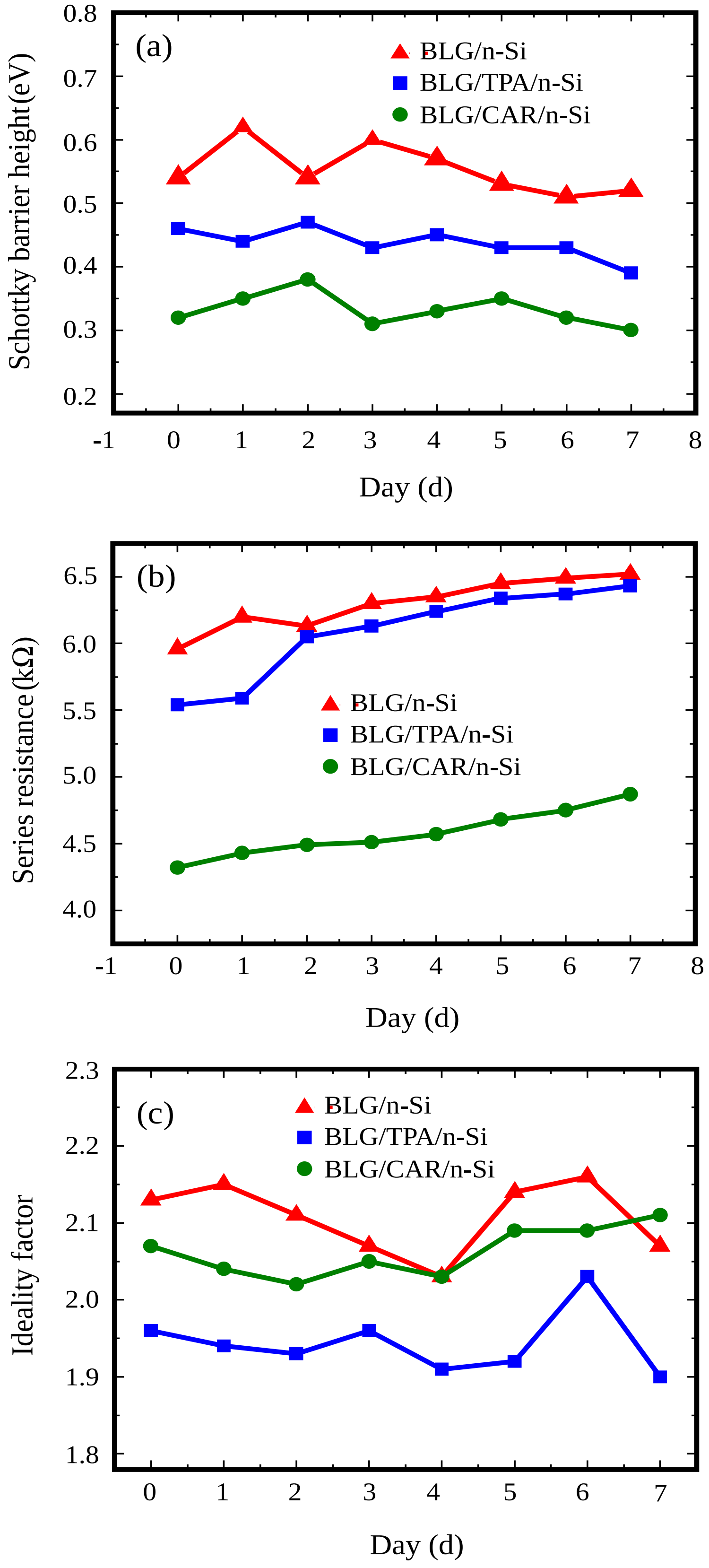

Figure 5.13. Values of (a) Schottky barrier height, (b) series resistance and (c) ideality factor as a function of air-exposure times up to 7 days.

Table 5.3. Major Schottky diodes parameters; the ideality factor, n; the series resistance, R_s; the Turn-on voltage, V_T ; and the SBH, φ_b.

	n	$^{dV/dlnI}$ **R$_s$ (kΩ)**	V_T **(V)**	ϕ_{sbh} *(eV)*
n-Si/BLG	2.13	5.96	0.7	0.54
n-Si/TPA/BLG	1.96	5.54	0.4	0.46
n-Si/CAR/BLG	2.07	4.32	0.3	0.32

As shown in Figure 5.14, the CAR molecule possesses lower Schottky barrier (1.63 eV) than the TPA molecule (1.87 eV) with the difference of 240 meV. It is necessary to note that effects such as defective surfaces, misaligned molecules, and the PR residues lead to differences between calculated and measured barrier values. When we consider the similar synthesis procedure, such effects are also similar cumulatively for the both TPA and CAR molecules. To sum up theoretical calculations is in good agreement with the experimentally observed Schottky device characteristics.

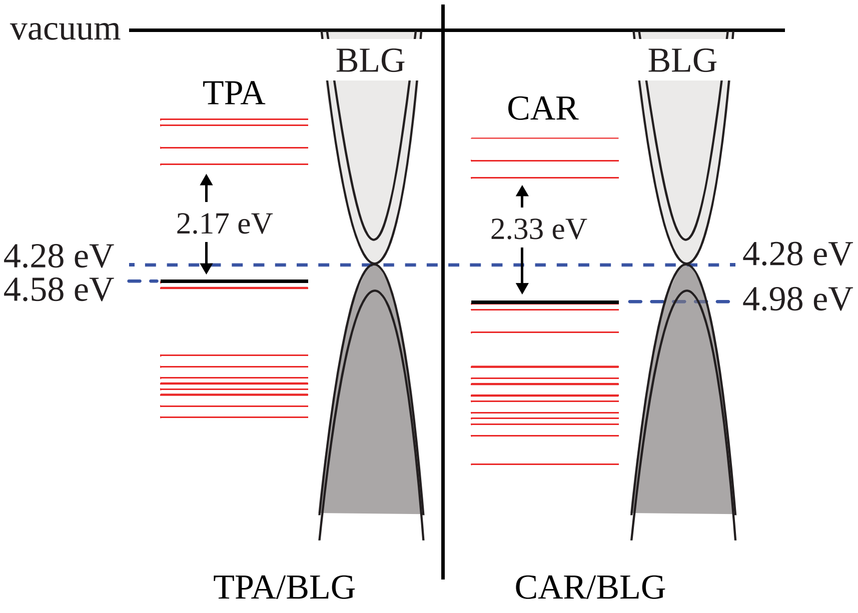

Figure 5.14. The band alignments of the graphene, TPA and CAR molecules with respect to their work function values.

5.3. P3HT-Graphene Bilayer Electrode on Si-based Schottky Junction Photodetectors

5.3.1. Characterization of P3HT Modified Graphene

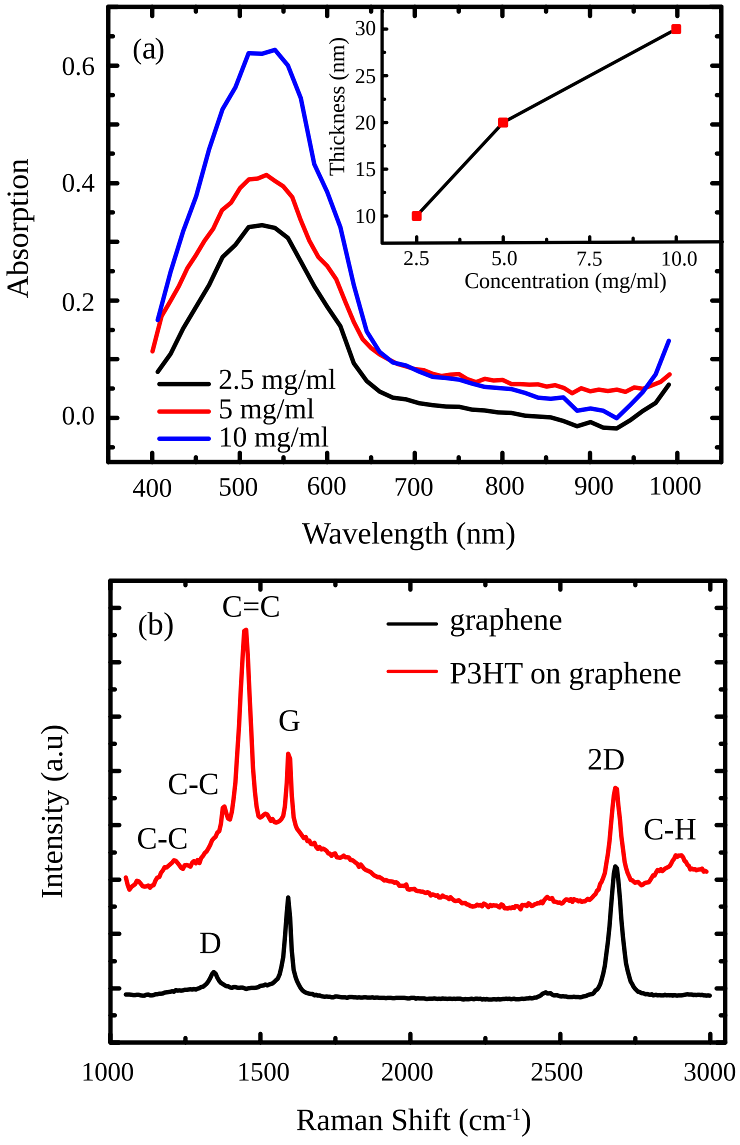

Figure 5.15. (a) Optical absorption spectra of P3HT films prepared from different concentrations on quartz. Inset: thickness of P3HT as a function of concentration. (b) Raman spectra of graphene and P3HT on graphene transferred onto SiO_2 coated Si.

Figure 5.15 (a) shows the optical absorption spectrum of P3HT-graphene film on quartz substrate. The P3HT film exhibits a main absorption peak at a wavelength of around 535 nm. This is attributed to the $\pi-\pi^*$ electronic transition and lattice vibration in crystalline P3HT domains. Concentration dependent thickness variations of dip-coated P3HT films are presented as the inset of Figure 5.15 (a). The measured thicknesses of P3HT films were about 10, 20 and 30 nm corresponding to the solution concentrations of 2.5, 5 and 10 mg/ml, respectively.

Figure 5.15 (b) shows the Raman spectra of graphene and P3HT film on graphene. In general, Raman spectrum of graphene exhibits typical band-peaks at the wavenumbers of D (1345 cm^{-1}), G (1593 cm^{-1}) and 2D (2685 cm^{-1}). The G band is the first Raman peak related to C-C stretching of sp^2 carbon. The 2D band is the second order graphene peak and the D band provides information on the amount of disorder in graphene. Intensity ratios of G/2D and D/G are used to determine the number of graphene layers and defect content of graphene. In our Raman analysis, $I_{G/2D}$ and $I_{D/G}$ were about 0.6 and 0.1, respectively, confirming the presence of monolayer graphene [123]. P3HT film has different modes at 1452 cm^{-1} for C=C skeleton symmetric stretching, 1379 cm^{-1} for C-C skeletal stretching, 2896 cm^{-1} for C-H stretching and 1208 cm^{-1} inter-ring C-C stretch mode, respectively [124]. The main Raman peak of P3HT coated graphene film at 1596 cm^{-1} and 2D peak at 2785 cm^{-1} are also present (Figure 5.15 (b)). However, the D peak is suppressed by C-C stretching of P3HT and the G peak is shifted from 1593 to 1596 cm^{-1}. This manifests that charge transfer occurs between P3HT and graphene [124].

5.3.2. Electronic Characterization of P3HT-Graphene/Si Schottky Photodetectors

Figure 5.16 (a) indicates sample mounted on a chip carrier including indium bonding and electrical pin. Figure 5.16 (b) shows SEM of P3HT-graphene/Si photodetector retaining P3HT-graphene film and Cr/Au electrode both on n-Si and SiO_2 sides of device structure. The three-dimensional view of the biased P3HT-graphene/Si device is depicted as in Figure 5.16 (c). The device structure consists of P3HT-graphene electrode and an underlying n-type Si substrate which was in contact with 3 mm x 5 mm of device area. Cr/Au was used to get ohmic contacts both on graphene and on n-Si. Upon light illumination in the visible wavelength range, electron-hole pairs were generated in the P3HT layer and in the depletion region of n-type Si substrate as well.

When a bias voltage was applied between the two electrodes, the electric field in the depletion region sweepeed the photogenerated electrons through to the n-type Si which was forward biased ($V_b < 0\ V$), whereas the holes moved towards the region underneath reverse biased ($V_b > 0\ V$) P3HT/graphene. Because of the fact that the photogenerated charge carriers were collected separately at the corresponding electrodes, this yielded a measurable photocurrent in the device. Figure 5.16 (d) demonstrates the schematic illustration for the energy-band diagram of P3HT-graphene/Si photodetector under a reverse bias condition. When P3HT-graphene and n-Si came in a contact, a depletion region and Schottky barrier (φ_b) are formed at the graphene/n-Si interface due to the difference between their corresponding Fermi levels [2, 120, 125]. Hence, the electrons in n-Si tended to flow into graphene until the Fermi levels were aligned across the junction. Under the illumination, incident light went through P3HT/graphene bilayer electrode and and penetrated into the n–Si to generate electron-hole pairs. The holes formed in the P3HT layer were transferred to the graphene via charge transfer doping, leading to p-type doping which increases built-in potential and junction field [17, 29]. This gave rise to the efficient separation of the photogenerated charge carriers in the depletion region and the holes moved to the graphene, whereas the electrons were transferred to the Si, enhancing the photocurrent of the device.

As will be discussed further, the device with 20 nm thick P3HT film displays the best performance in terms of current density (J)-voltage (V) characteristics and time-dependent photocurrent behavior are presented in Figure 5.17 (a) and (b). Both graphene/Si and P3HT-graphene/Si photodetectors exhibited rectification behavior confirming the Schottky junction formation at the graphene/Si interface. Additionally, while dark current of graphene/Si device at zero bias was about 6 nA, P3HT-based device was measured as 40 nA. Such a small increment of dark current is attributed to the presence of surface states with high density. Time-dependent photocurrent measurements of graphene/Si and P3HT-graphene/Si photodetectors were conducted over several switching on/off cycles under 540 nm light illumination at bias voltage of -0.1 V. The measurements were done within a total time of 210 s for 30 s intervals. As shown in Figure 5.17 (b), the measured current of the devices display two different states at relatively low incident light power (20 μW); a low-current state at around 32 μA in dark and average photocurrents of about 46 and 50 μA for graphene/Si and P3HT-graphene/Si photodetectors, respectively.

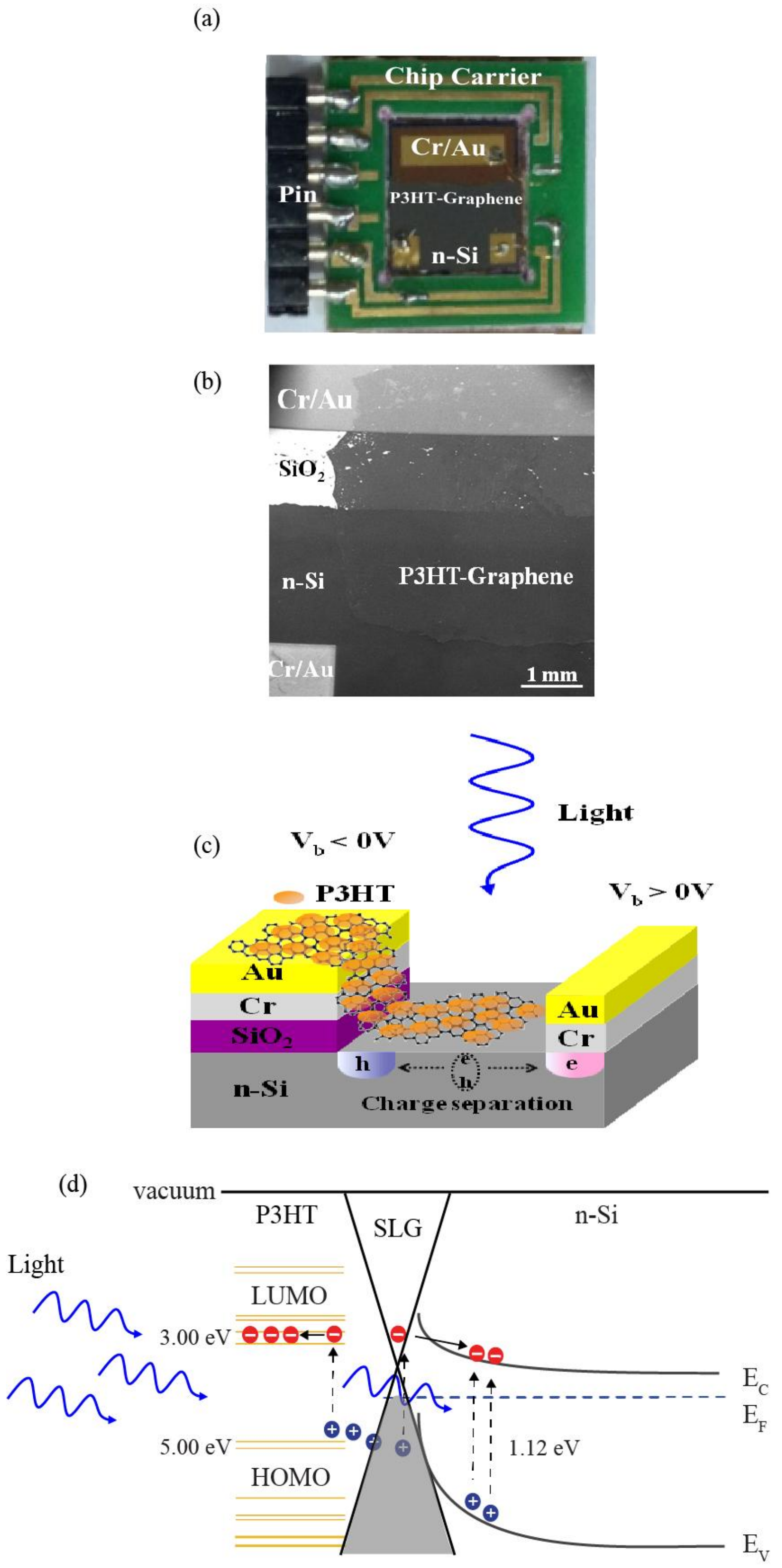

Figure 5.16. (a) P3HT–graphene/Si sample bonded on chip carrier. (b) Low-magnification SEM image of the fabricated P3HT–graphene/Si device. (c) Schematic cross-section view of the biased P3HT–graphene/Si device. The dashed arrow describes separation of photogenerated charge carriers. (d) Energy band diagram of P3HT–graphene/Si photodetectors.

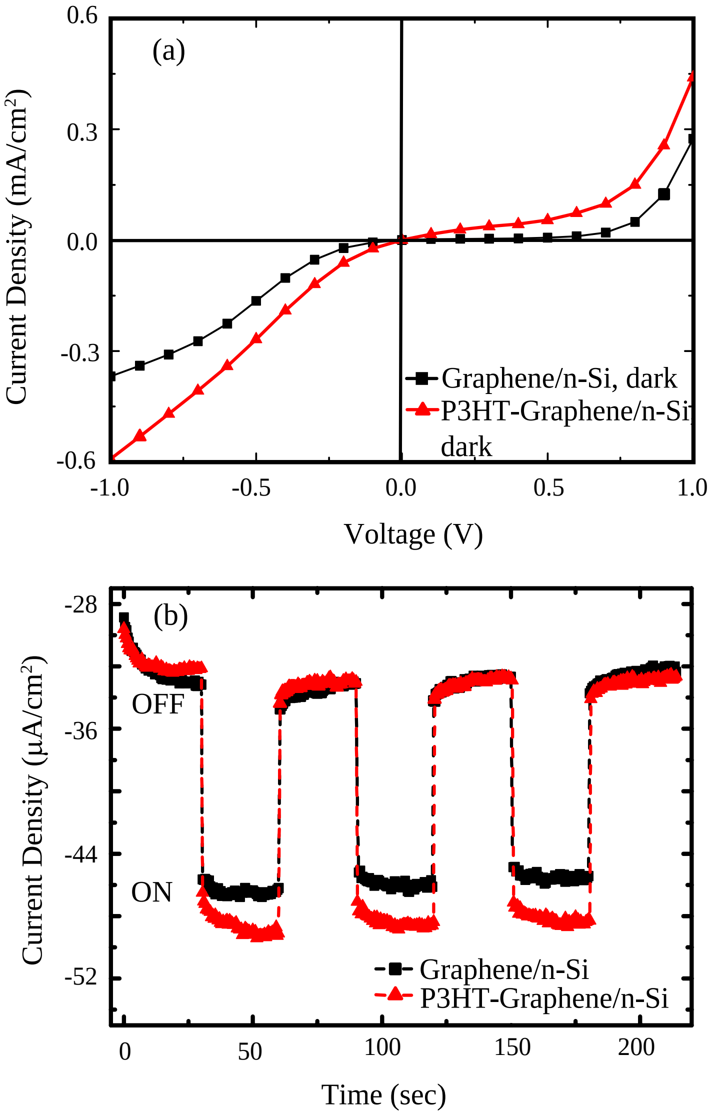

Figure 5.17. (a) The $J-V$ curve of the graphene/Si and P3HT-graphene/Si in dark. (b) Photoswitching behavior of the graphene/Si and P3HT-graphene/Si photodetectors under 540 nm light with an intensity of 20 μW at bias voltage of -0.1 V.

Additionally, for P3HT-graphene/Si photodetector, upon the light irradiation, a sharp increase in the current was followed by an exponential decay. As the light was turned off, a rapid downward trend in the current can be seen, following an exponential growth. The time constants for the growth and decay of the photocurrents were determined as 4.7 and 8.1 s, respectively. Furthermore, photoswitching characteristics of both devices show reversible photocurrent behavior and good stability. Our device with P3HT molecules was stable against air-exposure up to a period of about five days. However, after three months, the device was affected due to the adsorption of atmospheric molecules on the P3HT film, resulting in a degradation of device performance and stability [126-127]. Therefore, the device needs to be passivated with a proper encapsulation layer for long-term stability.

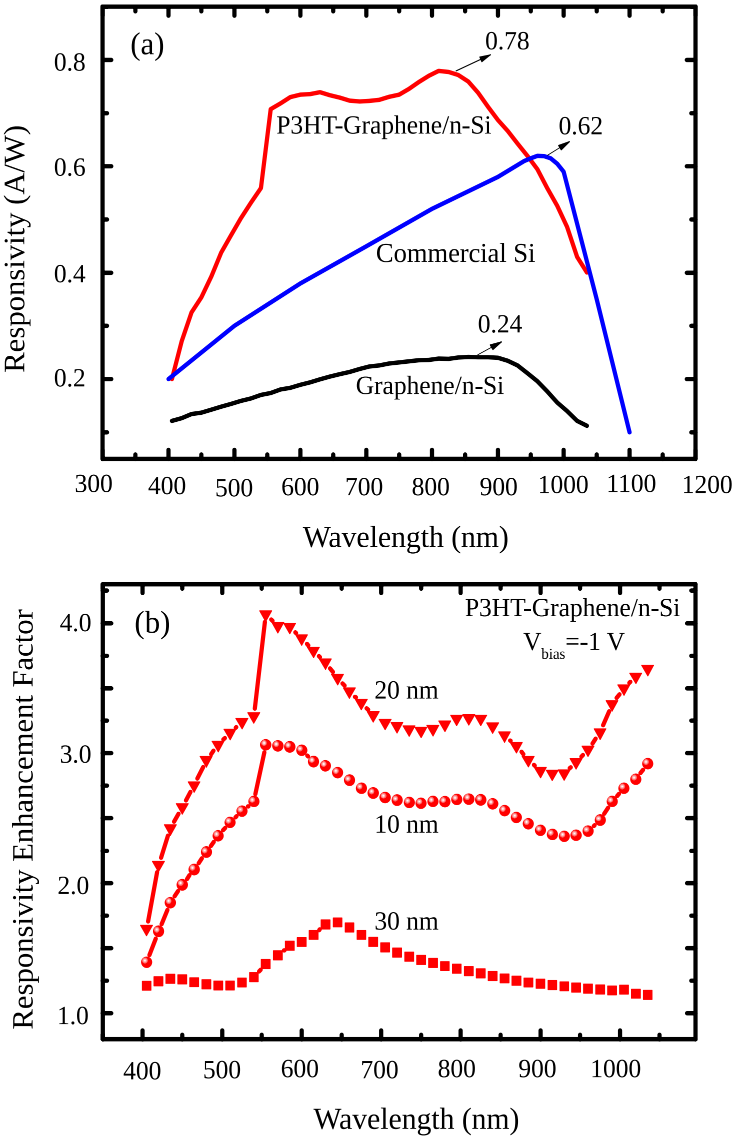

Figure 5.18. (a) Responsivity of graphene/Si, P3HT-graphene/Si and commercial Si photodetectors under bias voltage of -1 V. (b) Responsivity enhancement factor of P3HT based devices at different thicknesses.

Photoresponsivity is one of the most important parameters for the light sensing capability of photodetector devices and can be written as [126]

$$R = (I_{photo} - I_{dark})/P \tag{5.2}$$

where I_{photo} is the photocurrent, I_{dark} is the dark current and P is the optical power of incident light. Figure 5.18 (a) displays spectral responsivity of graphene/Si, P3HT-graphene/Si and commercial (Thorlabs) Si photodetectors under an applied reverse bias of 1 V. The graphene/Si photodetector exhibited typical Si based responsivity behavior similar to that reported in previous literature [14, 17]. The obtained maximum responsivity reached 0.24 AW^{-1} at the wavelength of 850 nm, in correlation with typical optical absorption spectrum of n-type Si. However, the respective photoresponsivity exhibited a downward trend below the cutoff wavelength of 1100 nm that corresponded to an energy level which was below the band gap energy of Si. For the commercial photodetector, the photoresponsivity with linear character was presented up to a wavelength of 950 nm and then decayed due to the Si absorption edge. P3HT-graphene bilayer electrode based Si photodetector presents not only higher responsivity but also wider wavelength coverage with respect to graphene/Si and commercial Si photodetectors. The obtained maximum responsivity at the wavelength of 850 nm was about 0.78 AW^{-1}. It is clear that the maximum responsivity of fabricated P3HT-graphene/Si device is 3.2 and 1.2 times higher than the maximum responsivities of graphene/Si and commercial Si photodetectors, respectively. The responsivity started to increase at the absorption onset wavelength of P3HT (Figure 5.18 (a)) and reached to a maximum value around 850 nm benefiting from the Si absorption. However, the slope of the decay observed for the wavelengths above 990 nm was much lower than that of the one observed in commercial Si photodetector. This can be attributed to P3HT-induced increment of responsivity at the higher wavelengths. Upon the light illumination, the holes in P3HT were transferred to graphene layer which is unintentionally p-doped [128-129], resulting in lowering the Fermi level of graphene which led to a larger built-in potential between n-Si and graphene. A larger built-in potential gives rise to a wider depletion region providing efficient dissociation of photon-generated carriers [17, 130]. A similar manner of the responsivity curve at higher wavelength (> 990 nm) can be found in literature [17]. Furthermore, the photodetection seen at the wavelengths > 990 nm can also be related to the localized polaron absorption of P3HT exceeding up to 1100 nm [131]. As displayed in Figure 5.18 (b), changing the thickness of P3HT caused an alteration in the responsivity enhancement factors. When the thickness of P3HT was increased from 10 to 20 nm, the responsivity enhancement factor also increased and displayed two distinct peaks at around 540 and 850 nm originating from the absorption of P3HT and Si, respectively. However, 30 nm thick P3HT film exhibited a red-shift due to the agglomeration of P3HT and decreased the responsivity enhancement factor. Increasing the thickness of P3HT may increase the density of electrons in the excited states upon irradiation and consequently facilitate the hole doping of graphene. However, when the exciton diffusion length of regioregular P3HT is considered [132], in such a thick film, the photogenerated excitons may also recombine before reaching the P3HT-graphene interface and cause a decrease in the responsivity enhancement factor.

The specific detectivity (D^*) is one of figures of merit for a photodetector and can be given as [15]

$$D^* = \frac{A^{1/2}R}{\sqrt{2eI_d}} \tag{5.3}$$

where A is the active area of the photodetector, R is the responsivity, e is the elementary charge and I_d is the dark current. As shown in Figure 5.19 (a), the calculated D^* of graphene/Si device was about 19 x 10^9 Jones, whereas D^* of P3HT-Graphene/Si photodetector exceeded 26 x 10^9 Jones at 850 nm which are higher than the values reported in similar works [9, 17]. Apparently, P3HT-graphene bilayer electrode improved the detection limit of the graphene/Si photodetector. However, there is reversal D^* between the graphene/Si and P3HT-graphene/Si photodetectors at approximate 450 nm. Considering the dark currents of both devices, the responsivity of the P3HT–graphene/Si photodetector was not high enough compared to the graphene/Si photodetector at lower wavelengths due to the absorption of the P3HT and Si. This is because of the fact that the D^* of the graphene/Si device increased with respect to the D^* of the P3HT modified graphene/Si photodetector at wavelengths below 450 nm.

Noise equivalent power (NEP) describes the incident power required to obtain a signal to noise ratio of 1 at a bandwidth of 1 Hz. The NEP can be obtained by using the Flicker noise (1/f), shot noise and thermal noise of a device and this gives information about the minimum detectable signal of the photodetector and can be written as [133-135] [133, 136]

$$NEP = A^{1/2}/D^* \tag{5.4}$$

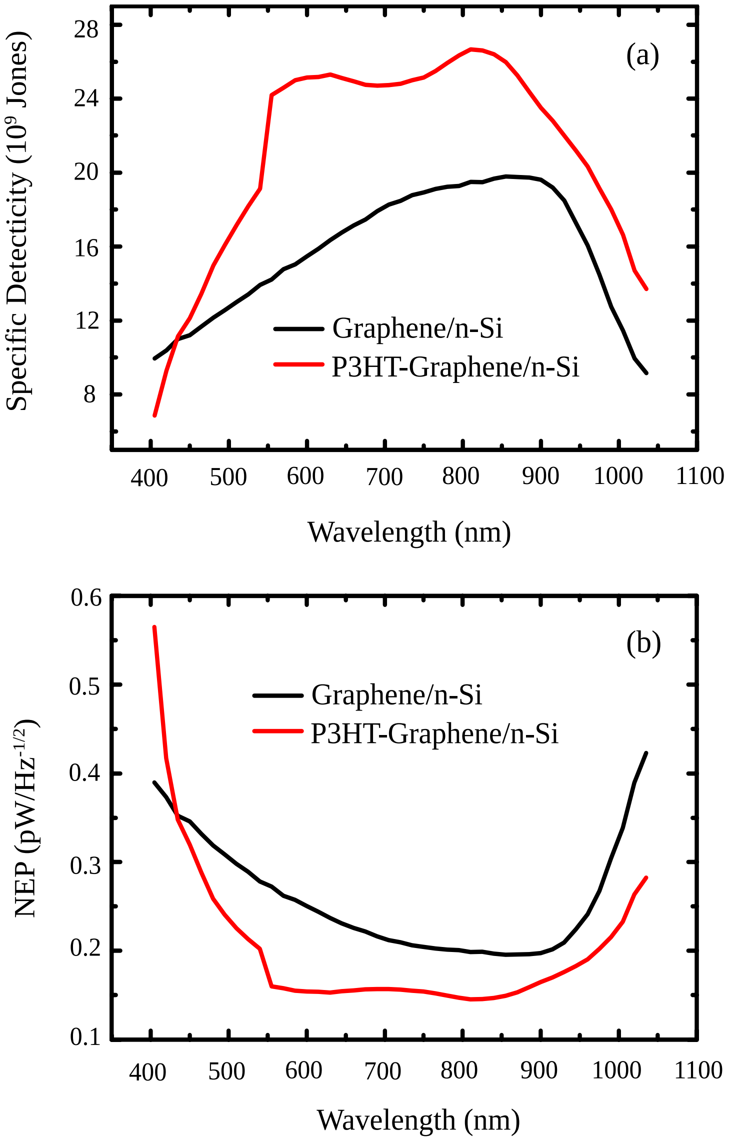

Figure 5.19. (a) Spectral dependence of D^* and (b) NEP of the graphene/Si and P3HT-graphene/Si photodetectors.

Figure 5.19 (b) shows the spectral NEP of graphene/Si and P3HT-graphene/Si photodetectors. The obtained minimum NEP was about 0.20 pW Hz$^{-1/2}$ for graphene/Si at 850 nm. However, the device with P3HT-graphene bilayer electrode exhibited low NEP down to 0.14 pW Hz$^{-1/2}$ at the wavelength of 850 nm. This value is higher than that reported in a similar work [9]. Additionally, NEP values of P3HT-graphene/Si photodetector changed from 0.15 to 0.14 pW Hz$^{-1/2}$ for the wavelength range between

550 and 885 nm. Such a small variation in the NEP value enables the device to be operating for a broader bandwidth ranging from visible to near-infrared spectrum.

The performance characteristics of the Si photodetectors with graphene electrodes are compared in Table 5.4 with respect to their reference samples. It is clear that P3HT-graphene bilayer electrode improved the performance of the respective photodetector in terms of the device parameters of *R*, *D** and NEP. As compared to previously reported graphene based Si photodetectors, the photoresponsivity of graphene/Si device was restricted to about 0.40 AW^{-1} due to low light absorption/gain ratio. Additionally, plasmonic silver nanoparticles (Ag-Nps) on graphene electrode was used to enhance the light interaction and provide efficient Schottky junction formation [11]. However, the use of these Ag-Nps hindered and limited the photoresponsivity of the device at around 0.1 AW^{-1}. Furthermore, Si-QDs–graphene coupled electrode was used to increase the built-in potential. The device was shown to exhibit relatively high *R*, *D** and NEP values [17].

Table 5.4. Summary of the performances of the graphene based Si photodetectors.

Device Structure	I_{dark} (nA)	R (AW^{-1})	D^* (10^9) (Jones)	NEP ($pW/Hz^{-1/2}$)	Reference
graphene/Si	6	0.24	19	0.20	This work
P3HT-graphene/Si	40	0.78	26	0.14	This work
graphene/Si	-	0.43	7.7	1.0	9
graphene/Si	-	0.23	-	-	14
Ag-Nps/graphene/Si	-	0.10	-	-	11
graphene/Si-QDs/Si	-	0.35	1.0	-	16
Si-QDs/graphene/Si	-	0.50	7.4	6.7	17

CHAPTER 6

CONCLUSIONS

This thesis focused on developing graphene-organic hybrid electrodes for Silicon based Schottky devices. Two different sets of carboxylic acid based SAMs were used to improve the rectification character of the Schottky junction formed at graphene/n-Si interface. While the first set of SAMs consists of MePIFA and DPIFA, the second set of SAMs contains TPA and CAR. In addition to this, P3HT, which is known to be an electron donor and absorb light in the visible spectrum, was utilized to create P3HT/graphene bilayer electrodes. The results of experiments were discussed in detail within three main chapters.

In Chapter 5.1, the effect of aromatic SAMs on the photodetection performance of graphene/Silicon Schottky diode was investigated. MePIFA and DPIFA molecules were used as SAMs to improve graphene/n-Si substrate interface properties. The increment of surface potential in SAMs modified n-Si surface was found to reduce the energy barrier between aromatic SAMs and graphene with respect to bare device. The *I-V* characteristics of bare graphene/Si and SAMs modified graphene/Si revealed Schottky barrier with rectifying behavior. Compared to bare diode, SAMs modified graphene/Si devices exhibited low Schottky barrier with a height of 0.72 eV. This gave rise to effective charge injection at the graphene/Si interface resulting in reducing R_s and low turn-on voltage. Additionally, DPIFA SAMs exhibited better diode performance compare to MePIFA SAMs due to the absence of methyl group which greatly hinders the π-π interaction between SAMs molecule and graphene.

In Chapter 5.2, the impact of SAMs on graphene/Si Schottky diodes was investigated. We found that TPA and CAR SAMs can be used to improve the rectification of graphene-Si interface. Additionally, the *I-V* characteristics of bare graphene/Si and SAMs modified graphene/Si diodes showed rectification behavior confirming the Schottky junction formation at the interface. The turn-on voltage of SAMs modified diodes was found to decrease from 0.7 V to 0.3 V. This implies that SAMs modified diodes have less power consumption when compared to bare diode. Besides, the variation in device performance between TPA and CAR based graphene/Si diodes is related to lower energy barrier of CAR/BLG system than that of TPA/BLG with the difference of 100 meV. This supported with DFT calculations which were obtained the difference of 240 meV.

In Chapter 5.3, we have investigated the effect of P3HT-graphene bilayer electrode on the photoresponsivity characteristics of Silicon based Schottky photodetectors. UV-Vis and Raman spectroscopy measurements have been conducted to confirm the optical and electronic modification of graphene by P3HT thin film. Current-voltage measurements of graphene/Si and P3HT-graphene/Si revealed the rectification behavior and the Schottky junction formation at the graphene/Si interface. Time-resolved photocurrent spectroscopy measurements exhibited excellent durability and fast response speed of fabricated devices. We found that the maximum responsivity of P3HT-graphene/Si photodetector reached to 0.78 AW^{-1} at a wavelength of 850 nm. The value of this responsivity was 3.2 and 1.2 times higher than that of bare graphene/Si photodetector and commercial Si photodetector, respectively. The observed increment in the photoresponsivity of P3HT-graphene/Si device was attributed to the charge transfer doping from P3HT to graphene within the spectral range between near-ultraviolet and near-infrared. Furthermore, P3HT-graphene electrode was found to improve the specific detectivity up to value of 26×10^{19} Jones at a wavelength of 850 nm. Besides, P3HT-graphene/Si photodetector exhibited low noise equivalent power down to 0.14 pW $Hz^{-1/2}$ which remained constant for the wavelength range between 550 and 885 nm. This enables the device to be operated for a broadband imaging.

To summarize, due to the presence of SAMs, rectification behavior of the Schottky junction was improved at the graphene/n-Si interface. This led to lower turn-on voltage, R_s and SBH with respect to the bare graphene/Si device. Additionally, SAMs based graphene/Si Schottky diodes improved on state voltage drop compared to bare graphene/Si diode, resulting in relatively less power consumption in switching applications. Furthermore, P3HT-graphene bilayer electrodes significantly enhanced the photoresponsivity characteristics of graphene/Si due to the effective charge transfer doping from P3HT to graphene under light illumination. This gave rise to higher Responsivity, Specific Detectivity and lower Noise Equivalent Power values compared to bare graphene/Si. The robust structure, lower Schottky barrier of SAMs/graphene interface and higher photoresponse of P3HT-graphene bilayer electrode hold promise for functional component in Si-based optoelectronic devices.

REFERENCES

1. Novoselov, K. S.; Geim, A. K.; Morozov, S.; Jiang, D.; Katsnelson, M.; Grigorieva, I.; Dubonos, S.; Firsov; AA, Two-dimensional gas of massless Dirac fermions in graphene. *nature* **2005,** *438* (7065), 197-200.

2. Kalita, G.; Hirano, R.; Ayhan, M. E.; Tanemura, M., Fabrication of a Schottky junction diode with direct growth graphene on silicon by a solid phase reaction. *Journal of Physics D: Applied Physics* **2013,** *46* (45), 455103.

3. Tongay, S.; Lemaitre, M.; Schumann, T.; Berke, K.; Appleton, B. R.; Gila, B.; Hebard, A. F., Graphene/GaN Schottky diodes: Stability at elevated temperatures. *Applied physics letters* **2011,** *99* (10), 102102.

4. Tomer, D.; Rajput, S.; Hudy, L.; Li, C.; Li, L., Inhomogeneity in barrier height at graphene/Si (GaAs) Schottky junctions. *Nanotechnology* **2015,** *26* (21), 215702.

5. Shivaraman, S.; Herman, L. H.; Rana, F.; Park, J.; Spencer, M. G., Schottky barrier inhomogeneities at the interface of few layer epitaxial graphene and silicon carbide. *Applied Physics Letters* **2012,** *100* (18), 183112.

6. Bolotin, K. I.; Sikes, K.; Jiang, Z.; Klima, M.; Fudenberg, G.; Hone, J.; Kim, P.; Stormer, H., Ultrahigh electron mobility in suspended graphene. *Solid State Communications* **2008,** *146* (9), 351-355.

7. Nair, R. R.; Blake, P.; Grigorenko, A. N.; Novoselov, K. S.; Booth, T. J.; Stauber,T.; Peres, N. M.; Geim, A. K., Fine structure constant defines visual transparency of graphene. *Science* **2008,** *320* (5881), 1308-1308.

8. Yu, Y.-J.; Zhao, Y.; Ryu, S.; Brus, L. E.; Kim, K. S.; Kim, P., Tuning the graphene work function by electric field effect. *Nano letters* **2009,** *9* (10), 3430-3434.

9. An, X.; Liu, F.; Jung, Y. J.; Kar, S., Tunable graphene–silicon heterojunctions for ultrasensitive photodetection. *Nano letters* **2013,** *13* (3), 909-916.

10. Lv, P.; Zhang, X.; Zhang, X.; Deng, W.; Jie, J., High-sensitivity and fast-response graphene/crystalline silicon schottky junction-based near-IR photodetectors. *IEEE Electron Device Letters* **2013,** *34* (10), 1337-1339.

11. Ayhan, M. E.; Kalita, G.; Kondo, M.; Tanemura, M., Photoresponsivity of silver nanoparticles decorated graphene–silicon Schottky junction. *RSC Advances* **2014,** *4* (51), 26866-26871.

12. Zhu, M.; Li, X.; Guo, Y.; Li, X.; Sun, P.; Zang, X.; Wang, K.; Zhong, M.; Wu, D.; Zhu, H., Vertical junction photodetectors based on reduced graphene oxide/silicon Schottky diodes. *Nanoscale* **2014,** *6* (9), 4909-4914.

13. Chen, Z.; Cheng, Z.; Wang, J.; Wan, X.; Shu, C.; Tsang, H. K.; Ho, H. P.; Xu, J. B., High responsivity, broadband, and fast graphene/silicon photodetector in photoconductor mode. *Advanced Optical Materials* **2015,** *3* (9), 1207-1214.

14. Riazimehr, S.; Bablich, A.; Schneider, D.; Kataria, S.; Passi, V.; Yim, C.; Duesberg, G. S.; Lemme, M. C., Spectral sensitivity of graphene/silicon heterojunction photodetectors. *Solid-State Electronics* **2016,** *115*, 207-212.

15. Wan, X.; Xu, Y.; Guo, H.; Shehzad, K.; Ali, A.; Liu, Y.; Yang, J.; Dai, D.; Lin, C.-T.; Liu, L., A self-powered high-performance graphene/silicon ultraviolet photodetector with ultra-shallow junction: breaking the limit of silicon? **2017**.

16. Shin, D. H.; Kim, S.; Kim, J. M.; Jang, C. W.; Kim, J. H.; Lee, K. W.; Kim, J.; Oh, S. D.; Lee, D. H.; Kang, S. S., Graphene/Si-Quantum-Dot Heterojunction Diodes Showing High Photosensitivity Compatible with Quantum Confinement Effect. *Advanced Materials* **2015,** *27* (16), 2614-2620.

17. Yu, T.; Wang, F.; Xu, Y.; Ma, L.; Pi, X.; Yang, D., Graphene Coupled with Silicon Quantum Dots for High-Performance Bulk-Silicon-Based Schottky-Junction Photodetectors. *Advanced Materials* **2016,** *28* (24), 4912 4919.

18. Li, Y.; Guo, Q.; Li, Z.; Pei, J.; Tian, W., Solution processable D–A small molecules for bulk-heterojunction solar cells. *Energy & Environmental Science* **2010,** *3* (10), 1427-1436.

19. Liu, Z.; Liu, Q.; Huang, Y.; Ma, Y.; Yin, S.; Zhang, X.; Sun, W.; Chen, Y., Organic photovoltaic devices based on a novel acceptor material: graphene. *Advanced Materials* **2008,** *20* (20), 3924-3930.

20. Baeg, K. J.; Binda, M.; Natali, D.; Caironi, M.; Noh, Y. Y., Organic light detectors: photodiodes and phototransistors. *Advanced Materials* **2013,** *25* (31), 4267-4295.

21. Zhang, L.; Li, Y.; Shi, J.; Shi, G.; Cao, S., Nonvolatile rewritable memory device based on solution-processable graphene/poly (3-hexylthiophene) nanocomposite. *Materials Chemistry and Physics* **2013,** *142* (2), 626-632.

22. Reyes-Reyes, M.; Kim, K.; Dewald, J.; López-Sandoval, R.; Avadhanula, A.; Curran, S.; Carroll, D. L., Meso-structure formation for enhanced organic photovoltaic cells. *Organic letters* **2005,** *7* (26), 5749-5752.

23. Lai, Y. C.; Wang, Y. X.; Huang, Y. C.; Lin, T. Y.; Hsieh, Y. P.; Yang, Y. J.; Chen, Y. F., Rewritable, Moldable, and Flexible Sticker-Type Organic Memory on Arbitrary Substrates. *Advanced Functional Materials* **2014,** *24* (10), 1430-1438.

24. Berson, S.; De Bettignies, R.; Bailly, S.; Guillerez, S., Poly (3-hexylthiophene) Fibers for Photovoltaic Applications. *Advanced Functional Materials* **2007,** *17* (8), 1377-1384.

25. Wu, Y.; Zhang, X.; Jie, J.; Xie, C.; Zhang, X.; Sun, B.; Wang, Y.; Gao, P., Graphene transparent conductive electrodes for highly efficient silicon nanostructures-based hybrid heterojunction solar cells. *The Journal of Physical Chemistry C* **2013,** *117* (23), 11968-11976.

26. Huang, J.; Hines, D. R.; Jung, B. J.; Bronsgeest, M. S.; Tunnell, A.; Ballarotto, V.;Katz, H. E.; Fuhrer, M. S.; Williams, E. D.; Cumings, J., Polymeric semiconductor/graphene hybrid field-effect transistors. *Organic Electronics* **2011,** *12* (9), 1471-1476.

27. Saini, V.; Li, Z.; Bourdo, S.; Dervishi, E.; Xu, Y.; Ma, X.; Kunets, V. P.; Salamo,G. J.; Viswanathan, T.; Biris, A. R., Electrical, optical, and nanocomposites morphological properties of P3HT-MWNT prepared by in situ polymerization. *The Journal of Physical Chemistry C* **2009,** *113* (19), 8023-8029.

28. Miller, S.; Fanchini, G.; Lin, Y.-Y.; Li, C.; Chen, C.-W.; Su, W.-F.; Chhowalla, M., Investigation of nanoscale morphological changes in organic photovoltaics during solvent vapor annealing. *Journal of materials chemistry* **2008,** *18* (3), 306-312.

29. Tan, W. C.; Shih, W. H.; Chen, Y. F., A Highly Sensitive Graphene-Organic Hybrid Photodetector with a Piezoelectric Substrate. *Advanced Functional Materials* **2014,** *24* (43), 6818-6825.

30. Xie, C.; Zhang, X.; Wu, Y.; Zhang, X.; Zhang, X.; Wang, Y.; Zhang, W.; Gao, P.; Han, Y.; Jie, J., Surface passivation and band engineering: a way toward high efficiency graphene–planar Si solar cells. *Journal of Materials Chemistry A* **2013,** *1* (30), 8567-8574.

31. Huisman, E. H.; Shulga, A. G.; Zomer, P. J.; Tombros, N.; Bartesaghi, D.; Bisri, S. Z.; Loi, M. A.; Koster, L. J. A.; van Wees, B. J., High gain hybrid graphene–organic semiconductor phototransistors. *ACS applied materials & interfaces* **2015,** *7* (21), 11083-11088.

32. Lin, Y.-J.; Lin, J.-H., Annealing effect on Schottky barrier inhomogeneity of graphene/n-type Si Schottky diodes. *Applied Surface Science* **2014,** *311*, 224-229.

33. Kim, D.-J.; Kim, G.-S.; Park, N.-W.; Lee, W.-Y.; Sim, Y.; Kim, K.-S.; Seong, M.-J.; Koh, J.-H.; Hong, C.-H.; Lee, S.-K., Effect of annealing of graphene layer on electrical transport and degradation of Au/graphene/n-type silicon Schottky diodes. *Journal of Alloys and Compounds* **2014,** *612*, 265-272.

34. An, Y.; Behnam, A.; Pop, E.; Ural, A., Metal-semiconductor-metal photodetectors based on graphene/p-type silicon Schottky junctions. *Applied physics letters* **2013,** *102* (1), 013110.

35. Sinha, D.; Lee, J. U., Ideal graphene/silicon Schottky junction diodes. *Nano letters* **2014,** *14* (8), 4660-4664.

36. Mohammed, M.; Li, Z.; Cui, J.; Chen, T.-p., Junction investigation of graphene/silicon Schottky diodes. *Nanoscale research letters* **2012,** *7* (1), 1-6.

37. Tongay, S.; Lemaitre, M.; Miao, X.; Gila, B.; Appleton, B.; Hebard, A., Rectification at graphene-semiconductor interfaces: zero-gap semiconductor-based diodes. *Physical Review X* **2012,** *2* (1), 011002.

38. Tomer, D.; Rajput, S.; Hudy, L.; Li, C.; Li, L., Carrier transport in reverse-biased graphene/semiconductor Schottky junctions. *Applied physics letters* **2015,** *106* (17), 173510.

39. Ulman, A., Formation and structure of self-assembled monolayers. *Chemical reviews* **1996,** *96* (4), 1533-1554.

40. Love, J. C.; Estroff, L. A.; Kriebel, J. K.; Nuzzo, R. G.; Whitesides, G. M., Self-assembled monolayers of thiolates on metals as a form of nanotechnology. *Chemical reviews* **2005,** *105* (4), 1103-1170.

41. Lafkioti, M.; Krauss, B.; Lohmann, T.; Zschieschang, U.; Klauk, H.; Klitzing, K. v.; Smet, J. H., Graphene on a hydrophobic substrate: doping reduction and hysteresis suppression under ambient conditions. *Nano letters* **2010,** *10* (4), 1149-1153.

42. Wang, X.; Xu, J. B.; Wang, C.; Du, J.; Xie, W., High-Performance Graphene Devices on SiO2/Si Substrate Modified by Highly Ordered Self-Assembled Monolayers. *Advanced Materials* **2011,** *23* (21), 2464-2468.

43. Wang, S.; Suzuki, S.; Furukawa, K.; Orofeo, C. M.; Takamura, M.; Hibino, H., Selective charge doping of chemical vapor deposition-grown graphene by interface modification. *Applied physics letters* **2013,** *103* (25), 253116.

44. Lv, H.; Wu, H.; Xiao, K.; Zhu, W.; Xu, H.; Zhang, Z.; Qian, H., Graphene mobility enhancement by organosilane interface engineering. *Applied physics letters* **2013,** *102* (18), 183107.

45. Cernetic, N.; Hutchins, D. O.; Ma, H.; Jen, A. K.-Y., Influence of self-assembled monolayer binding group on graphene transistors. *Applied physics letters* **2015,** *106* (2), 021603.

46. Lee, B.; Chen, Y.; Duerr, F.; Mastrogiovanni, D.; Garfunkel, E.; Andrei, E.; Podzorov, V., Modification of electronic properties of graphene with self-assembled monolayers. *Nano letters* **2010,** *10* (7), 2427-2432.

47. Yokota, K.; Takai, K.; Enoki, T., Carrier control of graphene driven by the proximity effect of functionalized self-assembled monolayers. *Nano letters* **2011,** *11* (9), 3669-3675.

48. Lee, W. H.; Park, J.; Kim, Y.; Kim, K. S.; Hong, B. H.; Cho, K., Control of Graphene Field-Effect Transistors by Interfacial Hydrophobic Self-Assembled Monolayers. *Advanced Materials* **2011,** *23* (30), 3460-3464.

49. Yan, Z.; Sun, Z.; Lu, W.; Yao, J.; Zhu, Y.; Tour, J. M., Controlled modulation of electronic properties of graphene by self-assembled monolayers on SiO2 substrates. *ACS nano* **2011,** *5* (2), 1535-1540.

50. Lenfant, S.; Krzeminski, C.; Delerue, C.; Allan, G.; Vuillaume, D., Molecular rectifying diodes from self-assembly on silicon. *Nano letters* **2003,** *3* (6), 741-746.

51. Novoselov, K. S.; Geim, A. K.; Morozov, S.; Jiang, D.; Katsnelson, M.; Grigorieva, I.; Dubonos, S.; Firsov; AA, Two-dimensional gas of massless Dirac fermions in graphene. *nature* **2005,** *438* (7065), 197.

52. Geim, A. K.; Novoselov, K. S., The rise of graphene. *Nature materials* **2007,** *6* (3), 183.

53. Bolotin, K. I.; Sikes, K.; Jiang, Z.; Klima, M.; Fudenberg, G.; Hone, J.; Kim, P.; Stormer, H., Ultrahigh electron mobility in suspended graphene. *Solid State Communications* **2008,** *146* (9-10), 351-355.

54. Pogna, E. A.; Trovatello, C.; Tielrooij, K.; Hesp, N.; Principi, A.; Lundeberg, M.; Banszerus, L.; Massicotte, M.; Schmidt, P.; Davydovskaya, D. In *Non-equilibrium optical properties of encapsulated graphene*, Lasers and Electro-Optics Europe & European Quantum Electronics Conference (CLEO/Europe-EQEC, 2017 Conference on), IEEE: 2017; pp 1-1.

55. Mak, K. F.; Ju, L.; Wang, F.; Heinz, T. F., Optical spectroscopy of graphene: , from the far infrared to the ultraviolet. *Solid State Communications* **2012,** *152* (15), 1341-1349.

56. http://www.mistralab.it/approfondimenti/Telecomunicazioni_progretto2/grafene Structure %20of%20 graphene.html, Accesed May, 2018

57. Wang, J.-T.; Chen, C.; Kawazoe, Y., New carbon allotropes with helical chains of complementary chirality connected by ethene-type π-conjugation. *Scientific reports* **2013,** *3*, 3077.

58. Neto, A. C.; Guinea, F.; Peres, N.; Novoselov, K. S.; Geim, A. K., The electronic properties of graphene. *Reviews of modern physics* **2009,** *81* (1), 109.

59. Biró, L. P.; Nemes-Incze, P.; Lambin, P., Graphene: nanoscale processing and recent applications. *Nanoscale* **2012,** *4* (6), 1824-1839.

60. Neto, A. C.; Guinea, F.; Peres, N. M.; Novoselov, K. S.; Geim, A. K., The electronic properties of graphene. *Reviews of modern physics* **2009,** *81* (1), 109.

61. Reich, S.; Maultzsch, J.; Thomsen, C.; Ordejon, P., Tight-binding description of graphene. *Physical Review B* **2002,** *66* (3), 035412.

62. Sarma, S. D.; Adam, S.; Hwang, E.; Rossi, E., Electronic transport in two-dimensional graphene. *Reviews of modern physics* **2011,** *83* (2), 407.

63. Bostwick, A.; Ohta, T.; Seyller, T.; Horn, K.; Rotenberg, E., Quasiparticle dynamics in graphene. *Nature physics* **2007,** *3* (1), 36.

64. Katsnelson, M.; Novoselov, K.; Geim, A., Chiral tunnelling and the Klein paradox in graphene. *Nature physics* **2006,** *2* (9), 620.

65. Malard, L.; Pimenta, M.; Dresselhaus, G.; Dresselhaus, M., Raman spectroscopy in graphene. *Physics Reports* **2009,** *473* (5-6), 51-87.

66. Cooper, D. R.; D'Anjou, B.; Ghattamaneni, N.; Harack, B.; Hilke, M.; Horth, A.; Majlis, N.; Massicotte, M.; Vandsburger, L.; Whiteway, E., Experimental review of graphene. *International Scholarly Research Notices* **2012,** *2012*.

67. Peres, N., Colloquium: The transport properties of graphene: An introduction. *Reviews of modern physics* **2010,** *82* (3), 2673.

68. Bonaccorso, F.; Sun, Z.; Hasan, T.; Ferrari, A., Graphene photonics and optoelectronics. *Nature Photonics* **2010,** *4* (9), 611-622.

69. Jo, G.; Choe, M.; Lee, S.; Park, W.; Kahng, Y. H.; Lee, T., The application of graphene as electrodes in electrical and optical devices. *Nanotechnology* **2012,** *23* (11), 112001.

70. Meyer, J. C.; Geim, A. K.; Katsnelson, M. I.; Novoselov, K. S.; Booth, T. J.; Roth, S., The structure of suspended graphene sheets. *nature* **2007,** *446* (7131), 60.

71. Sharma, R.; Baik, J. H.; Perera, C. J.; Strano, M. S., Anomalously large reactivity of single graphene layers and edges toward electron transfer chemistries. *Nano letters* **2010,** *10* (2), 398-405.

72. Schedin, F.; Geim, A.; Morozov, S.; Hill, E.; Blake, P.; Katsnelson, M.; Novoselov, K., Detection of individual gas molecules adsorbed on graphene. *Nature materials* **2007,** *6* (9), 652.

73. Wehling, T.; Novoselov, K.; Morozov, S.; Vdovin, E.; Katsnelson, M.; Geim, A.; Lichtenstein, A., Molecular doping of graphene. *Nano letters* **2008,** *8* (1), 173-177.

74. Gierz, I.; Riedl, C.; Starke, U.; Ast, C. R.; Kern, K., Atomic hole doping of graphene. *Nano letters* **2008,** *8* (12), 4603-4607.

75. Gunes, F.; Shin, H.-J.; Biswas, C.; Han, G. H.; Kim, E. S.; Chae, S. J.; Choi, J.-Y.; Lee, Y. H., Layer-by-layer doping of few-layer graphene film. *ACS nano* **2010,** *4* (8), 4595-4600.

76. Martins, T.; Miwa, R. d.; Da Silva, A. J.; Fazzio, A., Electronic and transport properties of boron-doped graphene nanoribbons. *Physical review letters* **2007,** *98* (19), 196803.

77. Panchakarla, L.; Subrahmanyam, K.; Saha, S.; Govindaraj, A.; Krishnamurthy, H.; Waghmare, U.; Rao, C., Synthesis, Structure, and Properties of Boron-and Nitrogen-Doped Graphene. *Advanced Materials* **2009,** *21* (46), 4726-4730.

78. Zhao, L.; He, R.; Rim, K. T.; Schiros, T.; Kim, K. S.; Zhou, H.; Gutiérrez, C.; Chockalingam, S.; Arguello, C. J.; Pálová, L., Visualizing individual nitrogen dopants in monolayer graphene. *Science* **2011,** *333* (6045), 999-1003.

79. Giovannetti, G.; Khomyakov, P.; Brocks, G.; Karpan, V. v.; Van den Brink, J.; Kelly, P. J., Doping graphene with metal contacts. *Physical review letters* **2008,** *101* (2), 026803.

80. Xia, F.; Perebeinos, V.; Lin, Y.-m.; Wu, Y.; Avouris, P., The origins and limits of metal–graphene junction resistance. *Nature nanotechnology* **2011,** *6* (3), 179.

81. Zhou, S. Y.; Gweon, G.-H.; Fedorov, A.; First, P.; De Heer, W.; Lee, D.-H.; Guinea, F.; Neto, A. C.; Lanzara, A., Substrate-induced bandgap opening in epitaxial graphene. *Nature materials* **2007,** *6* (10), 770.

82. Calizo, I.; Bao, W.; Miao, F.; Lau, C. N.; Balandin, A. A., The effect of substrates on the Raman spectrum of graphene: Graphene-on-sapphire and graphene-on-glass. *Applied Physics Letters* **2007,** *91* (20), 201904.

83. Zhang, Y.; Small, J. P.; Pontius, W. V.; Kim, P., Fabrication and electric-field-dependent transport measurements of mesoscopic graphite devices. *Applied Physics Letters* **2005,** *86* (7), 073104.

84. Novoselov, K. S.; Geim, A. K.; Morozov, S.; Jiang, D.; Zhang, Y.; Dubonos, S.; Grigorieva, I.; Firsov, A., Electric field effect in atomically thin carbon films. *science* **2004,** *306* (5696), 666-669.

85. Liu, W.; Kraemer, S.; Sarkar, D.; Li, H.; Ajayan, P. M.; Banerjee, K., Controllable and rapid synthesis of high-quality and large-area Bernal stacked bilayer graphene using chemical vapor deposition. *Chemistry of Materials* **2013,** *26* (2), 907-915.

86. Novoselov, K.; Neto, A. C., Two-dimensional crystals-based heterostructures: materials with tailored properties. *Physica Scripta* **2012,** *2012* (T146), 014006.

87. Forbeaux, I.; Themlin, J.-M.; Debever, J.-M., High-temperature graphitization of the 6H-SiC (0001) face. *Surface science* **1999,** *442* (1), 9-18.

88. Lenz-Solomun, P.; Wu, M.-C.; Goodman, D. W., Methane coupling at low temperatures on Ru (0001) and Ru (11¯20) catalysts. *Catalysis letters* **1994,** *25* (1-2), 75-86.

89. Muñoz, R.; Gómez-Aleixandre, C., Review of CVD synthesis of graphene. *Chemical Vapor Deposition* **2013,** *19* (10-11-12), 297-322.

90. Luo, Y.-R., *Comprehensive handbook of chemical bond energies*. CRC press: 2007.

91. Au, C.-T.; Ng, C.-F.; Liao, M.-S., Methane Dissociation and Syngas Formation on Ru, Os, Rh, Ir, Pd, Pt, Cu, Ag, and Au: A Theoretical Study. *Journal of Catalysis* **1999,** *185* (1), 12-22.

92. Miao, C.; Zheng, C.; Liang, O.; Xie, Y.-H., Chemical vapor deposition of graphene. In *Physics and applications of graphene-experiments*, InTech: 2011.

93. Li, X.; Cai, W.; An, J.; Kim, S.; Nah, J.; Yang, D.; Piner, R.; Velamakanni, A.; Jung, I.; Tutuc, E., Large-area synthesis of high-quality and uniform graphene films on copper foils. *science* **2009,** *324* (5932), 1312-1314.

94. Kim, K. S.; Zhao, Y.; Jang, H.; Lee, S. Y.; Kim, J. M.; Kim, K. S.; Ahn, J.-H.; Kim, P.; Choi, J.-Y.; Hong, B. H., Large-scale pattern growth of graphene films for stretchable transparent electrodes. *Nature* **2009,** *457* (7230), 706-710.

95. Murata, Y.; Nie, S.; Ebnonnasir, A.; Starodub, E.; Kappes, B.; McCarty, K.; Ciobanu, C.; Kodambaka, S., Growth structure and work function of bilayer graphene on Pd (111). *Physical Review B* **2012,** *85* (20), 205443.

96. Loginova, E.; Bartelt, N.; Feibelman, P.; McCarty, K., Factors influencing graphene growth on metal surfaces. *New Journal of Physics* **2009,** *11* (6), 063046.

97. Bae, S.; Kim, H.; Lee, Y.; Xu, X.; Park, J.-S.; Zheng, Y.; Balakrishnan, J.; Lei, T.; Kim, H. R.; Song, Y. I., Roll-to-roll production of 30-inch graphene films for transparent electrodes. *Nature nanotechnology* **2010,** *5* (8), 574-578.

98. Braun, F., Ueber die Stromleitung durch Schwefelmetalle. *Annalen der Physik* **1875,** *229* (12), 556-563.

99. Bethe, H. A., Theory of the boundary layer of crystal rectifiers. In *Semiconductor Devices: Pioneering Papers*, World Scientific: 1991; pp 387-399.

100. Sze, S. M.; Ng, K. K., *Metal-semiconductor contacts*. Wiley Online Library: 2006.

101. Mönch, W., Metal-semiconductor contacts: electronic properties. *Surface science* **1994,** *299*, 928-944.

102. Bardeen, J., Surface states and rectification at a metal semi-conductor contact. *Physical Review* **1947,** *71* (10), 717.

103. Contacts, M.-S., EH Rhoderick and RH Williams. *Clarendon, Oxford* **1988**, 1-70.

104. Simmons, J., Conduction in thin dielectric films. *Journal of Physics D: Applied Physics* **1971,** *4* (5), 613.

105. Kınacı, B.; Özen, Y.; Kızılkaya, K.; Asar, T.; Çetin, S.; Boyalı, E.; Öztürk, M.; Memmedli, T.; Özçelik, S., Effect of alloy composition on structural, optical and morphological properties and electrical characteristics of Ga x In 1− x P/GaAs structure. *Journal of Materials Science: Materials in Electronics* **2013,** *24* (4), 1375-1381.

106. Binnig, G.; Quate, C. F.; Gerber, C., Atomic force microscope. *Physical review letters* **1986,** *56* (9), 930-933.

107. Batsanov, S., Van der Waals radii of elements. *Inorganic materials* **2001,** *37* (9), 871-885.

108. Mironov, V. L., Fundamentals of scanning probe microscopy. *The Russian Academy of Sciences* **2004**.

109. Rosenwaks, Y.; Shikler, R.; Glatzel, T.; Sadewasser, S., Kelvin probe force microscopy of semiconductor surface defects. *Physical Review B* **2004,** *70* (8), 085320.

110. Maldonado, S.; Smith, T. J.; Williams, R. D.; Morin, S.; Barton, E.; Stevenson, K. J., Surface modification of indium tin oxide via electrochemical reduction of aryldiazonium cations. *Langmuir* **2006,** *22* (6), 2884-2891.

111. Beerbom, M.; Lägel, B.; Cascio, A.; Doran, B.; Schlaf, R., Direct comparison of photoemission spectroscopy and in situ Kelvin probe work function measurements on indium tin oxide films. *Journal of electron spectroscopy and related phenomena* **2006,** *152* (1-2), 12-17.

112. Jorio, A., Raman spectroscopy in graphene-based systems: Prototypes for nanoscience and nanometrology. *ISRN Nanotechnology* **2012,** *2012.*

113. Ni, Z.; Wang, Y.; Yu, T.; Shen, Z., Raman spectroscopy and imaging of graphene. *Nano Research* **2008,** *1* (4), 273-291.

114. Wang, Y. y.; Ni, Z. h.; Yu, T.; Shen, Z. X.; Wang, H. m.; Wu, Y. h.; Chen, W.; Shen Wee, A. T., Raman studies of monolayer graphene: the substrate effect. *The Journal of Physical Chemistry C* **2008,** *112* (29), 10637-10640.

115. Beams, R.; Cançado, L. G.; Novotny, L., Raman characterization of defects and dopants in graphene. *Journal of Physics: Condensed Matter* **2015,** *27* (8), 083002.

116. Reina, A.; Jia, X.; Ho, J.; Nezich, D.; Son, H.; Bulovic, V.; Dresselhaus, M. S.; Kong, J., Large area, few-layer graphene films on arbitrary substrates by chemical vapor deposition. *Nano letters* **2008,** *9* (1), 30-35.

117. Yan, K.; Peng, H.; Zhou, Y.; Li, H.; Liu, Z., Formation of bilayer bernal graphene: layer-by-layer epitaxy via chemical vapor deposition. *Nano letters* **2011,** *11* (3), 1106-1110.

118. Chen, S.; Cai, W.; Piner, R. D.; Suk, J. W.; Wu, Y.; Ren, Y.; Kang, J.; Ruoff, R. S., Synthesis and characterization of large-area graphene and graphite films on commercial Cu–Ni alloy foils. *Nano letters* **2011,** *11* (9), 3519-3525.

119. Yan, Z.; Peng, Z.; Sun, Z.; Yao, J.; Zhu, Y.; Liu, Z.; Ajayan, P. M.; Tour, J. M., Growth of bilayer graphene on insulating substrates. *ACS nano* **2011,** *5* (10), 8187-8192.

120. Kumar, R.; Varandani, D.; Mehta, B., Nanoscale interface formation and charge transfer in graphene/silicon Schottky junctions; KPFM and CAFM studies. *Carbon* **2016,** *98*, 41-49.

121. Ferrari, A. C.; Meyer, J.; Scardaci, V.; Casiraghi, C.; Lazzeri, M.; Mauri, F.; Piscanec, S.; Jiang, D.; Novoselov, K.; Roth, S., Raman spectrum of graphene and graphene layers. *Physical review letters* **2006,** *97* (18), 187401.

122. Kim, H.-Y.; Lee, K.; McEvoy, N.; Yim, C.; Duesberg, G. S., Chemically modulated graphene diodes. *Nano letters* **2013,** *13* (5), 2182-2188.

123. Lin, Z.; Ye, X.; Han, J.; Chen, Q.; Fan, P.; Zhang, H.; Xie, D.; Zhu, H.; Zhong, M., Precise control of the number of layers of graphene by picosecond laser thinning. *Scientific reports* **2015,** *5*, 11662.

124. Bkakri, R.; Kusmartseva, O. E.; Kusmartsev, F.; Song, M.; Bouazizi, A., Degree of phase separation effects on the charge transfer properties of P3HT: Graphene nanocomposites. *Journal of Luminescence* **2015,** *161*, 264-270.

125. Liu, J.; Yin, Y.; Yu, L.; Shi, Y.; Liang, D.; Dai, D., Silicon-graphene conductive photodetector with ultra-high responsivity. *Scientific reports* **2017,** *7*, 40904.

126. Kapoor, A. K.; Kumar, U.; Balakrishnan, V.; Basu, P., Degradation process in organic thin film devices fabricated using P3HT. *Pramana* **2007,** *68* (3), 489-498.

127. Zhao, Y.; Sugunan, A.; Schmidt, T.; Fornara, A.; Toprak, M. S.; Muhammed, M., Relaxation is the key to longer life: suppressed degradation of P3HT films on conductive substrates. *Journal of Materials Chemistry A* **2014,** *2* (33), 13270-13276.

128. Li, J.; Niu, L.; Zheng, Z.; Yan, F., Photosensitive graphene transistors. *Advanced Materials* **2014,** *26* (31), 5239-5273.

129. Suk, J. W.; Lee, W. H.; Lee, J.; Chou, H.; Piner, R. D.; Hao, Y.; Akinwande, D.; Ruoff, R. S., Enhancement of the electrical properties of graphene grown by chemical vapor deposition via controlling the effects of polymer residue. *Nano letters* **2013,** *13* (4), 1462-1467.

130. Pirkle, A.; Chan, J.; Venugopal, A.; Hinojos, D.; Magnuson, C.; McDonnell, S.; Colombo, L.; Vogel, E.; Ruoff, R.; Wallace, R., The effect of chemical residues on the physical and electrical properties of chemical vapor deposited graphene transferred to SiO2. *Applied Physics Letters* **2011,** *99* (12), 122108.

131. Sze, S., Physics of Semiconductor Devices; John Willy & Sons, Inc. *New York* **1981**.

132. Zhang, W.; Hu, R.; Li, D.; Huo, M.-M.; Ai, X.-C.; Zhang, J.-P., Primary dynamics of exciton and charge photogeneration in solvent vapor annealed P3HT/PCBM films. *The Journal of Physical Chemistry C* **2012,** *116* (6), 4298-4310.

133. Tamai, Y.; Ohkita, H.; Benten, H.; Ito, S., Exciton diffusion in conjugated polymers: from fundamental understanding to improvement in photovoltaic conversion efficiency. *J. Phys. Chem. Lett* **2015,** *6* (17), 3417-3428.

134. Ni, Z.; Ma, L.; Du, S.; Xu, Y.; Yuan, M.; Fang, H.; Wang, Z.; Xu, M.; Li, D.; Yang, J., Plasmonic Silicon Quantum Dots Enabled High-Sensitivity Ultrabroadband Photodetection of Graphene-Based Hybrid Phototransistors. *ACS nano* **2017,** *11* (10), 9854-9862.

135. Guo, N.; Hu, W.; Jiang, T.; Gong, F.; Luo, W.; Qiu, W.; Wang, P.; Liu, L.; Wu, S.; Liao, L., High-quality infrared imaging with graphene photodetectors at room temperature. *Nanoscale* **2016,** *8* (35), 16065-16072.

136. Miao, J.; Hu, W.; Guo, N.; Lu, Z.; Liu, X.; Liao, L.; Chen, P.; Jiang, T.; Wu, S.; Ho, J. C., High-Responsivity Graphene/InAs Nanowire Heterojunction Near-Infrared Photodetectors with Distinct Photocurrent On/Off Ratios. *Small* **2015,** *11* (8), 936-942.

VITA

Date and Place of Birth: 25.11.1985, İzmir-TURKEY

EDUCATION

2011–2018 Doctor of Philosophy in Materials Science and Engineering

Graduate School of Engineering and Sciences, İzmir Institute of Technology,

İzmir-TURKEY

Thesis Title: Developing Graphene-Organic Hybrid Electrodes for Silicon Based Schottky Devices

Supervisor: Assoc. Prof. Dr. Cem ÇELEBİ

2008–2011 Master of Science in Physics

Graduate School of Engineering and Sciences, İzmir Institute of Technology,

İzmir-TURKEY

Thesis Title: Interface properties of Modified Indium Tin Oxide Based Organic Light Emitting Diodes with Functional Aromatic Molecules

Supervisor: Assoc. Prof. Dr. Salih OKUR

2002–2006 Bachelor of Physics

Department of Physics, Faculty of Science, Uludağ University, İzmir-TURKEY

SELECTED PUBLICATIONS

1. **H. Aydın**, S.B. Kalkan, C. Varlikli and C. Celebi, "Graphene-P3HT Bilayer Electrode for Silicon-Based Schottky Junction Photodetector" **Nanotechnology IOP**, 29, 145502 (2018).

2. **H. Aydın**, C. Bacaksiz, N. Yagmurcukardes, C. Karakaya, O. Mermer, M. Can, R. T. Senger, H. Sahin, Y. Selamet, "Experimental and Computational Investigation of Graphene/SAMs/n-Si Schottky Diodes," **Applied Surface Science**, 428 1010-1017. (2018).

3. S. B. Kalkan, **H. Aydın**, D. Ozkendir and C. Celebi, "The Effect of Adsorbates on the Electrical Stability of Graphene Studied by Transient Photocurrent Spectroscopy," **Applied Physics Letters**, 112, 013103 (2018).